



**Politecnico
di Torino**

Politecnico di Torino

Corso di Laurea Magistrale in Communications Engineering

A.a. 2023/2024

Sessione di Laurea Marzo 2026

Antenna Pattern Reconstruction from Underdetermined Near-Field Measurements

Tesi svolta presso CEA-Leti, Grenoble, Francia

Candidato: Jonas Thalmeier

Relatore PoliTo: Paola Pirinoli

Relatori CEA: Francesco Foglia Manzillo
Olivier Rance

Plagiarism Declaration

Dichiaro che la presente tesi è frutto del mio lavoro originale e che non ho ricevuto alcuna assistenza esterna. Sono state utilizzate esclusivamente le fonti citate nel presente elaborato. Le parti costituite da citazioni dirette o parafrasi sono opportunamente indicate come tali.

I warrant, that the thesis is my original work and that I have not received outside assistance. Only the sources cited have been used in this report. Parts that are direct quotes or paraphrases are identified as such.

Done at Grenoble, on February 25, 2026

Signature:



Thaliev

Abstract

English

This thesis investigates methods for reconstructing antenna far field radiation patterns from underdetermined planar near-field measurements. Traditional near-field characterization relies on the Nyquist sampling criterion, which often leads to prohibitive acquisition times. The primary objective of this study was to evaluate sampling strategies that reduce the number of required measurement points without significantly degrading the accuracy of the reconstructed far field. Five representative sampling and interpolation schemes were implemented and compared, along with an approach designed to mitigate truncation errors. These methods were rigorously assessed through full-wave simulations and validated using measurements. The results demonstrate that “informed” strategies, specifically those incorporating prior knowledge of the source geometry, achieve superior efficiency. Non-redundant sampling and greedy selection allowed for a reduction in the number of samples by a factor of up to 20 compared to uniform $\lambda/2$ sampling while maintaining a low normalized mean square error within the reliable angular region. Furthermore, the selection-based approach exhibited the highest robustness against measurement noise, proving capable of accurate reconstruction even at low signal-to-noise ratios.

Italiano

Questa tesi analizza metodi per la ricostruzione dei diagrammi di radiazione in campo lontano di antenne a partire da misure planari di campo vicino sottodeterminate. La caratterizzazione tradizionale in campo vicino si basa sul criterio di campionamento di Nyquist, che spesso comporta tempi di acquisizione proibitivi. L’obiettivo principale di questo studio è stato valutare strategie di campionamento in grado di ridurre il numero di punti di misura necessari senza degradare in modo significativo l’accuratezza del campo lontano ricostruito. Sono stati implementati e confrontati cinque schemi rappresentativi di campionamento e interpolazione, insieme a un approccio progettato per mitigare gli errori di troncamento. Tali metodi sono stati valutati rigorosamente mediante simulazioni elettromagnetiche full-wave e validati tramite misure sperimentali. I risultati dimostrano che le strategie “informate”, in particolare quelle che incorporano conoscenze a priori sulla geometria della sorgente, raggiungono un’efficienza superiore. Il campionamento non ridondante e la selezione greedy hanno consentito di ridurre il numero di campioni fino a un fattore 20 rispetto al campionamento uniforme a $\lambda/2$, mantenendo un basso errore quadratico medio normalizzato nella regione angolare affidabile. Inoltre, l’approccio basato sulla selezione ha mostrato la maggiore robustezza al rumore di misura, dimostrando di poter garantire una ricostruzione accurata anche a bassi rapporti segnale-rumore.

Contents

1	Motivation	9
1.1	Near-Field Measurement Procedure	10
1.2	Outline	12
2	Theoretical Foundations of Antenna Field Analysis	14
2.1	Field Regions	14
2.2	Maxwell Equations	16
2.3	Auxiliary Potential Functions	16
2.4	Plane Wave Expansion	18
2.5	Representation of the Far Field	20
2.6	Numerical Implementation for Planar Aperture Problems	20
2.7	Discretization of Source Quantities	21
2.8	Calculation of the Near Field	22
2.9	Near- to Far Field Transformation	24
2.9.1	Calculation of the NFFFT	24
2.9.2	Influence of the Sampling Step Size	25
2.9.3	Truncation Error and Reliable Region	26
2.10	Generation of Simulation Data	29
2.11	Conclusion	31
3	Sampling Schemes and Reconstruction Algorithms	32
3.1	Non-Redundant Near-Field Sampling	34
3.1.1	Degrees of Freedom of a Scattered Field	34
3.1.2	Optimal Parametrization of a Measurement Curve	36
3.1.3	Application of Parametrization to Plane-Polar Geometry	38
3.1.4	Interpolation	40
3.1.5	Implementation in the Plane-Polar Case	41
3.1.6	Results	42
3.2	Near Field Warping Sampling Scheme	47
3.2.1	Approximation of Eigenvalue Problem	48
3.2.2	Parametrization	49
3.2.3	Interpolation	51

3.2.4	Spatial Varying Oversampling	51
3.2.5	Results	52
3.2.6	Alternative Oversampling of the Warped Grid	52
3.3	Sparse Nonuniform Planar Sampling Based on Angular Projection	53
3.3.1	Methodology	54
3.3.2	Results	55
3.4	Interpolation of Near Fields without Prior Source Knowledge	56
3.4.1	Methodology	57
3.4.2	Pseudo Random Sampling Point Selection	58
3.4.3	Results	59
3.5	Greedy Sampling Point Selection for Planar Near-Field Measurements	60
3.5.1	Radiation Operator Derivation	60
3.5.2	Optimal Sampling Point Selection	61
3.5.3	Alternative Selection of Optimal Sampling Points	62
3.5.4	Source Domain Field Reconstruction	65
3.5.5	Results	65
3.6	Gerchberg-Papoulis Algorithm	66
3.6.1	Methodology	66
3.6.2	Gradient Descent for Convergence Control	68
3.6.3	Selection of the Reliability Scaling Factor C	68
3.6.4	Results	69
3.7	Conclusion	70
4	Minimizing Samples in a Limited Acquisition Area	73
4.1	Adapting the Non-Redundant Sampling Grid	73
4.1.1	Replacing Sampling Radii	74
4.1.2	Squeezing Sampling radii	75
4.1.3	Qualitative Comparison	76
4.2	Quantitative Comparison on a 10-dBi Standard-Gain Horn	78
4.2.1	Metrics	78
4.2.2	Results using Noiseless Data	80
4.2.3	Consideration on the Impact of Noise	83
4.2.4	Concluding Remarks on the Comparative Analysis	86
4.3	Quantitative Comparison Based on Measurement Data	89
4.3.1	Dataset and Evaluation Procedure	89
4.3.2	Results	91
4.3.3	Concluding Remarks on the Comparative Analysis	93
5	Conclusion	95

List of Figures

1.1	Near-field measurement system. Figure reproduced from [1].	11
2.1	Schematic representation of the reactive near field, radiating near field (Fresnel), and far field (Fraunhofer) regions of an antenna, including their commonly used boundary approximations. Figure reproduced from [1].	15
2.2	Geometry of the canonical aperture on an infinite groundplane.	21
2.3	Near field of a canonical aperture ($X_S = 2.5\lambda$, $Y_S = 1.5\lambda$, TE ₁₀ mode) evaluated at a distance of 2λ , calculated using the method described in (2.8.1) (Numerical method) and using the plane wave expansion.	25
2.4	Far field of a canonical aperture (size $5\lambda \times 3\lambda$, TE ₁₀ mode) calculated from the near-field distribution over an area of $750\lambda \times 450\lambda$ at a distance of $z = 17.5\lambda$ using the Fourier transform method for different spatial sampling intervals.	26
2.5	Far field of a 10 dBi standard-gain horn calculated from the near-field distribution over an area of $166\lambda \times 166\lambda$ at a distance of $z = 2.89\lambda$ using the Fourier transform method for different spatial sampling intervals.	27
2.6	Schematic definition of the angle of validity θ' . The resulting reliable region is indicated by the gray shading.	28
2.7	Comparison between the analytically computed far field of a canonical rectangular aperture ($5\lambda \times 3\lambda$, TE ₁₀ mode) and the far-field reconstructed from a finite planar measurement surface of $17\lambda \times 16\lambda$ at a distance of 17.5λ . The resulting angle of validity in the x -plane is $\theta'_x = 39.7^\circ$	29
2.8	Comparison between the simulated far field of a 10 dBi standard-gain horn and the far field reconstructed from a finite planar measurement surface of $17\lambda \times 11\lambda$ at a distance of 10.75λ . The resulting angle of validity in the x -plane is $\theta'_x = 55.0^\circ$	30
2.9	Workflow of generating and importing simulation data into Python.	30
3.1	Geometry of scatterers within the sphere B of radius a and measurement curve s . Figure reproduced from [14].	35
3.2	Geometry of scatterer and measurement curve in three dimensions. Figure reproduced from [15].	36

3.3	Geometry of the antenna under test and the plane-polar surface. Figure reproduced from [27].	38
3.4	Meridian plane geometry. Figure reproduced from [27].	39
3.5	10 dBi horn under test, near-field measurement surface and non-redundant sampling point.	43
3.6	22 non-redundant sampling points on 3 radii ($r/\lambda = [0, 1.17, 3.12]$). . . .	43
3.7	Co-polarized far-field pattern (cut in the plane $\phi = 0^\circ$) at 30 GHz of a 10-dBi standard-gain horn reconstructed from 22 non-redundant near-field samples at a distance of $z = 2.89\lambda$, compared to the simulated far-field data.	44
3.8	Flat lens antenna on the plane $z = 0$ illuminated by a horn feed (drawn to scale).	45
3.9	Co-polarized and cross-polarized far-field patterns (in the plane $\phi = 0^\circ$). The results of reconstruction from grids considering lens-only vs. lens-plus-horn near-field grids ($z = 0.62\sqrt{D^3/\lambda} = 19.3\lambda = 41.4$ mm, $r_{\max} = 31$ mm), are compared to full-wave simulations.	46
3.10	Measurement configuration for the coordinate warping scheme.	48
3.11	Warped sampling grid consisting of 25 points.	52
3.12	Co-polarized far field pattern (cut in the plane $\phi = 0^\circ$) at 30 GHz of a 10-dBi standard-gain horn reconstructed from a warped sampling grid consisting of 25 points at a distance of $z = 2.89\lambda$, compared to the simulated far field.	53
3.13	Projection of spherical coordinates onto the measurement plane.	55
3.14	Igloo sampling grid consisting of 76 points.	56
3.15	Co-polarized far-field pattern (cut in the plane $\phi = 0^\circ$) at 30 GHz of a 10-dBi standard-gain horn reconstructed from an Igloo sampling grid consisting of 76 points at a distance of $z_0 = 2.898\lambda$, compared with the simulated far field.	56
3.16	127 random selected points from a $\lambda/2$ grid.	59
3.17	Co-polarized far-field pattern (cut in the plane $\phi = 0^\circ$) at 30 GHz of a 10-dBi standard-gain horn reconstructed from a random grid consisting of 127 points at a distance of $z_0 = 2.898\lambda$, compared with the simulated far field.	60
3.18	Sampling locations selected by the greedy noise factor minimization method ($X_S = 1.36\lambda$, $Y_S = 1\lambda$, $X_O = Y_O = 11.5\lambda$, $z_0 = 7\lambda$).	63
3.19	Sampling locations selected by confidence ellipsoid minimization ($X_S = 1.36\lambda$, $Y_S = 1\lambda$, $X_O = Y_O = 11.5\lambda$, $z_0 = 7\lambda$).	64
3.20	Sampling locations selected by MSE minimization ($X_S = 1.36\lambda$, $Y_S = 1\lambda$, $X_O = Y_O = 11.5\lambda$, $z_0 = 7\lambda$).	64
3.21	Five sampling points selected by MSE minimization from a $\lambda/2$ grid. . .	65

3.22	Co-polarized far-field pattern (cut in the plane $\phi = 0^\circ$) at 30 GHz of a 10-dBi standard-gain horn reconstructed from five optimally selected sampling points at a distance of $z_0 = 2.898\lambda$, compared with the simulated far field.	66
3.23	Geometric configuration of the Gerchberg-Papoulis based algorithm for reducing truncation error.	67
3.24	Co-polarized far-field pattern (cut in the plane $\phi = 20^\circ$) at 30 GHz of a 10-dBi standard-gain horn reconstructed from uniform $\lambda/2$ sampling with and without the application of the GPA in comparison to the simulated far field.	69
3.25	Co-polarized far-field pattern (cut in the plane $\phi = 70^\circ$) at 30 GHz of a 10-dBi standard-gain horn reconstructed from uniform $\lambda/2$ sampling with and without the application of the GPA in comparison to the simulated far field.	70
4.1	Visualization of the replacement and squeezing methods used to adapt the original sampling grid to a restricted $18\lambda \times 18\lambda$ region, marked by the dashed line.	77
4.2	NMSE as a function of the undersampling ratio. The results are obtained from simulated near-field data of a 10-dBi standard-gain horn over a confined acquisition area of $4\lambda \times 3.5\lambda$, in the absence of measurement noise.	80
4.3	Undersampling ratio required to achieve NMSE within 1 dB, 3 dB, and 5 dB of the baseline NMSE. Noiseless simulation near-field data have been considered.	81
4.4	Co-polarized far-field pattern (cut in the plane $\phi = 0^\circ$) at 30 GHz of a 10-dBi standard-gain horn reconstructed from ~ 110 near-field samples (corresponding to an undersampling ratio of ~ 0.1) at a distance of $z = 2.89\lambda$ using three different sampling schemes, compared to the simulated far-field data.	83
4.5	Average computation time for sampling grid generation and interpolation for the different reconstruction methods.	84
4.6	NMSE as a function of the undersampling ratio. The results are obtained from simulated near-field data of a 10-dBi standard-gain horn over a confined acquisition area of $4\lambda \times 3.5\lambda$, with additive white Gaussian noise at an SNR of 20 dB applied to the data.	85
4.7	Undersampling ratio required to achieve an NMSE within 1 dB, 3 dB, and 5 dB of the baseline NMSE for an SNR of 20 dB.	86
4.8	NMSE as a function of the undersampling ratio. Results are based on simulated data from a 10-dBi standard-gain horn with a confined acquisition area and 10 dB additive white Gaussian noise.	87

4.9	Undersampling ratio required to achieve an NMSE within 1 dB, 3 dB, and 5 dB of the baseline NMSE for an SNR of 10 dB.	88
4.10	Measurement configuration of the 20-dBi standard-gain horn and planar acquisition surface (drawn to scale).	89
4.11	Magnitude of the measured y -polarized near field at $z = 20 \text{ mm} = 1.14\lambda$. The average edge taper is approximately 34.5 dB.	90
4.12	Phase of the measured y -polarized near field, normalized to π , at $z = 20 \text{ mm} = 1.14\lambda$	91
4.13	NMSE as a function of the undersampling ratio evaluated from near-field measurements of a 20-dBi standard-gain horn over an acquisition area of size $3.5\lambda \times 3\lambda$, at a distance 1.14λ from the horn aperture.	92
4.14	Co-polarized far-field pattern (cut in the plane $\phi = 0^\circ$) at 17.025 GHz of a 20-dBi standard-gain horn reconstructed from planar near-field measurements at $z = 20 \text{ mm} = 1.14\lambda$: (a) non-redundant sampling (94 samples), (b) selection-based method (39 samples). Both results are compared to the reference far field obtained via PWE from all 2365 available near-field samples.	94

Chapter 1

Motivation

The internship in course of which the research for this thesis was conducted was carried out at the Antenna, Propagation and Inductive Coupling Laboratory (LAPCI), which is part of CEA-Leti and located in Grenoble. While CEA-Leti possesses facilities for direct far-field measurements, there is a strong interest in reconstructing the far field from near-field measurements.

This interest is motivated by several factors. First, the capacity of the anechoic chambers required for far-field measurements is limited, and the demand for measurements often exceeds the available resources. To address this limitation, LAPCI has acquired equipment enabling near-field antenna measurements, thereby increasing the overall measurement capacity. Second, near-field measurements offer greater flexibility and mobility, as they do not strictly require a fully anechoic environment and generally require less physical space.

Near-field techniques are particularly advantageous for electrically large antennas operating at high frequencies. As described in Section 2.1, the minimum distance required to ensure far-field conditions depends on both the antenna dimensions and the operating wavelength. For example, a 128-element antenna array operating at 3.5 GHz, representative of configurations used in 5G base stations, would require a far-field measurement distance on the order of 30 m. Such distances exceed the physical dimensions of most conventional anechoic chambers. For satellite communication antennas, which are often larger and operate at even higher frequencies, the required measurement distances can be substantially greater.

Unlike far-field measurements, near-field measurements do not directly provide the quantities of interest. Instead, the far field must be reconstructed from the measured near-field data. The objective of this thesis was therefore to investigate methods for calculating the far field as accurately as possible while accounting for practical constraints. These constraints primarily include the following two aspects:

- **Limited measurement surface:** In particular, for measurements performed on a plane in a Cartesian coordinate system, it is not possible to acquire data over an infinite surface. Therefore, a truncation of the measurement region must be assumed. Additional truncation may occur when certain areas of the antenna’s near field are inaccessible due to mechanical supports, cables, antenna structures, or other obstructions.
- **Reduced number of near field samples:** Under ideal conditions, the near field would be sampled according to the Nyquist sampling theorem, with a spacing of $\lambda/2$. However, each near-field measurement requires a non-negligible acquisition time, and the total measurement duration can become significant as the measurement area increases. Consequently, this thesis aimed to explore and evaluate methods that can significantly reduce the number of required measurements compared to a conventional $\lambda/2$ sampling scheme.

1.1 Near-Field Measurement Procedure

Near field antenna characterization typically relies on complex field data, which is the most common. In a standard near-field measurement setup, a probe is positioned in proximity to the antenna under test (AUT) and is mechanically scanned over a predefined surface, referred to as the scanning surface, which may be planar, cylindrical, or spherical, as illustrated in Figure 1.1. During the scan, the probe collects complex voltage samples (amplitude and phase) at discrete positions, which are recorded together with their precise spatial coordinates.

To fully characterize the vector nature of the radiated field, two separate scans are generally performed: the probe is rotated by 90° around its axis between measurements to capture orthogonal field components. This dual-polarization sampling enables the reconstruction of both the co-polar and cross-polar components of the antenna’s far-field radiation pattern. Notably, no prior knowledge of the AUT’s polarization is required during data acquisition; this information can be accurately inferred from the reconstructed far field through post-processing.

The probe and its support structure must be designed to minimally perturb the electromagnetic field being measured, and the probe’s response must remain stable across different orientations, environmental conditions, and over time. Moreover, the measured quantity is the voltage at the probe terminals, not the electric field directly. The electric field must therefore be reconstructed from the measured voltage using the known probe response, typically characterized through prior calibration.

Once acquired and corrected, the near-field data are transformed into the far-field pattern

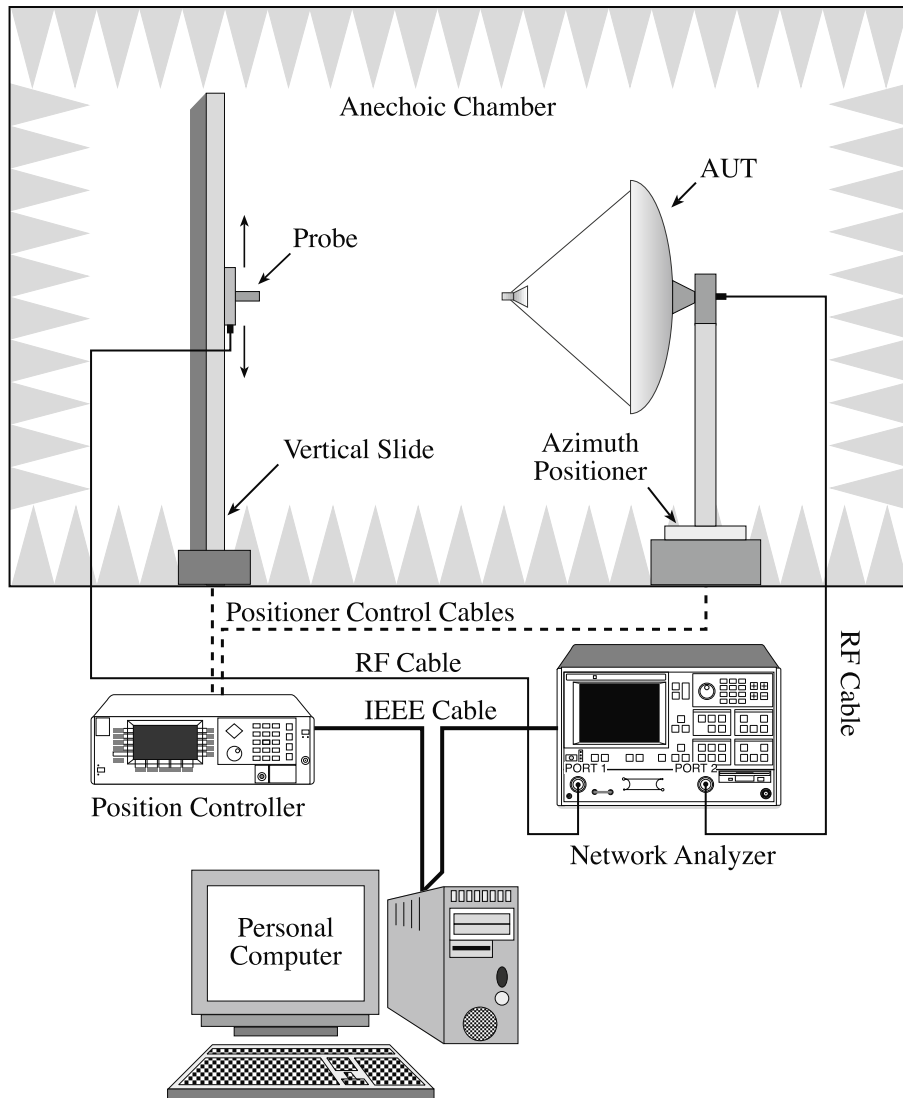


Figure 1.1: Near-field measurement system. Figure reproduced from [1].

using modal expansion techniques. Specifically, the AUT's radiated field is expressed as a superposition of basis functions, plane, cylindrical, or spherical waves, that satisfy the vector wave equation in the source-free region surrounding the antenna. The choice of basis dictates the required scanning surface geometry (planar, cylindrical, or spherical), leveraging the orthogonality of the modes on that surface to compute the expansion coefficients. These coefficients then enable accurate reconstruction of the far-field radiation pattern. Each scanning configuration offers distinct advantages depending on the antenna type and measurement constraints, which justifies the widespread use of multiple near field to far field transformation (NFFFT) approaches in practice [1], [2]. In this work however, only planar scanning geometries will be considered.

1.2 Outline

The following report is organized into five key stages, progressing from theoretical foundations to experimental validation of undersampled antenna measurements:

- **Context and Motivation (Chapter 1):** Introduction to the practical necessity of reconstructing far-field patterns from a reduced number of near-field samples to increase measurement capacity and flexibility.
- **Theoretical Foundations (Chapter 2):** Review of Maxwell’s equations, auxiliary potential functions, and the Plane Wave Expansion (PWE) method as the mathematical basis for electromagnetic field analysis, including the near field to far field transformation. Comparison of “Numerical” vs. PWE methods for field transformation, establishing the “Angle of Validity” (AOV) to account for truncation errors, and detailing the automation of simulation data via the HFSS API.
- **Sampling Schemes and Reconstruction Algorithms (Chapter 3):** Detailed review and implementation of five distinct strategies for near-field sampling and interpolation: Non-redundant sampling, coordinate warping, Igloo sampling (angular projection), minimum-rank interpolation, and greedy point selection. Additionally, a method to reduce the truncation error, based on the Gerchberg-Papoulis Algorithm, is described.
- **Minimizing Samples in a Limited Acquisition Area (Chapter 4):** An adaptation of the non-redundant sampling scheme is introduced to enable its application in realistic scenarios with spatially constrained measurement domains. The performance of all five reviewed sampling and interpolation schemes is then evaluated and compared using simulated data from a 10 dBi horn antenna. The methods are benchmarked in terms of Normalized Mean Square Error (NMSE) and computational complexity under various signal-to-noise ratio (SNR) conditions. Finally, the most computationally efficient approaches, namely the non-redundant, Igloo, and selection-based schemes, are further assessed using measured near-field data from a 20-dBi standard-gain horn antenna.
- **Conclusion (Chapter 5):** Summary of the main findings and technical contributions of this work. This includes the key insights gained regarding sampling and interpolation strategies for near-field measurements, the evaluation of their accuracy and computational efficiency, and the practical implications of the proposed adaptations for spatially constrained measurement scenarios.

Since a comprehensive treatment of all possible near-field measurement configurations, processing methods, and influencing effects would exceed the scope of a master’s thesis,

the present work is subject to the following thematic limitations:

1. **Planar scanning:** Cylindrical, spherical, and planar scanning each present specific advantages and drawbacks, and the associated sampling and transformation techniques differ substantially. This report exclusively considers planar scanning.
2. **Probe coupling:** Due to the spatial proximity between the AUT and the probe, their interaction cannot generally be neglected. The probe may modify the AUT field through reflection and scattering effects [3]. In this work, the measurements were performed using optical probes. These probes limit coupling in practice, and therefore, coupling effects were neglected.
3. **Probe correction:** In practice, the probe response is measured rather than the electromagnetic field directly. This response depends on the radiation characteristics of the probe, even in the absence of coupling. Determining the AUT field from the probe response requires probe correction [4]. Probe correction is not addressed here, and the electromagnetic field is assumed to be known.
4. **Single frequency:** Antenna radiation patterns are commonly analyzed over multiple frequencies. This study does not consider methods that exploit correlations across frequencies and is restricted to single-frequency analysis.
5. **Phaseless measurements:** Accurate phase retrieval of the near field, in addition to amplitude, can be challenging [5]. Various approaches exist for far-field reconstruction from phaseless measurements; however, such methods are not considered in this report.
6. **Positioning error:** Errors in the positioning of the probe relative to the AUT can significantly affect the measured near field. This effect is extensively addressed in the literature but is not considered in this work.

Chapter 2

Theoretical Foundations of Antenna Field Analysis

In order to understand and properly apply the procedures underlying the various sampling and interpolation methods, a solid foundation in electromagnetic radiation and wave propagation is required. This chapter therefore reviews the fundamental principles relevant to antenna field analysis. The discussion begins with Maxwell's equations and proceeds to the introduction of vector potentials and the solution of the Helmholtz equation in planar geometries. Based on these foundations, the computation of near and far fields from prescribed source distributions is derived, and the plane-wave expansion (PWE) framework is introduced and developed, as it constitutes a central tool for the subsequent analysis.

2.1 Field Regions

In the following sections, the terms near field and far field play a central role. They refer to different spatial regions surrounding a radiating source, which in this work is an antenna. The near-field region itself is commonly subdivided into two distinct zones: the reactive near-field region and the radiating near field, also referred to as the Fresnel region.

The reactive near-field region is defined as the volume immediately surrounding the antenna where reactive field components dominate. These components are evanescent, and the relationship between the \mathbf{E} and \mathbf{H} fields is highly complex; the fields are neither orthogonal, nor is there a fixed ratio between their amplitudes.

The boundary between the reactive near-field region and the Fresnel region is commonly approximated by

$$r = 0.62\sqrt{\frac{D^3}{\lambda}}, \quad (2.1.1)$$

where D denotes the largest physical dimension of the antenna and λ is the wavelength.

The Fresnel region constitutes the intermediate zone between the reactive near-field and the far-field (Fraunhofer) region. In this region, radiated field components dominate, implying that evanescent fields are negligible and the \mathbf{E} and \mathbf{H} fields are approximately orthogonal. However, unlike the far field, the angular field distribution still depends on the distance r from the antenna. The transition from the Fresnel region to the Fraunhofer region is typically defined by the distance:

$$r = \frac{2D^2}{\lambda}. \quad (2.1.2)$$

In the Fraunhofer region, four primary conditions are met. At sufficient distance, only the radiation ($1/r$) terms remain significant as higher-order terms fade away. Consequently, the angular field distribution becomes independent of the distance, and only transverse field components persist, causing the ratio of electric to magnetic fields to approach the free-space impedance ($377\ \Omega$). Furthermore, the incoming wavefront appears nearly planar across a receiving antenna's aperture. This planar approximation is governed by the criterion (2.1.2), which ensures that the phase error resulting from the curvature of the actual spherical wavefront does not exceed $\pm 22.5^\circ$ relative to an ideal plane wavefront [6].

The different field regions and their approximate boundaries are illustrated in Figure 2.1.

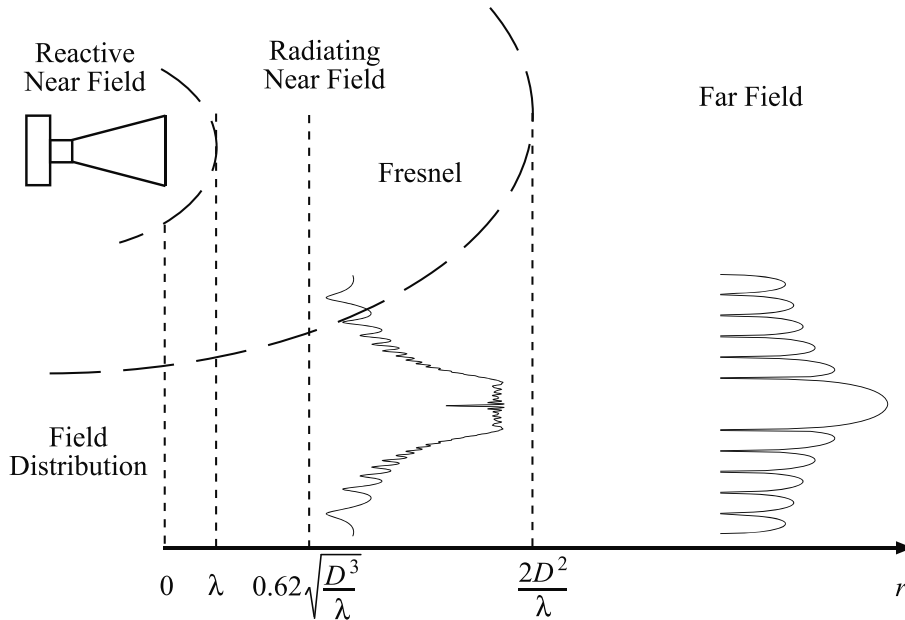


Figure 2.1: Schematic representation of the reactive near field, radiating near field (Fresnel), and far field (Fraunhofer) regions of an antenna, including their commonly used boundary approximations. Figure reproduced from [1].

2.2 Maxwell Equations

Various methods exist to analyze the electromagnetic fields radiated by an antenna. Fundamentally, all such methods are derived from Maxwell's equations:

$$\nabla \cdot \mathbf{E} = \frac{\rho}{\varepsilon_0} \quad (2.2.1a)$$

$$\nabla \cdot \mathbf{B} = 0 \quad (2.2.1b)$$

$$\nabla \times \mathbf{E} = -\frac{\partial \mathbf{B}}{\partial t} \quad (2.2.1c)$$

$$\nabla \times \mathbf{B} = \mu_0 \mathbf{J} + \mu_0 \varepsilon_0 \frac{\partial \mathbf{E}}{\partial t} \quad (2.2.1d)$$

In the above equations, $\mathbf{E}(\mathbf{r}, t)$ denotes the electric field, and $\mathbf{B}(\mathbf{r}, t)$ represents the magnetic flux density. The scalar fields $\rho(\mathbf{r}, t)$ and $\mathbf{J}(\mathbf{r}, t)$ are the free charge density and free current density, respectively. The constants ε_0 and μ_0 are the vacuum permittivity and permeability, which characterize the electric and magnetic properties of free space. The differential operators $\nabla \cdot$ and $\nabla \times$ denote divergence and curl, respectively.

In general scenarios, analytic solutions to these equations are unavailable, and numerical evaluation can be computationally intensive. Exceptions exist only for cases with simple geometric boundary conditions. To analyze more complex structures, various approximations and numerical methods have been developed over recent decades, some of which are detailed below.

2.3 Auxiliary Potential Functions

Auxiliary potential functions are commonly employed as an intermediate step in radiation problems to simplify the calculation of radiated fields (\mathbf{E} and \mathbf{H}) from electric (\mathbf{J}) and magnetic (\mathbf{M}) source currents. Using these potentials is often more tractable than inferring fields directly from source distributions. The most frequently used functions are the magnetic vector potential \mathbf{A} and the electric vector potential \mathbf{F} , defined as follows [6]:

$$\mathbf{H}_A = \frac{1}{\mu_0} \nabla \times \mathbf{A} \quad (2.3.1a)$$

$$\mathbf{E}_F = -\frac{1}{\varepsilon_0} \nabla \times \mathbf{F} \quad (2.3.1b)$$

Here, \mathbf{A} is generated by \mathbf{J} , and \mathbf{F} is generated by \mathbf{M} . These potentials can be expressed as integrals of their respective source currents:

$$\mathbf{A} = \frac{\mu_0}{4\pi} \iiint_V \mathbf{J} \frac{e^{-jkR}}{R} d\nu' \quad (2.3.2a)$$

$$\mathbf{F} = \frac{\varepsilon_0}{4\pi} \iiint_V \mathbf{M} \frac{e^{-jkR}}{R} d\nu' \quad (2.3.2b)$$

where $k = \omega\sqrt{\mu_0\varepsilon_0}$ represents the wavenumber, and R is the distance between the source and observation points. By applying Maxwell's equations (2.2.1) to the definitions in (2.3.1), the total fields are derived as:

$$\begin{aligned} \mathbf{H} = \mathbf{H}_A + \mathbf{H}_F &= \frac{1}{\mu_0} \nabla \times \mathbf{A} - \frac{1}{j\omega\mu_0} \nabla \times \mathbf{E}_F \\ &= \frac{1}{\mu_0} \nabla \times \mathbf{A} - j\omega\mathbf{F} - j\frac{1}{\omega\mu_0\varepsilon_0} \nabla(\nabla \cdot \mathbf{F}) \end{aligned} \quad (2.3.3a)$$

$$\begin{aligned} \mathbf{E} = \mathbf{E}_A + \mathbf{E}_F &= \frac{1}{j\omega\varepsilon_0} \nabla \times \mathbf{H}_A - \frac{1}{\varepsilon_0} \nabla \times \mathbf{F} \\ &= -j\omega\mathbf{A} - j\frac{1}{\omega\mu_0\varepsilon_0} \nabla(\nabla \cdot \mathbf{A}) - \frac{1}{\varepsilon_0} \nabla \times \mathbf{F} \end{aligned} \quad (2.3.3b)$$

Far-Field Approximation

In spherical coordinates, the amplitude of the potentials \mathbf{A} and \mathbf{F} varies as $1/r^n$ (where $n = 1, 2, \dots$). In the asymptotic limit where $r \rightarrow \infty$, higher-order terms ($n \geq 2$) become negligible. For the radiated fields \mathbf{E} and \mathbf{H} , no $1/r$ dependence exists in the radial component, as the contributions from different terms in Equation (2.3.3) cancel out. Consequently, considering only the dominant $1/r$ terms, Equation (2.3.3) simplifies to:

$$E_{A,r} \simeq 0 \quad (2.3.4a)$$

$$E_{A,\theta} \simeq -j\omega A_\theta \quad (2.3.4b)$$

$$E_{A,\phi} \simeq -j\omega A_\phi \quad (2.3.4c)$$

$$H_{F,r} \simeq 0 \quad (2.3.4d)$$

$$H_{F,\theta} \simeq -j\omega F_\theta \quad (2.3.4e)$$

$$H_{F,\phi} \simeq -j\omega F_\phi \quad (2.3.4f)$$

2.4 Plane Wave Expansion

Assuming source-free free space, from Maxwell's equations the so-called Helmholtz equations can be derived [7]:

$$(\nabla^2 + k^2)\mathbf{E} = 0 \quad (2.4.1a)$$

$$(\nabla^2 + k^2)\mathbf{H} = 0 \quad (2.4.1b)$$

Scalar solutions to these equations in Cartesian coordinates are separable and can be represented as elementary plane waves [8]:

$$u_{\alpha\beta}(\mathbf{r}) = \frac{1}{2\pi} e^{j\mathbf{k}\cdot\mathbf{r}} \quad (2.4.2a)$$

$$k_x = \alpha, \quad k_y = \beta, \quad k_z = \gamma \quad (2.4.2b)$$

$$\gamma = \sqrt{k^2 - \alpha^2 - \beta^2} \quad (2.4.2c)$$

The restriction on γ in Equation (2.4.2c) ensures that $\mathbf{k} \cdot \mathbf{k} = k^2$. Vector solutions can be constructed as follows:

$$\mathbf{m}_{\alpha\beta}(\mathbf{r}) = \frac{1}{k} \nabla \times \mathbf{n}_{\alpha\beta}(\mathbf{r}) = u_{\alpha\beta}(\mathbf{r}) \mathbf{e}^1(\hat{\mathbf{k}}) \quad (2.4.3a)$$

$$\mathbf{n}_{\alpha\beta}(\mathbf{r}) = \frac{1}{k} \nabla \times \mathbf{m}_{\alpha\beta}(\mathbf{r}) = u_{\alpha\beta}(\mathbf{r}) \mathbf{e}^2(\hat{\mathbf{k}}) \quad (2.4.3b)$$

$$\hat{\mathbf{k}} \cdot \mathbf{m}_{\alpha\beta}(\mathbf{r}) = \hat{\mathbf{k}} \cdot \mathbf{n}_{\alpha\beta}(\mathbf{r}) = 0 \quad (2.4.3c)$$

$$\mathbf{e}^1(\hat{\mathbf{r}}) = \begin{cases} \frac{\hat{\mathbf{z}} \times \hat{\mathbf{r}}}{\sqrt{1 - (\hat{\mathbf{z}} \times \hat{\mathbf{r}})^2}} & , \hat{\mathbf{r}} \neq \pm \hat{\mathbf{z}} \\ \pm \hat{\mathbf{y}} & , \hat{\mathbf{r}} = \pm \hat{\mathbf{z}} \end{cases} \quad (2.4.3d)$$

$$\mathbf{e}^2(\hat{\mathbf{r}}) = j\hat{\mathbf{r}} \times \mathbf{e}^1(\hat{\mathbf{r}}) \quad (2.4.3e)$$

Since $\mathbf{m}_{\alpha\beta}$ and $\mathbf{n}_{\alpha\beta}$ satisfy the Helmholtz equation (2.4.1), any electromagnetic field in a source-free, linear, homogeneous, isotropic medium can be expressed as a sum of $\mathbf{m}_{\alpha\beta}$ and $\mathbf{n}_{\alpha\beta}$:

$$\mathbf{E}(\mathbf{r}) = \int_{-\infty}^{\infty} \int_{-\infty}^{\infty} [f_{\alpha\beta}^1 \mathbf{m}_{\alpha\beta}(\mathbf{r}) + f_{\alpha\beta}^2 \mathbf{n}_{\alpha\beta}(\mathbf{r})] \frac{d\alpha d\beta}{\gamma k} \quad (2.4.4a)$$

$$j\sqrt{\mu_0/\varepsilon_0} \mathbf{H}(\mathbf{r}) = \int_{-\infty}^{\infty} \int_{-\infty}^{\infty} [f_{\alpha\beta}^2 \mathbf{m}_{\alpha\beta}(\mathbf{r}) + f_{\alpha\beta}^1 \mathbf{n}_{\alpha\beta}(\mathbf{r})] \frac{d\alpha d\beta}{\gamma k} \quad (2.4.4b)$$

for real-valued γ , the differential expression $d\alpha d\beta/\gamma k$ is equivalent to $\sin\theta d\theta d\phi$. Defining $\mathbf{f}(\hat{\mathbf{k}}) = f_{\alpha\beta}^1 \mathbf{e}^1(\hat{\mathbf{k}}) + f_{\alpha\beta}^2 \mathbf{e}^2(\hat{\mathbf{k}})$, the electric field expression becomes:

$$\mathbf{E}(\mathbf{r}) = \frac{1}{2\pi} \int_{-\infty}^{\infty} \int_{-\infty}^{\infty} \mathbf{f}(\hat{\mathbf{k}}) e^{j\mathbf{k}\cdot\mathbf{r}} \frac{d\alpha d\beta}{\gamma k} \quad (2.4.5)$$

This formulation is equivalent to a two-dimensional inverse Fourier transform. Consequently, the plane wave spectrum (or transmitting function) $\mathbf{f}(\hat{\mathbf{k}})$ is the Fourier transform of the electric field:

$$\mathbf{f}(\hat{\mathbf{k}}) = \frac{\gamma k}{2\pi} \int_{-\infty}^{\infty} \int_{-\infty}^{\infty} \mathbf{E}(\mathbf{r}) e^{-j\mathbf{k}\cdot\mathbf{r}} dx dy \quad (2.4.6)$$

From the divergence condition $\nabla \cdot \mathbf{E} = 0$, it follows that $\mathbf{f}(\hat{\mathbf{k}}) \cdot \mathbf{k} = 0$. This implies the plane wave spectrum is determined solely by the tangential field components; specifically, $f_z(\hat{\mathbf{k}})$ can be inferred from $f_x(\hat{\mathbf{k}})$ and $f_y(\hat{\mathbf{k}})$:

$$f_z(\hat{\mathbf{k}}) = -\frac{f_x(\hat{\mathbf{k}})k_x + f_y(\hat{\mathbf{k}})k_y}{k_z} \quad (2.4.7)$$

Far Field Approximation (Stationary Phase)

To simplify the electric field expression for $r \rightarrow \infty$, we assume that the integral in Equation (2.4.7) is dominated by spectral components of $\mathbf{f}(\hat{\mathbf{k}})$ where the phase $\mathbf{k} \cdot \mathbf{r}$ is stationary with respect to first-order variations in k_x and k_y . This is the Stationary Phase method [6]. The stationary point is found by solving:

$$\frac{\partial(\mathbf{k} \cdot \mathbf{r})}{\partial k_x} = \frac{\partial(\mathbf{k} \cdot \mathbf{r})}{\partial k_y} = 0 \quad (2.4.8a)$$

$$\mathbf{k} \cdot \mathbf{r} = r(k_x \sin \theta \cos \phi + k_y \sin \theta \sin \phi + k_z \cos \theta) \quad (2.4.8b)$$

The solution yields:

$$k_x = k_1 = k \sin \theta \cos \phi \quad (2.4.9a)$$

$$k_y = k_2 = k \sin \theta \sin \phi \quad (2.4.9b)$$

Expanding $\mathbf{k} \cdot \mathbf{r}$ via a Taylor series at the stationary point (k_1, k_2) gives $T_2(k_x, k_y) \approx kr + t_1 + t_2$, where the zeroth-order term is kr . Equation (2.4.7) can then be approximated as:

$$\begin{aligned} \mathbf{E}(x, y, z) &\simeq \frac{1}{4\pi^2} \iint \mathbf{f}(k_1, k_2) e^{j(kr + t_1(k_x, k_y) + t_2(k_x, k_y))} dx dy \\ &\simeq \frac{1}{4\pi^2} \mathbf{f}(k_1, k_2) e^{jkr} \iint e^{j(t_1(k_x, k_y) + t_2(k_x, k_y))} dx dy \end{aligned} \quad (2.4.10)$$

Lengthy manipulations show that the integral in Equation (2.4.10) equals $j \frac{2\pi k}{r} \cos \theta$. Applying the Cartesian to spherical transformation yields:

$$\begin{aligned} \mathbf{E}(r, \theta, \phi) &\simeq j \frac{ke^{jkr}}{2\pi r} \cos \theta \left[\hat{\theta} f_\theta + \hat{\phi} f_\phi \right] \\ &\simeq j \frac{ke^{jkr}}{2\pi r} \left[\hat{\theta} (f_x \cos \phi + f_y \sin \phi) + \hat{\phi} \cos \theta (-f_x \sin \phi + f_y \cos \phi) \right] \end{aligned} \quad (2.4.11)$$

2.5 Representation of the Far Field

Co- and Cross-Polarization

To improve the interpretability of the far field radiation patterns, the fields are represented in terms of co- and cross-polarized components rather than the conventional θ - and ϕ -polarized components. For an antenna that radiates a field predominantly polarized along either the x - or y -direction, this representation ensures that the dominant radiation component consistently appears as the co-polarized field, regardless of the azimuthal cut ϕ under consideration. In contrast, when plotting the θ - and ϕ -components directly, the dominant field component alternates between the two depending on the selected cut.

The co- and cross-polarized far-field components are defined as linear combinations of the θ - and ϕ -components, following the formulation proposed by [9]:

$$E_{\text{co}}(\theta, \phi) = \sin \phi E_{\theta}(\theta, \phi) + \cos \phi E_{\phi}(\theta, \phi), \quad (2.5.1a)$$

$$E_{\text{cross}}(\theta, \phi) = \cos \phi E_{\theta}(\theta, \phi) - \sin \phi E_{\phi}(\theta, \phi). \quad (2.5.1b)$$

Normalization

As discussed in Section 2.1, the angular far field distribution is independent of the radial distance r , except for the spherical spreading factor and phase term e^{jkr}/r . To ensure clarity and enable a consistent comparison of results, all presented far field patterns are normalized by this factor, thereby eliminating the explicit r -dependence. The plotted quantities therefore represent the angular field distribution and are given in units of [V].

2.6 Numerical Implementation for Planar Aperture Problems

The theoretical framework described above was applied to a canonical test case: an aperture on an infinite ground plane. This setup allows for relatively simple calculations of near and far fields while remaining applicable to diverse scenarios. The geometry is depicted in Figure 2.2. The field is defined as zero on the ground plane and consists of x and y components within the aperture:

$$\mathbf{E}_{ap}(x, y, z = 0) = [E_x(x, y)\hat{\mathbf{x}} + E_y(x, y)\hat{\mathbf{y}}] \text{rect}(x/2X_S) \text{rect}(y/2Y_S) \quad (2.6.1)$$

Two primary scenarios were investigated:

- A defined field distribution (uniform or \cos^n) over the aperture was used to calculate

near and far fields, serving as a benchmark for testing sampling and interpolation methods. In most simulations, a field distribution of the form $\cos^1(\pi x/2X_S)$ was applied across the aperture, ensuring that half of a cosine period was contained within the aperture extent. This distribution is hereafter referred to as the TE₁₀ mode.

- Near-field data obtained via sampling/interpolation were used to define the aperture distribution for calculating the far field or the near field on a subsequent plane. This approach relies on the principle that the aperture and ground plane can be replaced by an equivalent magnetic current $\mathbf{M}_{eq}(x, y, z = 0) = -2\hat{\mathbf{z}} \times \mathbf{E}_{ap}(x, y)$ [6].

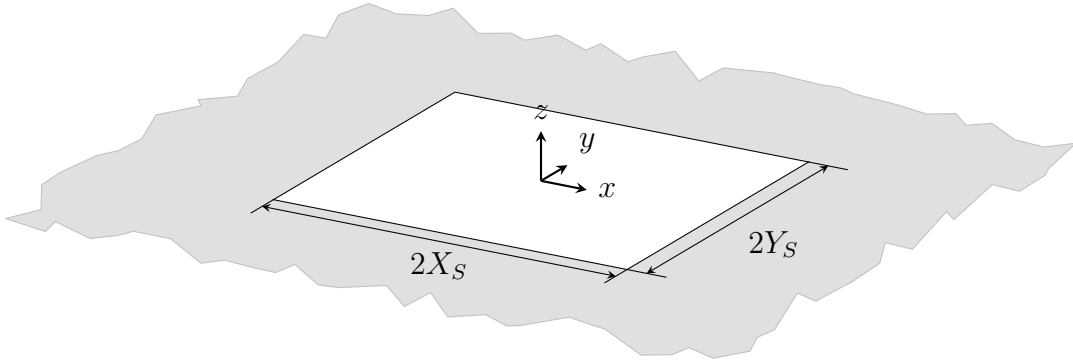


Figure 2.2: Geometry of the canonical aperture on an infinite groundplane.

2.7 Discretization of Source Quantities

While continuous integrals describe the physics conceptually, numerical evaluation typically requires approximating these integrals as finite sums. This is achieved by modeling the continuous spatial quantity as a sum of delta functions centered within respective unit cells. For a magnetic source current restricted to x and y components on a plane, this is expressed as:

$$\mathbf{M}(x, y) = \sum_{m,n} \mathbf{M}(m, n) \delta(x - x_m) \delta(y - y_m) \quad (2.7.1)$$

This generalizes to three dimensions as:

$$\mathbf{M}(x, y, z) = \sum_{m,n,o} \mathbf{M}(m, n, o) \delta(x - x_m) \delta(y - y_n) \delta(z - z_o) \quad (2.7.2)$$

To derive the far field expression, we consider the contribution of a single spatial component of the source current. Since the far field is a linear function of the sources, results can be generalized. Assuming $\mathbf{J} = \mathbf{0}$ and $\mathbf{M} = M_x \hat{\mathbf{a}}_x$, the θ component of the electric far field is

[6]:

$$E_{\theta,ff} = -\frac{jk e^{-jkr}}{4\pi r} (L_\phi + \eta N_\theta) \quad (2.7.3a)$$

$$L_\phi = \iiint [-M_x \sin \phi + M_y \cos \phi] e^{jk(ux'+vy'+wz')} dx' dy' dz' \quad (2.7.3b)$$

$$N_\theta = \mathbf{0} \quad (2.7.3c)$$

$$u = \sin \theta \cos \phi \quad (2.7.3d)$$

$$v = \sin \theta \sin \phi \quad (2.7.3e)$$

$$w = \cos \theta \quad (2.7.3f)$$

Substituting the discretized source definition into the integral yields:

$$\begin{aligned} E_{\theta,ff} &= -\frac{jk e^{-jkr}}{4\pi r} \iiint -M_x \sin \phi e^{jk(ux'+vy'+wz')} dx' dy' dz' \\ &= -\frac{jk e^{-jkr}}{4\pi r} \\ &\quad \cdot \iiint \left[\sum_{m,n,o} -M_x(m,n,o) \delta(x' - x_m) \Delta x \delta(y' - y_n) \Delta y \delta(z' - z_o) \Delta z \right] \\ &\quad \cdot \sin \phi e^{jk(ux'+vy'+wz')} dx' dy' dz' \\ &= \frac{jk e^{-jkr}}{4\pi r} \sum_{m,n,o} -M_x[m,n,o] \sin(\phi) e^{jk(ux_m+vy_n+wz_o)} \Delta x \Delta y \Delta z \end{aligned} \quad (2.7.4)$$

This essentially replaces integrals with sums. In practice, these equations were utilized with a quantization step of $\lambda/4$, as a compromise between precision and computational complexity; this value is used throughout unless otherwise stated.

2.8 Calculation of the Near Field

The near field is calculated by first defining the equivalent magnetic source current as per Equation (2.7.1). Combining Equation (2.3.2b) and Equation (2.3.3b) for the specific setup ($E_z = 0$, $\mathbf{J} = 0$) gives:

$$\begin{aligned} \mathbf{E}(x, y, z) &= -\frac{1}{\epsilon_0} \nabla_{\mathbf{r}} \times \mathbf{F}(x, y, z) \\ &= -\frac{1}{4\pi} \nabla_{\mathbf{r}} \times \int_{-X_S}^{X_S} \int_{-Y_S}^{Y_S} \mathbf{M}(x', y') \frac{e^{-jkR}}{R} dy' dx' \\ &= -\frac{1}{4\pi} \nabla_{\mathbf{r}} \times \sum_{m,n} \mathbf{M}[x'_m, y'_n] \frac{e^{-jkR}}{R} \Delta x' \Delta y' \\ &= -\frac{1}{4\pi} \sum_{m,n} \mathbf{M}[x'_m, y'_n] \times \left(\nabla_{\mathbf{r}} \frac{e^{-jkR}}{R} \right) \Delta x' \Delta y' \end{aligned} \quad (2.8.1)$$

where

$$R = \sqrt{(x - x')^2 + (y - y')^2 + z^2} \quad (2.8.2)$$

and the analytic gradient of the e^{-jkR}/R term is:

$$\nabla_{\mathbf{r}} \frac{e^{-jkR}}{R} = \begin{pmatrix} x - x' \\ y - y' \\ z \end{pmatrix} \frac{-e^{-jkR}}{R^2} (jk + R^{-1}) \quad (2.8.3)$$

With these expressions, the individual components of $\mathbf{E}(x, y, z)$ can be obtained through straightforward, albeit tedious, manipulations.

Alternatively, the Plane Wave Expansion (PWE) method can be employed [10]. In the first step, the near-field spectrum $\mathbf{f}(k_x, k_y)$ is computed using a fast Fourier transform (FFT), as defined in Equation (2.8.4), applied separately to the x - and y -components of the field. The near-field data must be sampled on a regular Cartesian grid of size $N_x \times N_y$ with spatial sampling intervals Δx and Δy , centered at $x = y = 0$:

$$\mathbf{f}'(m\Delta k_x, n\Delta k_y) = \sum_{p=0}^{N_x-1} \sum_{q=0}^{N_y-1} \mathbf{E}(x_p, y_q) e^{2\pi j(mp/N_x + nq/N_y)} \Delta x \Delta y \quad (2.8.4)$$

This operation yields $N_x \times N_y$ samples of the spectrum with spectral spacing $\Delta k_x = 2\pi/(N_x\Delta x)$ and $\Delta k_y = 2\pi/(N_y\Delta y)$. To account for the distance between the measurement plane and the reference plane z_0 , the spectrum is back-propagated according to

$$\mathbf{f}(m\Delta k_x, n\Delta k_y) = \mathbf{f}'(m\Delta k_x, n\Delta k_y) e^{jk_z z_0} \quad (2.8.5)$$

where k_z is defined in Equations (2.4.2b) and (2.4.2c). Subsequently, evanescent spectral components satisfying $k_x^2 + k_y^2 > k^2$ are suppressed, then the electric field can be calculated on an arbitrary x-y-plane by propagating the spectrum with the respective value of $z = z_1$ and calculating the inverse 2D Fourier transform

$$\mathbf{E}(x_p, y_q) = \frac{1}{N_x N_y \Delta x \Delta y} \sum_{m=0}^{N_x-1} \sum_{n=0}^{N_y-1} \mathbf{f}''(m\Delta k_x, n\Delta k_y) e^{-2\pi j(mp/N_x + nq/N_y)} \quad (2.8.6a)$$

$$\mathbf{f}''(m\Delta k_x, n\Delta k_y) = \mathbf{f}(m\Delta k_x, n\Delta k_y) e^{-jk_z z_1} \quad (2.8.6b)$$

However, significant zero padding is required when computing the plane wave spectrum. Insufficient zero padding leads to pronounced ripples in the resulting near-field distribution. Those ripples are caused by the jump discontinuity at the edge of the aperture and are known as the Gibbs phenomenon. This effect is illustrated in Figure 2.3, where the near field obtained using the method described in (2.8.1) (hereafter referred to as the ‘‘Numerical’’ method) is compared with the result obtained using the plane wave expansion

with zero padding equal to four times the size of the original aperture. Further increasing the zero padding causes the plane-wave-based solution to converge toward the “Numerical” result.

The code used to compute the near field with the Numerical method was fully vectorized, replacing explicit for-loops with tensor operations. The resulting tensors are five-dimensional, with each dimension corresponding to:

1. The three spatial components of the field: x , y , and z
2. The x -coordinate of the source domain
3. The y -coordinate of the source domain
4. The x -coordinate of the observation domain
5. The y -coordinate of the observation domain

For more than a few hundred observation points, the memory requirements became substantial. To mitigate this, the computation was divided into chunks of 100 observation points, which were processed sequentially. These chunks were distributed across all available CPU cores to enable parallel execution. With this approach, the total computation time remained reasonable. Consequently, the Numerical method for near field calculation was preferred, as the Fourier-transform-based approach is susceptible to ripple artifacts if the zero padding is not chosen sufficiently large.

2.9 Near- to Far Field Transformation

The near field to far field transformation (NFFFT) is a central element of the methods addressed in this document. In all considered approaches, the NFFFT represents the final processing step that converts field distributions, either measured on a planar near field surface or defined on an aperture plane, into the corresponding far-field representation, which constitutes the quantity of interest. Furthermore, the NFFFT applied to near-field samples on a rectangular grid serves as the reference method against which the investigated techniques are evaluated. Consequently, after outlining the procedure used to compute the NFFFT, the influence of selected transformation parameters is examined. The NFFFT can be applied both to near-field data measured on a plane at $z > 0$ and to field distributions directly defined on an aperture plane at $z = 0$.

2.9.1 Calculation of the NFFFT

For far-field computation, particularly when simulation data are available, a Fourier transform based approach is employed instead of numerical integration of electromagnetic

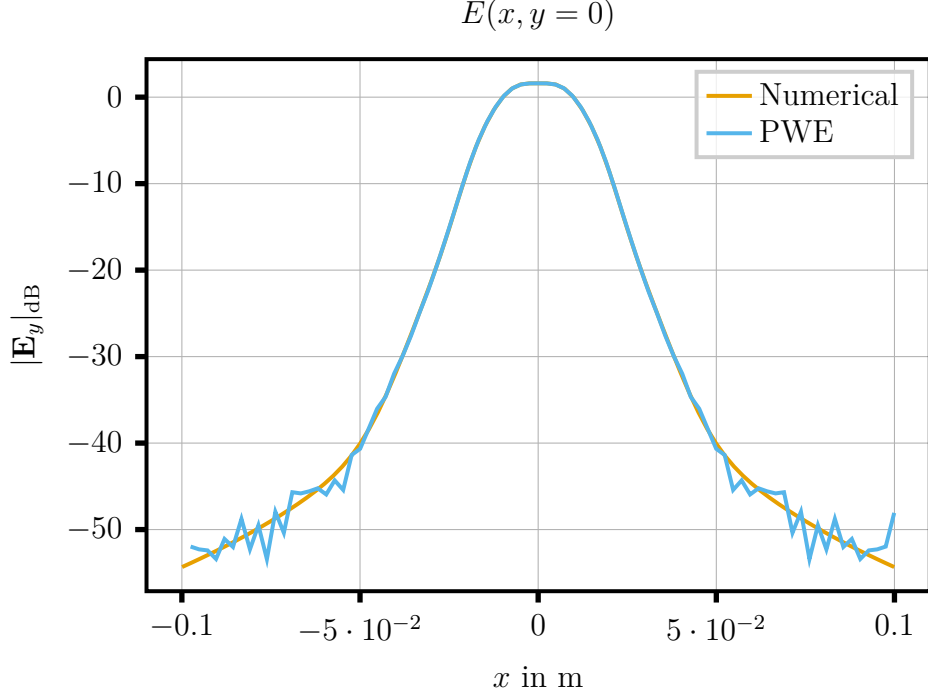


Figure 2.3: Near field of a canonical aperture ($X_S = 2.5\lambda$, $Y_S = 1.5\lambda$, TE_{10} mode) evaluated at a distance of 2λ , calculated using the method described in (2.8.1) (Numerical method) and using the plane wave expansion.

potentials. The Fourier-based method provides exact results, reduced computational effort, and a more compact implementation.

In the first step, the near-field spectrum $\mathbf{f}(k_x, k_y)$ is computed and back propagated to the plane $z = 0$, as described in Equations (2.8.4) and (2.8.5). The resulting spectrum, with the evanescent components suppressed, is then bilinearly interpolated at the spectral coordinates corresponding to the desired far field direction (θ, ϕ) :

$$k_x = k \sin \theta \cos \phi, \quad k_y = k \sin \theta \sin \phi. \quad (2.9.1)$$

Finally, the relation given in Equation (2.4.11) is used to compute the far-field components.

2.9.2 Influence of the Sampling Step Size

A key parameter of the FFT-based NFFFT is the spatial sampling interval of the near-field data. If the sampling step size is too large, spectral components associated with large elevation angles θ cannot be accurately recovered. Only when the Nyquist sampling criterion [11], corresponding to a spatial sampling interval of $\lambda/2$, is satisfied can the far field over the entire upper hemisphere be reconstructed. This behavior is illustrated in Figures 2.4 and 2.5. The first example considers a canonical aperture in an infinite ground plane, while the second example corresponds to the simulation of a horn antenna.

In both cases, far-field results obtained from near-field data sampled with different spatial resolutions are compared with the analytical solution and the full-wave simulation results, respectively. Further reducing the sampling interval below $\lambda/2$ yields only marginal gains in accuracy; however, it can help mitigate undesirable effects introduced by truncation. Therefore, when computationally feasible, a $\lambda/4$ grid is used for far field calculations.

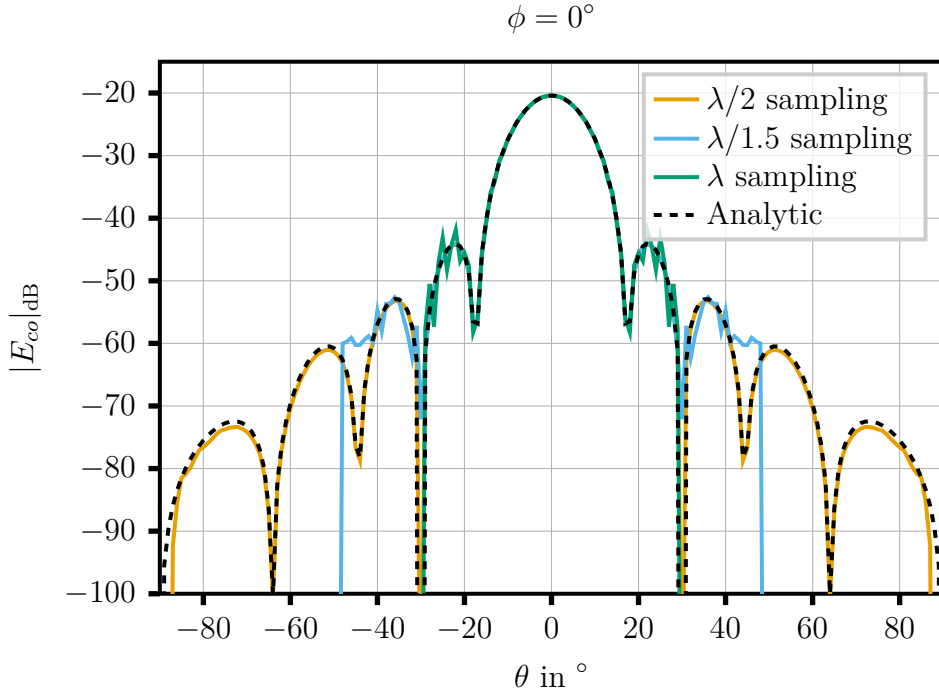


Figure 2.4: Far field of a canonical aperture (size $5\lambda \times 3\lambda$, TE_{10} mode) calculated from the near-field distribution over an area of $750\lambda \times 450\lambda$ at a distance of $z = 17.5\lambda$ using the Fourier transform method for different spatial sampling intervals.

2.9.3 Truncation Error and Reliable Region

In practice, the surface over which near-field measurements are obtained is necessarily finite. For planar measurement geometries, this finite extent results in incomplete coverage of the upper hemisphere, which introduces errors in the reconstructed far-field pattern. These errors are referred to as truncation errors. Truncation errors predominantly affect a limited angular region, while the far field remains accurate elsewhere. The angular domain in which the reconstructed far field can be considered reliable is referred to as the reliable region.

The reliable region is defined as the angular domain in which the far-field pattern reconstructed from planar near-field measurements can be regarded as accurate. This region is bounded by the angle of validity (AOV), denoted θ' , which generally depends on the azimuth angle ϕ . The concept originates from the assumption that the antenna can be represented by an equivalent plane aperture of known geometry and position, where

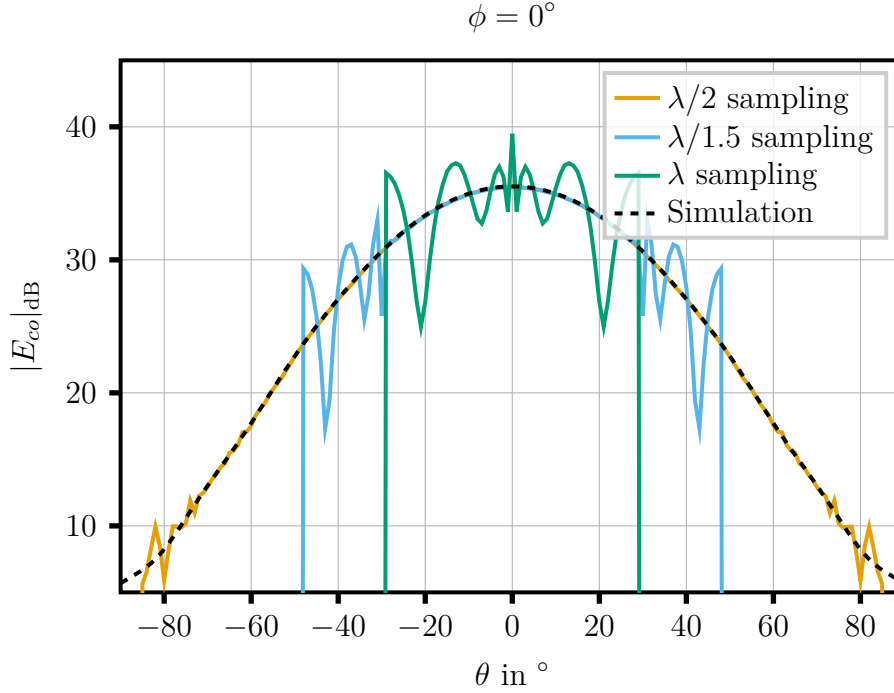


Figure 2.5: Far field of a 10 dBi standard-gain horn calculated from the near-field distribution over an area of $166\lambda \times 166\lambda$ at a distance of $z = 2.89\lambda$ using the Fourier transform method for different spatial sampling intervals.

the tangential electric and magnetic fields are negligible outside the aperture. A Cartesian coordinate system is defined such that the aperture lies in the x - y -plane, with the z -axis pointing away from the antenna. Using the plane-wave spectrum (PWS) formulation, the truncation error is small when the dominant contribution to the far field in a given direction comes from within the scanned region. However, if the associated stationary-phase point (i.e., the intersection of the observation ray with the scan plane) falls outside the measured area, the truncation error becomes dominant, and the far field estimate is no longer reliable. Applying this reasoning across all source points in the aperture leads to the definition of the reliable region: it is bounded by rays that connect the edges of the equivalent aperture to the corners of the scan area. A schematic illustration of this is shown in Figure 2.6.

For the common case of centered, rectangular source domain and scan areas, this region forms a prismatoid, with angular limits in the principal planes:

$$\theta'_x = \tan^{-1} \left(\frac{x_O - x_S}{2z} \right), \quad \theta'_y = \tan^{-1} \left(\frac{y_O - y_S}{2z} \right) \quad (2.9.2)$$

where x_O, y_O is the extent of the scan area and x_S, y_S is the extent of the source domain.

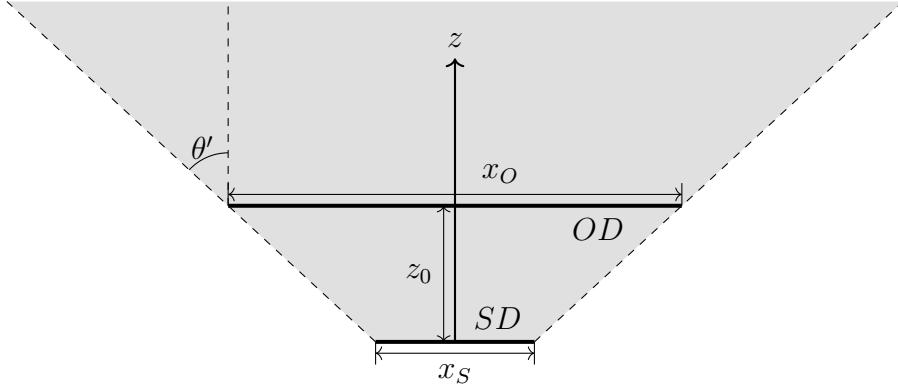


Figure 2.6: Schematic definition of the angle of validity θ' . The resulting reliable region is indicated by the gray shading.

The corresponding spectral reliable region is given by [12]

$$\left\{ \frac{k_x^2}{(k \sin \theta'_x)^2} + \frac{k_y^2}{k^2} < 1 \right\} \cap \left\{ \frac{k_x^2}{k^2} + \frac{k_y^2}{(k \sin \theta'_y)^2} < 1 \right\}, \quad (2.9.3)$$

where k denotes the wavenumber. This spectral region defines the range of spatial frequencies for which the plane-wave spectrum, and consequently the reconstructed far field, can be considered reliable. The same reliable region applies to both electric and magnetic fields. Furthermore, its angular extent remains unchanged under propagation, as propagation only introduces a phase factor in the spectral domain.

The reliable region is clearly illustrated in Figure 2.7, where the far field reconstructed from a finite planar measurement surface is compared to the analytical solution for a canonical rectangular aperture of size $5\lambda \times 3\lambda$, excited with a TE_{10} mode. The near-field samples are obtained on a $\lambda/4$ grid over an area of $17\lambda \times 16\lambda$ at a distance of 17.5λ from the aperture. This configuration corresponds to an angle of validity in the depicted x -plane ($\phi = 0^\circ$) of $\theta'_x = 39.7^\circ$. Within the angle of validity, the reconstructed far field agrees closely with the analytical solution, with only negligible deviations. Outside the AOV, however, the far-field reconstruction rapidly deteriorates, and no longer represents the true radiation pattern.

A similar behavior is observed when simulated near-field data of a 10 dBi standard-gain horn are used, as shown in Figure 2.8. The near-field samples are taken on a $\lambda/4$ grid over an area of $17\lambda \times 11\lambda$ at a distance of 10.75λ . This measurement configuration corresponds to an angle of validity in the depicted x -plane ($\phi = 0^\circ$) of $\theta'_x = 55.0^\circ$. Consistent with the canonical example, the reconstructed far-field pattern exhibits good agreement with the reference solution within the AOV, whereas substantial deviations are observed beyond this angular range. Noticeable discrepancies already arise near the AOV boundary, indicating a gradual degradation of accuracy as the limit is approached. Despite this behavior,

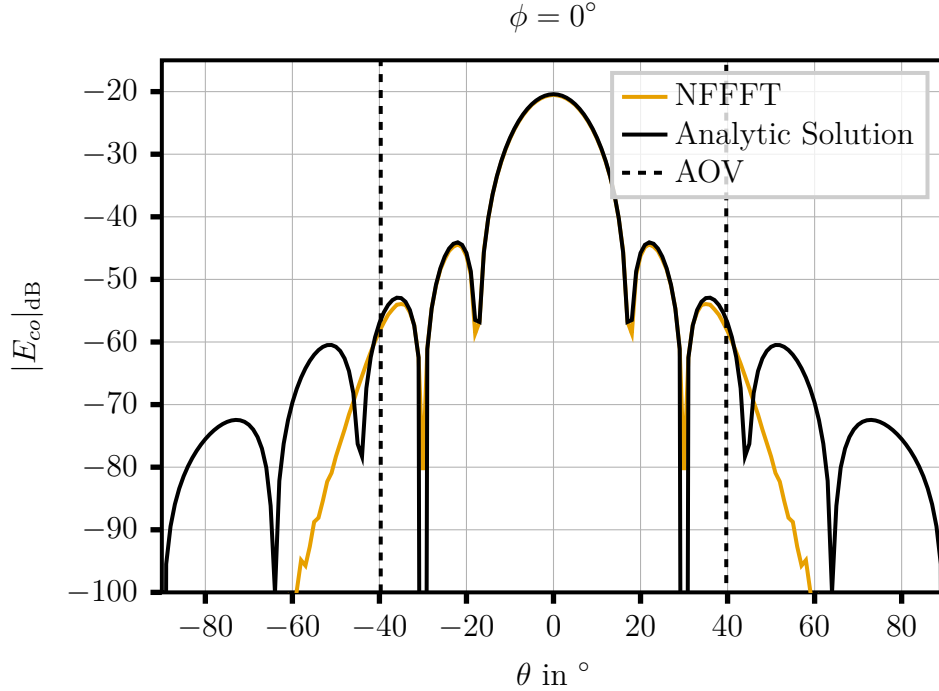


Figure 2.7: Comparison between the analytically computed far field of a canonical rectangular aperture ($5\lambda \times 3\lambda$, TE_{10} mode) and the far-field reconstructed from a finite planar measurement surface of $17\lambda \times 16\lambda$ at a distance of 17.5λ . The resulting angle of validity in the x -plane is $\theta'_x = 39.7^\circ$.

the AOV provides a reliable criterion for estimating the angular region over which the reconstructed far-field results can be considered accurate.

2.10 Generation of Simulation Data

Full-wave simulations were conducted using Ansys HFSS to generate realistic data for testing. To streamline the process, a set of functions was developed using the HFSS API to automate the generation and import of field data at specific spatial coordinates. This reduced manual effort and potential human error. The workflow is depicted in Figure 2.9.

Two analogous functions were implemented for the generation and import of near field and far-field data, following the same procedural workflow. The primary difference between the two lies in the simulation setup: near-field simulations require a list of arbitrary Cartesian observation points, whereas far-field simulations are defined by angular ranges and step sizes in elevation and azimuth.

The implementation of these API-based functions proved more time-consuming than initially expected due to limited documentation. Available resources consist mainly of brief and sparse code examples, which provide insufficient guidance given the complex class hierarchy of the API. In addition, changes to the API in the past have rendered many

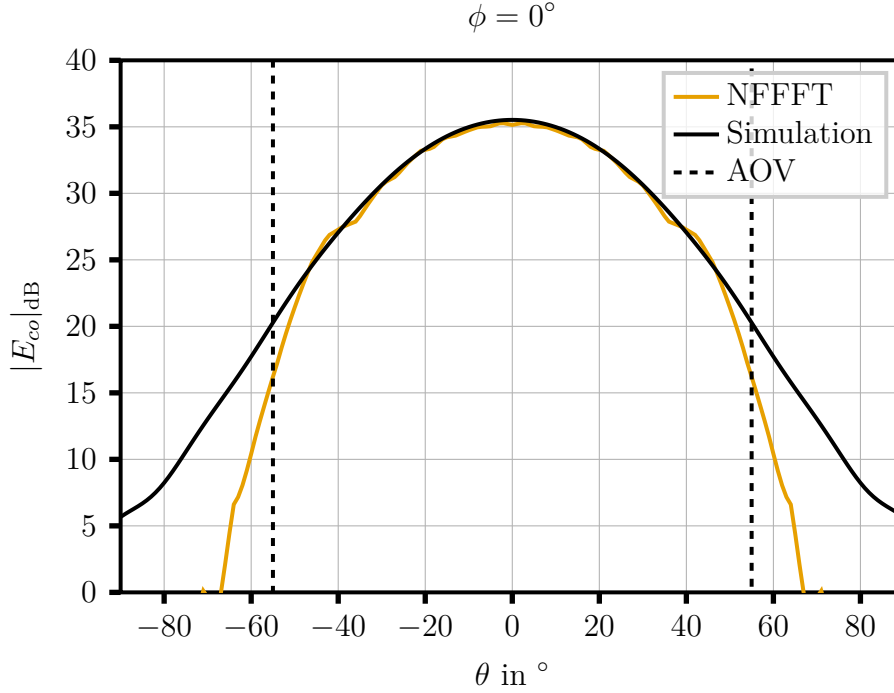


Figure 2.8: Comparison between the simulated far field of a 10 dBi standard-gain horn and the far field reconstructed from a finite planar measurement surface of $17\lambda \times 11\lambda$ at a distance of 10.75λ . The resulting angle of validity in the x -plane is $\theta'_x = 55.0^\circ$.

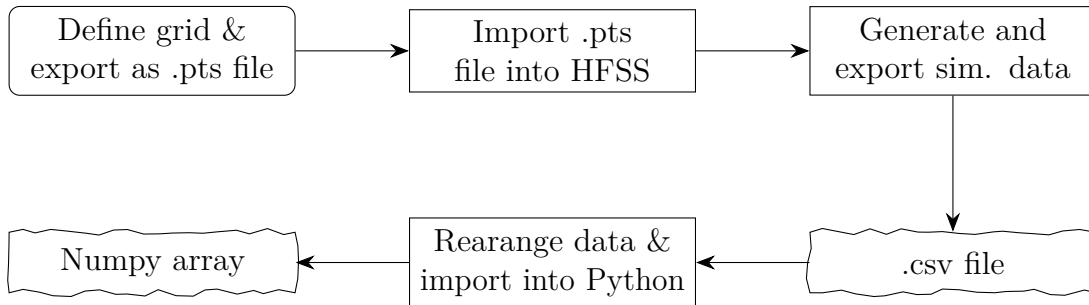


Figure 2.9: Workflow of generating and importing simulation data into Python.

third-party code snippets obsolete. Debugging was particularly challenging, as errors frequently resulted in silent failures without meaningful diagnostic output. Consequently, the development process relied heavily on iterative trial-and-error over several days.

Despite the extended development effort, the resulting functions substantially improve efficiency. Once implemented, they enable new experimental configurations to be simulated and their corresponding data to be imported within approximately ten seconds. As these operations are performed multiple times per day, the cumulative time savings compared to manual processing are significant.

2.11 Conclusion

This section provided a recap of the fundamentals of wave propagation and introduced the notations and approximations used to express electromagnetic fields in a simplified form. A central concept is the plane wave expansion, which represents an arbitrary field as a superposition of plane waves. Subsequently, the procedures used to compute near field and far-field distributions for all simulations and experiments presented in this report were described. These computations are based on modeling a near-field distribution within an aperture located on an infinite ground plane. The presented results demonstrate that both the Numerical approach and the plane wave expansion yield identical near-field patterns, and that in the far field, the results obtained from the plane wave expansion are in agreement with analytical solutions.

Chapter 3

Sampling Schemes and Reconstruction Algorithms

After introducing the principles of wave propagation and the transformation from near-field samples to the far field, the central question of this work can now be addressed: how can an accurate far-field pattern be obtained from as few near-field samples as possible within a confined measurement area? To answer this question, the existing literature was reviewed, and five representative approaches were selected for a detailed study and a comparative analysis, in order to evaluate to what extent they reduce the required number of near-field samples without significantly degrading the far-field reconstruction.

Reducing the measurement time in planar near field antenna characterization has been a major research objective for several decades. While the classical Nyquist sampling criterion, derived from the spatial bandwidth of the electromagnetic field, guarantees accurate reconstruction, it often results in a prohibitive number of samples, particularly for electrically large antennas or high operating frequencies. Consequently, numerous advanced sampling strategies have been developed to decrease the number of acquisition points while preserving the fidelity of the far-field pattern.

Among the most rigorous contributions are the Non-Redundant Sampling Representations introduced by O.M. Bucci, C. Gennarelli, and F. D'Agostino [13], [14], [15], [16]. By formalizing the concept of the Number of Degrees of Freedom (NDF) of the radiated field and modeling the antenna by means of a suitable rotational ellipsoid, they demonstrated that spatially varying sampling steps in plane-polar geometry allow the number of measurements to be matched to the actual information content of the field rather than to its maximum spatial bandwidth.

Parallel to these approaches, relying on the emitters' geometry, M.A. Maisto, R. Solimene, and R. Pierri developed sampling schemes based on Singular Value Optimization (SVO)

and warping strategies [17], [18], [19]. By exploiting the spectral properties of the radiation operator a coordinate transformation is introduced, to increase the sampling density in the relevant regions.

F. Ferrara, C. Gennarelli and R. Guerriero [1] merge elements of both concepts by adopting a source model analogous to that in [16], while introducing a parametrization of the measurement domain that is conceptually similar to the warping strategies proposed in [18].

An alternative strategy is the adaptive near field acquisition [20], where the measurement system dynamically adjusts the sampling density during the scan. Regions with strong field variations are sampled more densely, while areas where the measured near field is smoother are sampled more sparsely according to a predefined decision threshold. The achievable reduction in measurement points therefore depends directly on the actual near-field distribution.

Another adaptive scheme is proposed in [21], where an initially sparse set of samples is classified using K-means clustering. The associated Voronoi cell areas and local field gradients are evaluated and combined through weighted criteria to distinguish between regions requiring dense or coarse sampling.

A different philosophy is followed by sparse nonuniform sampling schemes such as the igloo method [22]. Here, sampling points uniformly distributed over half a spherical surface are mapped onto the planar near field measurement surface. The near field is then reconstructed by interpolation on a uniformly spaced grid.

Recently, compressive sensing techniques have been introduced into antenna measurements [23], [24]. By promoting sparsity in the harmonics or the distribution of the near field, these probabilistic approaches enable accurate reconstruction from sub-Nyquist, often randomly distributed sampling sets, provided that appropriate sparsity conditions are fulfilled. Closely related is the minimum-complexity interpolation framework of [25], which does not rely on explicit source information but instead enforces general electromagnetic field properties such as low rank (minimum complexity) and smoothness to estimate the field from incomplete data.

Finally, a greedy selection-based strategy has been proposed in the form of the maximum noise propagation error (MNPE) algorithm [19]. This approach aims at the reconstruction of an equivalent surface current of the source. Starting from a densely populated initial grid, sampling points are selected sequentially such that the propagation of measurement noise into the reconstructed current is minimized. The procedure stops when the introduction of further measurement points does not yield a significant additional reduction of the noise factor.

Given the vast amount of existing literature, including numerous variations of nonuniform and interpolation-based grids, an exhaustive review is beyond the scope of this work. Instead, the following sections focus on five representative schemes, Non-redundant sampling [16], warping-based sampling [17], [18], Igloo sampling [22], minimum-complexity interpolation [25], and the selection-based approach [19], which together span deterministic geometry-driven, sparse, and regularization-based strategies.

In contrast to the extensive literature on sampling strategies, algorithms specifically designed to mitigate truncation errors appear less frequently and exhibit a narrower variety of approaches. Nevertheless, addressing the inaccuracies arising from limited measurement domains remains critical for practical applications. Consequently, the Gerchberg-Papoulis Algorithm (GPA) [12], [26] was selected as a representative method in this category; it is subsequently analyzed in detail and experimentally validated to assess its efficacy in reducing reconstruction errors caused by aperture truncation.

3.1 Non-Redundant Near-Field Sampling

The first method for sampling and interpolating near-field data is based on the seminal works of Bucci et al. [13], [14], [15]. These publications are widely considered the most significant in the field and are cited in the vast majority of subsequent research. The approach is grounded in a comprehensive analysis of electromagnetic fields and their degrees of freedom depending on the emitter’s geometry [13]. Subsequently, the spatial bandwidth is derived [14], which is the foundation of the introduced parametrization that aims to make the spectral wavenumber increment across the samples constant, which allows uniform sampling and cardinal sinc interpolation [15]. The application of this approach to plane-polar near-field measurements [16] was implemented and tested.

3.1.1 Degrees of Freedom of a Scattered Field

To minimize near-field sampling effectively, it is necessary to determine the minimum number of samples required to fully describe the field of an emitter, this quantity is referred to as degrees of freedom (DoF). The derivation of these DoF is the primary focus of [13]. The study examines how accurately an electric field \mathbf{E} associated with a scattering system within a sphere B (see Figure 3.1) can be approximated by a set of functions $\mathcal{B}_w = \{\mathbf{B}_w\}$ that are bandlimited to a bandwidth w .

The approximation is defined by the separation between the two sets:

$$\delta_w = \delta(\mathcal{E}, \mathcal{B}_w) = \sup_{\mathbf{E}} \inf_{\mathbf{B}_w} \|\mathbf{E} - \mathbf{B}_w\| \quad (3.1.1)$$

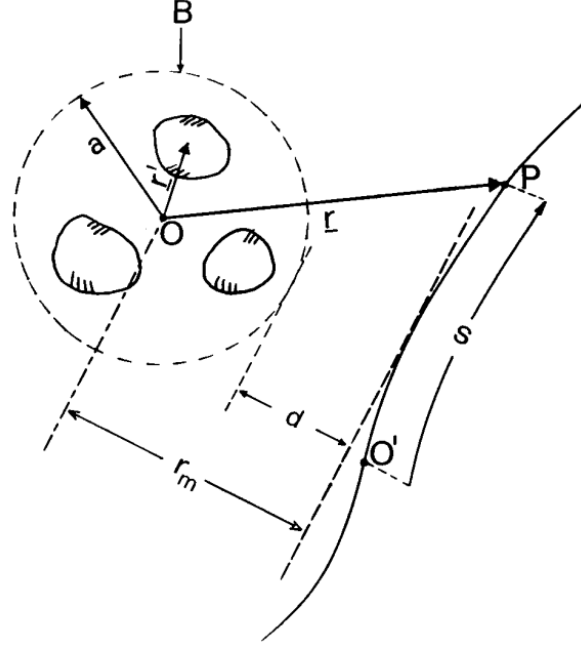


Figure 3.1: Geometry of scatterers within the sphere B of radius a and measurement curve s . Figure reproduced from [14].

here $\mathcal{E} = \{\mathbf{E}\}$. A critical bandwidth value is identified as:

$$W_0 \approx \beta a / r_m \quad (3.1.2)$$

where β is the wavenumber, a the radius of the sphere B that contains the scattering system and r_m the minimum distance of S from the origin O . For $w \ll W_0$ the separation is large while for $w \gg W_0$ the separation is small. The separation as a function of the bandwidth $\delta_w(w/W_0)$ approaches a step function when $\beta a \rightarrow \infty$. Therefore, the separation between \mathcal{E} and \mathcal{B}_w can be controlled by a parameter $\chi = w/W_0$. For χ slightly larger than 1 the separation (3.1.1) becomes negligible.

The assessment of the minimum cardinality of the basis function set, i.e. DoF, is further explored in [14] by analyzing the field over a measurement curve C . For a field $\mathbf{E}(s)$ observed on a curve C with coordinate $s \in (-S, S)$, we consider an n -dimensional set of functions $\mathcal{L}_n = \{\mathbf{L}_n\}$. The separation

$$\delta(\mathcal{E}, \mathcal{L}_n) = \sup_{\mathbf{E}} \inf_{\mathbf{L}_n} \|\mathbf{E} - \mathbf{L}_n\| \quad (3.1.3)$$

tends to zero as $n \rightarrow \infty$. An upper bound is established via the triangle inequality:

$$\delta(\mathcal{E}, \mathcal{L}_n) \leq \delta(\mathcal{E}, \mathcal{U}_w) + \delta(\mathcal{E}, \mathcal{L}_n) \quad (3.1.4)$$

where \mathcal{U}_w is the set of functions bandlimited to w with a norm not larger than 1 between

$(-\infty, \infty)$. The first term of the upper bound in (3.1.4) turns out to be identical to (3.1.1), which can be approximated as a step function from high to low at $w \approx W_0$. It can be shown that the second term is also a step-like function, but from low to high around $w \approx W = \pi n/2S$. If the cardinality of \mathcal{L}_n is $n = N_0$, the transition of both terms in (3.1.4) coincides, where N_0 is defined as:

$$N_0 = \frac{2SW_0}{\pi r_m} \approx \frac{2S\beta a}{\pi r_m} \quad (3.1.5)$$

Given dimensions a , r_m and S , the bandwidth W_0 and Nyquist number N_0 must first be determined. If w is selected to be slightly larger than W_0 and n slightly larger than N_0 , the upper limit of the separation between \mathcal{E} and \mathcal{L}_n , as presented in Equation (3.1.4), is negligibly low.

3.1.2 Optimal Parametrization of a Measurement Curve

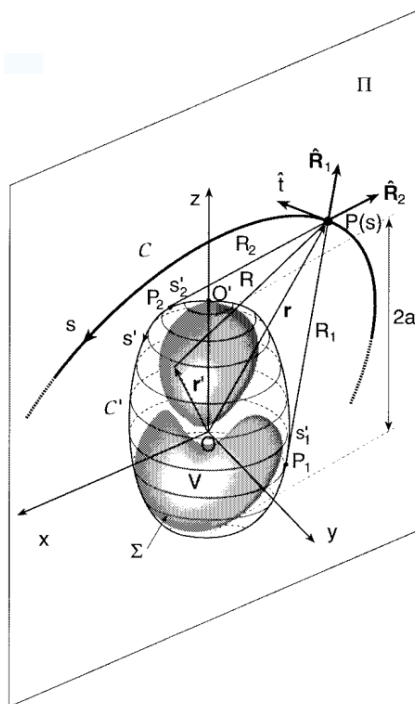


Figure 3.2: Geometry of scatterer and measurement curve in three dimensions. Figure reproduced from [15].

The previous subsections established the number $n \geq N_0$ and bandwidth $w \geq W_0$ of functions required to approximate a field over a curve C . In practice, this knowledge can only be leveraged if the sampling positions are determined such that each sample is non-redundant. If n measurements were taken at arbitrary positions, one might acquire redundant information in regions of C where the spatial sampling rate is excessive, while lacking crucial information for precise field reconstruction in regions where samples are

spaced too far apart.

In [15], this issue is addressed by parameterizing the measurement curve via ξ . It is noteworthy that the geometry under consideration differs from the previous case, as the volume Σ enclosing the scattering system is not assumed to be a sphere, but rather a domain exhibiting rotational symmetry with respect to the z-axis. Furthermore, the measurement curve is assumed to lie on a meridian plane Π . The intersection between Π and Σ is denoted as C' . This is depicted in Figure 3.2. The electric field is expressed in the parametrization $\mathbf{E}(\mathbf{r}(\xi)) = \mathbf{E}(\xi)$. Additionally, a “reduced” field is introduced:

$$\mathbf{F}(\xi) = \mathbf{E}(\xi) \exp[j\gamma(\xi)] \quad (3.1.6)$$

which depends on the phase function $\gamma(\xi)$ that must be determined.

Proceeding from the expression of $\mathbf{F}(\xi)$ as a function of the equivalent electric source current $\mathbf{J}(\mathbf{r}')$ over the volume Σ , it is derived that the critical bandwidth can be expressed as:

$$W = \max_{\xi} \left[\max_{\mathbf{r}'} \left| \frac{\partial \gamma}{\partial \xi} \right| \right] = \max_{\xi} w(\xi) \quad (3.1.7)$$

In order to render the band limitation error small when w exceeds the critical bandwidth W , the parametrization and phase must be selected such that $w(\xi)$ is minimized for any ξ . This is achieved by setting the derivative of the phase to the average of the maximum and minimum of $\beta \partial R / \partial \xi$:

$$\frac{d\gamma(\xi)}{d\xi} = \frac{\beta}{2} \left[\max_{\mathbf{r}'} \frac{\partial R}{\partial \xi} + \min_{\mathbf{r}'} \frac{\partial R}{\partial \xi} \right] \quad (3.1.8)$$

$R = |\mathbf{r} - \mathbf{r}'|$ is the distance between observation point \mathbf{r} and source point \mathbf{r}' . Additionally, ξ is selected to ensure $w(\xi)$ remains constant and equal to W . By choice, the critical bandwidth is set to $W = \beta l' / 2\pi$, where l' represents the length of C' , normalized to the minimum distance between C and C' . Accordingly, ξ is defined as:

$$\xi = \xi(s) = \frac{\beta}{2W} \int_0^s \left[\max_{\mathbf{r}'} \frac{\partial R}{\partial s} - \min_{\mathbf{r}'} \frac{\partial R}{\partial s} \right] ds \quad (3.1.9)$$

Following algebraic manipulation, γ and ξ can be expressed concisely as:

$$\gamma = \beta \left[\frac{R_1 + R_2}{2} + \frac{s'_1 - s'_2}{2} \right] \quad (3.1.10a)$$

$$\xi = \frac{\beta}{W} \left[\frac{R_1 - R_2}{2} + \frac{s'_1 + s'_2}{2} \right] \quad (3.1.10b)$$

where R_1 and R_2 are the distances between observation point $P(s)$ and the tangential

points P_1 and P_2 with the respective arclength coordinates s'_1 and s'_2 , which are illustrated in Figure 3.2

This parametrization ensures that the positions of the non-redundant samples are equispaced in the ξ domain. The selection of W results in ξ covering a 2π range. This implies that at the Nyquist spacing $\Delta\xi = \pi/W$, the number of points lying on any closed meridian curve is finite, constant, and equal to:

$$N_\xi = 2W = \frac{2l'}{\lambda} \quad (3.1.11)$$

3.1.3 Application of Parametrization to Plane-Polar Geometry

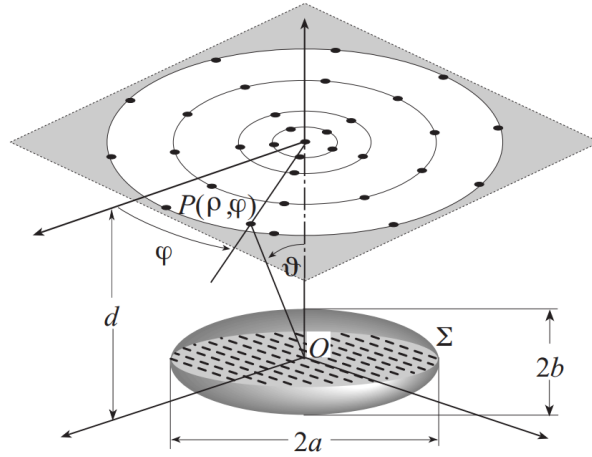


Figure 3.3: Geometry of the antenna under test and the plane-polar surface. Figure reproduced from [27].

This theoretical foundation is applied to sampling on a plane-polar measurement surface in [16]. The plane $z = z_0$ is selected as the surface for near-field measurements, as illustrated in Figure 3.3. Initially, the arrangement of acquisition points along the radial direction to obtain non-redundant measurements is identified. Subsequently, the number of samples required along the azimuthal direction for the radius defined by each of these points to define the field on the specified z -plane is calculated. The meridian plane defined by this radial line is denoted as Π . A cross-section of this meridian plane is depicted in Figure 3.4.

The volume Σ is modeled as a rotational ellipsoid with major and minor axes $2a$ and $2b$, respectively. The foci are located in the xy -plane, each at a distance f from the origin. [16] details how the expressions for $\gamma(\xi)$ and ξ are derived from Equation (3.1.10a) and

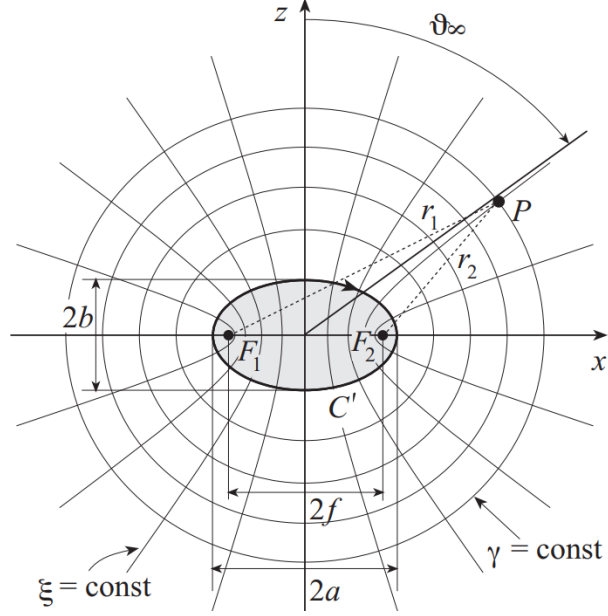


Figure 3.4: Meridian plane geometry. Figure reproduced from [27].

Equation (3.1.10b). They can be written as:

$$\xi = \frac{\pi}{2} \left[\frac{E(\sin^{-1} u | \epsilon^2)}{E(\pi/2 | \epsilon^2)} \right] \quad (3.1.12a)$$

$$\gamma = \beta a \left[v \sqrt{\frac{v^2 - 1}{v^2 - \epsilon^2}} - E \left(\cos^{-1} \sqrt{\frac{1 - \epsilon^2}{v^2 - \epsilon^2}} | \epsilon^2 \right) \right] \quad (3.1.12b)$$

where $E(\cdot)$ is the elliptic integral of second kind, ϵ is the eccentricity of Σ and u, v are elliptic coordinates defined as:

$$u = (r_1 - r_2)/2f \quad (3.1.13a)$$

$$v = (r_1 + r_2)/2a \quad (3.1.13b)$$

Here, r_1 and r_2 describe the distances from point $P(\xi, \varphi)$ to focal points 1 and 2, respectively and $2f$ is the focal distance. In the first step, the critical bandwidth in the radial direction is calculated as:

$$W_\xi = \frac{\beta l'}{2\pi}. \quad (3.1.14)$$

The sample spacing in the ξ -domain is determined by:

$$\Delta\xi = \frac{2\pi}{2N'' + 1} \quad (3.1.15a)$$

$$N'' = \text{Int}(\chi N') + 1 \quad (3.1.15b)$$

$$N' = \text{Int}(\chi' W_\xi) + 1 \quad (3.1.15c)$$

The notation deviates from the previous subsection, as N'' corresponds to the number of non-redundant samples over the meridian plane in the upper half-space ($z > 0$). The parameter χ controls the oversampling, while χ' represents the excess bandwidth factor.

In the subsequent step, the number of samples along φ must be determined at each radius defined by $n\Delta\xi$. The corresponding bandwidth is given by:

$$W_\varphi(\xi) = \beta a \sin v_\infty(\xi), \quad (3.1.16)$$

where $v_\infty = \sin^{-1} u$ is the polar angle of the asymptote to the hyperbola passing through point $P(\xi, \varphi)$. The azimuthal angular spacing $\Delta\varphi$ among points corresponding to the same radius ξ_n is found as:

$$\Delta\varphi_n = \frac{2\pi}{M_n'' + 1} \quad (3.1.17a)$$

$$M_n'' = \text{Int}(\chi M_n') + 1 \quad (3.1.17b)$$

$$M_n' = \text{Int}[\chi^* W_\varphi(\xi_n)] + 1 \quad (3.1.17c)$$

$$\chi^* = 1 + (\chi' - 1) [\sin v_\infty(\xi_n)]^{-2/3} \quad (3.1.17d)$$

3.1.4 Interpolation

The acquisition of non-redundant samples is insufficient in isolation; it is only valuable if a method exists to reconstruct the field associated with the scatterer at unmeasured positions. Therefore, [16] presents an optimal sampling algorithm, using the following Dirichlet and Chebyshev sampling functions:

$$D_L(x) = \frac{\sin\left(\frac{2L+2}{2}x\right)}{(2L+1)\sin\left(\frac{x}{2}\right)} \quad (3.1.18a)$$

$$\Omega_L(x) = \frac{T_L\left[2\left(\frac{\cos(x/2)}{\cos(x_0/2)}\right)^2 - 1\right]}{T_L\left[\frac{2}{\cos^2(x_0/2)} - 1\right]} \quad (3.1.18b)$$

where $T_L(\cdot)$ denotes the Chebyshev polynomial of degree L . Using these functions and the relations $N = N'' - N'$ and $M = M'' - M'$, the formula proposed in [16] to interpolate

the non-redundant sample on an arbitrary point (ξ, φ) is:

$$\begin{aligned} \mathbf{F}(\xi, \varphi) = & \sum_{n=n_0-q+1}^{n_0+q} \Omega_N(\xi - \xi_n) D_{N''}(\xi - \xi_n) \\ & \cdot \sum_{m=m_0-p+1}^{m_0+p} \mathbf{F}(\xi_n, \varphi_{m,n}) \Omega_M(\varphi - \varphi_{m,n}) D_{M''}(\varphi - \varphi_{m,n}) \end{aligned} \quad (3.1.19)$$

x_0 in (3.1.18) is equal to $q\Delta\xi$ or $p\Delta\varphi_n$, where $2q$ and $2p$ represent the number of retained samples along ξ and φ , respectively. n_0 and m_0 correspond to the sampling point (ξ_n, φ_m) that is the closest to the interpolation point (ξ, φ) . Given the reasonable computational complexity in all test cases analyzed in this thesis, all available samples were retained for each interpolation point.

3.1.5 Implementation in the Plane-Polar Case

The practical implementation for calculating the positions of non-redundant samples is not explicitly detailed in the cited literature and is therefore elucidated here. The required parameters include the major and minor axes, a and b , of the rotational ellipsoid that completely encloses the radiating system. Additionally, the wavelength λ and the value z defining the measurement plane must be known.

First, the eccentricity ϵ , the focal distance $2f$, and the length l' of the intersection curve between the meridian plane Π and the ellipsoid are given by:

$$\epsilon = \sqrt{1 - (b/a)^2} \quad (3.1.20a)$$

$$f = \sqrt{a^2 - b^2} \quad (3.1.20b)$$

$$l' = 4aE(\pi/2|\epsilon^2). \quad (3.1.20c)$$

where $E(\cdot|\cdot)$ is the incomplete elliptic integral of the second kind. Subsequently, the critical bandwidth W_ξ is determined according to Equation (3.1.14) (with $\beta = 2\pi/\lambda$), followed by the calculation of N' , N'' , and $\Delta\xi$ according to Equation (3.1.15).

Since $\xi \in [0, \pi]$ on a radial line extending from $x = y = 0$ to infinity, values satisfying the following conditions must be calculated:

$$\xi_n = n\Delta\xi \quad (3.1.21a)$$

$$n \in \mathbb{Z} \quad (3.1.21b)$$

$$n \leq \frac{\pi}{\Delta\xi} \quad (3.1.21c)$$

$\Delta\xi$ is determined according to Equations (3.1.14) and (3.1.15). As $\xi(\mathbf{r})$ is not analytically invertible, $\mathbf{r}(\xi_n)$ must be interpolated from $\xi(\mathbf{r})$. Therefore, ξ is calculated for a sufficient

number of points r along a radial line. For each point, the distances to the focal points are determined:

$$r_1 = \sqrt{(r + f)^2 + z^2} \quad (3.1.22a)$$

$$r_2 = \sqrt{(r - f)^2 + z^2} \quad (3.1.22b)$$

These values are used in conjunction with Equation (3.1.13) to calculate u and v . Then, ξ can be determined for all initially selected values of r via Equation (3.1.12a). From this sequence of corresponding r and ξ values, the non-redundant sampling positions r_n are interpolated for their respective ξ_n .

Subsequently, $r_{1,n}$, $r_{2,n}$, u_n , v_n , and v_n are calculated to obtain both γ_n (Equation (3.1.12b)) and $W_{\varphi,n}$ (Equation (3.1.16)). Similarly to the ξ -case, the angular sample spacing $\Delta\varphi_n$ is determined using Equation (3.1.17a) at each radius r_n , and the sampling positions are calculated as:

$$\varphi_{m,n} = m\Delta\varphi_n \quad (3.1.23a)$$

$$m \in \mathbb{Z} \quad (3.1.23b)$$

$$m \leq \frac{2\pi}{\Delta\varphi_n} \quad (3.1.23c)$$

Having determined all non-redundant sampling positions $(r_n, \varphi_{m,n})$, near-field measurements can be acquired at these coordinates. The reduced field required for interpolation is defined as:

$$\mathbf{F}(\xi_n, \varphi_{m,n}) = \mathbf{E}(\xi_n, \varphi_{m,n}) \exp[j\gamma_n] \quad (3.1.24)$$

This reduced field is then interpolated onto a regular x - y grid, facilitating the calculation of the far field via the plane wave spectrum. In most test cases analyzed in this work, optimal results were obtained by defining the x - y grid such that it extends the non-redundant measurement surface in the x and y directions by a factor of 1.3.

3.1.6 Results

10 dBi Standard-Gain

To validate the non-redundant sampling methodology, it was first tested using full-wave simulation data of a WR34 10-dBi standard-gain horn. This model served as the initial test case for all investigated methods. The near field was simulated at 30 GHz at twice the Fresnel distance from the radiating aperture:

$$z_0 = 0.62\sqrt{D^3/\lambda} \cdot 2 = 28.8 \text{ mm} = 2.898\lambda \quad (3.1.25)$$

where D represents the maximum diameter of the antenna, corresponding to the diagonal of the horn aperture in this instance. The rotational ellipsoid enclosing the antenna is modeled as a circle (eccentricity $\epsilon = 1$) positioned on the horn aperture. Consequently, the semi-minor axis is set to $b = 0$ and the semi-major axis to $a = \sqrt{(a_{ap}/2)^2 + (b_{ap}/2)^2}$, where $a_{ap} = 14.06$ mm and $b_{ap} = 10.5$ mm denote the length and width of the aperture, respectively.

The schematic of the resulting measurement setup is presented in Figure 3.5. The rotational ellipsoid is depicted as the gray region on the aperture.

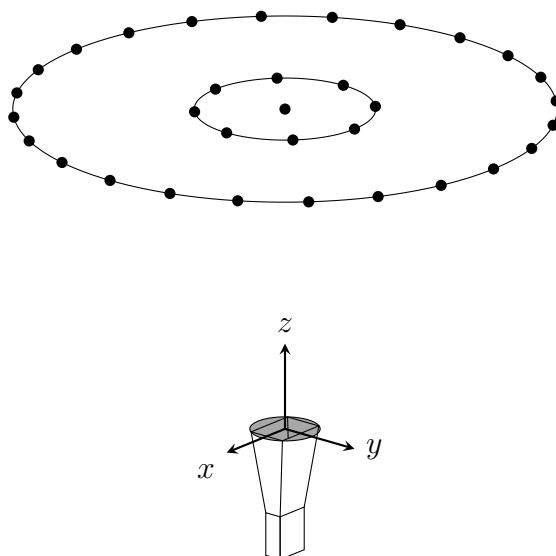


Figure 3.5: 10 dBi horn under test, near-field measurement surface and non-redundant sampling point.

Setting the parameters that control oversampling and excess bandwidth to $\chi = \chi' = 1$ will result in a sampling grid consisting of 22 sampling points on the radii $r/\lambda = [0, 1.17, 3.12]$, that are depicted on Figure 3.6.

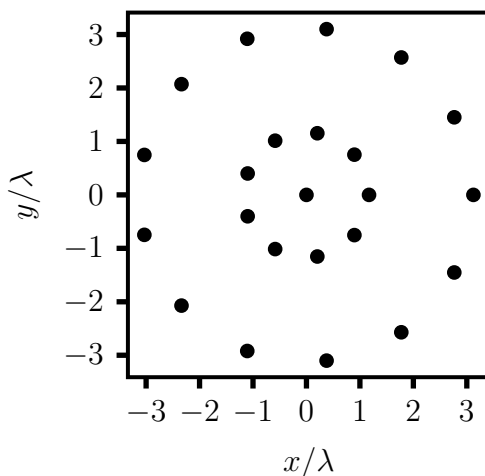


Figure 3.6: 22 non-redundant sampling points on 3 radii ($r/\lambda = [0, 1.17, 3.12]$).

Those 22 samples enable a precise reconstruction of the near field on a domain (approximately $x, y \in [-5.5\lambda, 5.5\lambda]$) that is slightly larger than the measurement area, which is a circle with radius 3.12λ , as depicted in Figure 3.6, using the Equation (3.1.19). The far field reconstructed from this data is precise up to an elevation angle of $\theta \approx 50^\circ$ in this scenario, as illustrated in Figure 3.7. Conversely, if the near field were sampled using conventional methods to achieve precise far-field reconstruction over a comparable elevation range at the same measurement distance z , approximately 529 samples would be required.

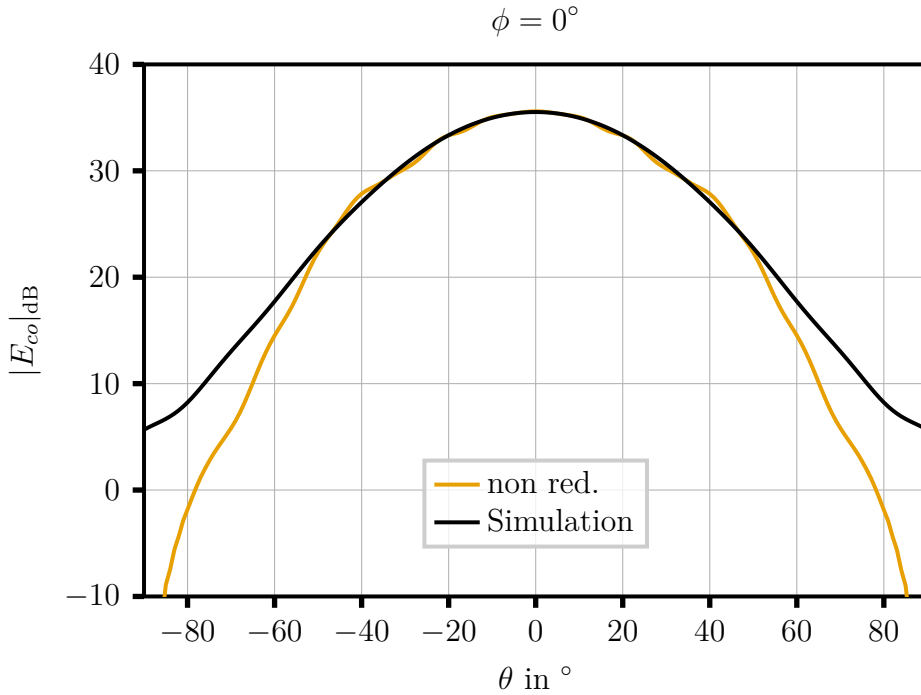


Figure 3.7: Co-polarized far-field pattern (cut in the plane $\phi = 0^\circ$) at 30 GHz of a 10-dBi standard-gain horn reconstructed from 22 non-redundant near-field samples at a distance of $z = 2.89\lambda$, compared to the simulated far-field data.

Flat Lens Antenna

To assess the robustness of the non-redundant sampling approach for more complex radiating structures, a 140 GHz flat lens antenna was examined. As depicted in Figure 3.8, the lens is illuminated by a horn feed from a distance of 15 mm and engineered to rotate the incident y -polarized wave by 90° , while maximizing gain at $\theta = 20^\circ$, $\phi = 0^\circ$ and suppressing side lobes.

There are two possible strategies for defining the antenna enclosing volume that determines the non-redundant measurement grid :

1. Characterize only the dominant x -polarized field component, which corresponds to the co-polarized far field. In this case, the enclosing volume degenerates into a

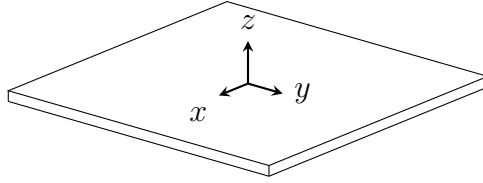


Figure 3.8: Flat lens antenna on the plane $z = 0$ illuminated by a horn feed (drawn to scale).

planar surface containing the lens only. The resulting non-redundant grid is therefore compact, with a relatively small maximum radius and low sampling density.

2. To accurately reconstruct both the co- and cross-polarized far-field patterns, it is necessary to characterize the near-field components in both the x - and y -polarization. The x -polarized near field predominantly originates from the lens, whereas the y -polarized component is primarily radiated by the horn aperture. Consequently, the enclosing volume must encompass the entire radiating structure, including both the flat lens and the horn feed. This results in a substantially larger investigation domain, an increased maximum radius, and, accordingly, a significantly denser and more extensive non-redundant sampling grid.

The resulting non-redundant sampling grids and their efficiency relative to a conventional $\lambda/2$ planar grid are summarized in Table 3.1. The “saved sample” metric quantifies the reduction in measurement points compared to a square grid with side length $2r_{\max}$, where r_{\max} refers to the outermost sampling radius of the non-redundant grid.

	Lens only	Lens + Horn
r_{\max} (mm)	105	680
Number of samples	359	800
Saved samples (%)	96.30	99.80

Table 3.1: Measurement grid parameters for the flat lens antenna.

The second approach, enclosing both the lens and the horn feed in the measurement volume, ensures a physically consistent model for full-polarization reconstruction but comes at the cost of a drastically increased number of required samples. In contrast, the first approach, which encloses only the lens, yields a much sparser non-redundant

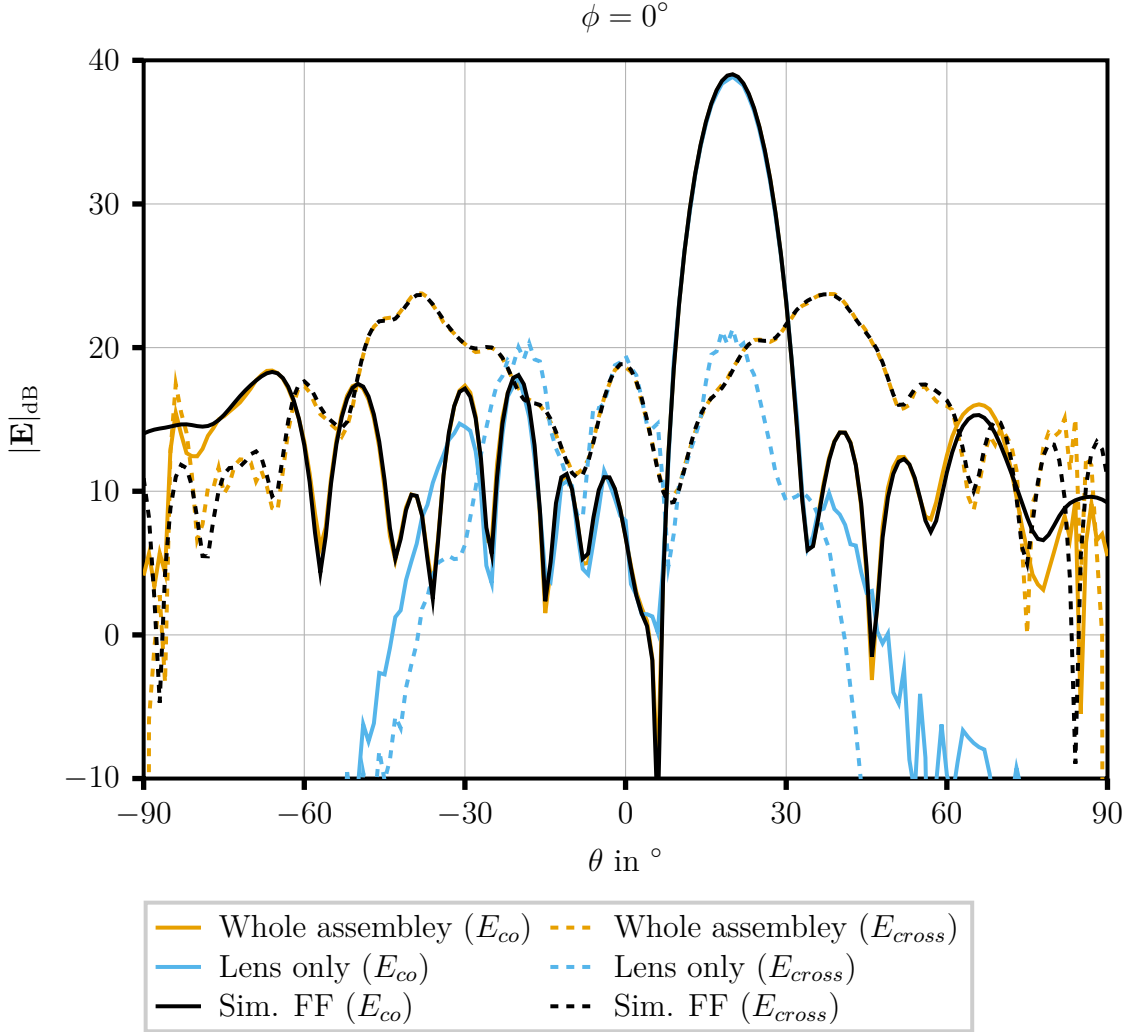


Figure 3.9: Co-polarized and cross-polarized far-field patterns (in the plane $\phi = 0^\circ$). The results of reconstruction from grids considering lens-only vs. lens-plus-horn near-field grids ($z = 0.62\sqrt{D^3/\lambda} = 19.3\lambda = 41.4$ mm, $r_{\max} = 31$ mm), are compared to full-wave simulations.

grid and is therefore far more efficient in terms of measurement effort. However, this efficiency comes with a significant limitation: since the model assumes that all radiated fields originate from the lens volume, it cannot account for the direct contribution of the horn feed. As a result, while the co-polarized far field (predominantly generated by the lens) is expected to be well reconstructed, the accuracy degrades noticeably for $\theta > 35^\circ$, as shown in Figure 3.9. A larger error is observed, in the full angular range, for the reconstructed cross-polarized component, as it significantly depends on the direct radiation from the x -polarized feed.

Interestingly, the lens physically blocks the direct line-of-sight from the horn to the measurement plane for angles up to approximately $\theta \approx 40^\circ$. Within this angular sector, the measurement surface “see” only the field transformed by the lens, and reconstruction is accurate. Beyond this angle, however, the measurement plane captures both the lens-

modified field and the unobstructed near field radiated directly by the horn. Since the first approach’s model excludes the horn as a source, this unmodeled contribution, further complicated by the fact that the horn field is not purely y -polarized, introduces significant errors in both components of the far-field reconstruction.

The same phenomenon was observed for a similar design optimized at 300 GHz to produce a fan beam over $-40^\circ < \theta < 40^\circ$ at $\phi = 0^\circ$, confirming that the issue stems from the mismatch between the assumed source volume and the true field distribution.

These results highlight a critical trade-off: while the non-redundant sampling scheme dramatically reduces the number of required measurements compared to a conventional $\lambda/2$ grid, the accuracy of the far-field reconstruction is highly sensitive to the choice of the antenna-enclosing volume. When the volume is chosen appropriately, capturing all relevant radiating elements, the method achieves high fidelity in the angular regions of interest using only a fraction of the samples. It appears that the extent of this reliable region can be estimated very well using optical analogies such as the angle of validity, described in Section 2.9.3.

3.2 Near Field Warping Sampling Scheme

Maisto and Solimene have developed a warping-based sampling approach in a series of works (inter alia [17], [18]), representing a state-of-the-art contribution to near-field sampling theory. The formulation presented in [18] is particularly suited to planar measurement configurations and is therefore adopted in this work.

The method is conceptually related to the non-redundant sampling approach described in Section 3.1, as it relies on a suitable parametrization of the spatial domain. However, in contrast to modeling the source region as a rotational ellipsoid, the warping-based technique represents the antenna under test (AUT) by equivalent currents distributed over a rectangular planar source domain. This choice makes the approach especially appropriate for aperture-type and horn antennas.

Specifically, the AUT is modeled by equivalent currents defined over the planar source domain

$$SD = [-X_S, X_S] \times [-Y_S, Y_S] \quad \text{at } z = 0 \quad (3.2.1)$$

while the near-field measurements are collected over an observation domain

$$OD = [-X_O, X_O] \times [-Y_O, Y_O] \quad \text{at } z = z_0 \quad (3.2.2)$$

The corresponding measurement configuration is illustrated in Figure 3.10.

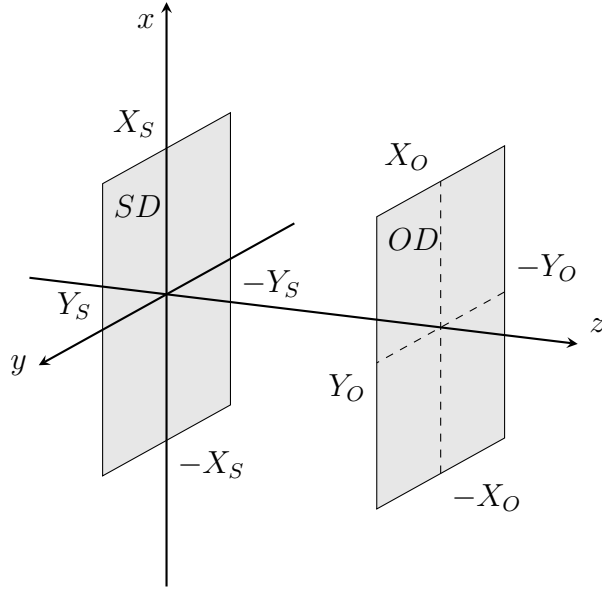


Figure 3.10: Measurement configuration for the coordinate warping scheme.

3.2.1 Approximation of Eigenvalue Problem

The derivation of the optimal sampling scheme begins by expressing the electric field $\mathbf{E}(\mathbf{r}_0)$ over the observation domain OD in terms of the equivalent current distribution \mathbf{J} defined on the source domain SD . This relationship is established through the radiation operator \mathcal{G} , which maps the equivalent currents to the radiated field in the observation region:

$$\mathcal{G} : \mathbf{J} \in L^2(SD^3) \rightarrow \mathbf{E}(\mathbf{r}_0) = \int_{SD} \underline{G}(\mathbf{r}_0, \mathbf{r}) \mathbf{J}(\mathbf{r}) d\mathbf{r} \in L^2(OD^2) \quad (3.2.3)$$

where $\underline{G}(\mathbf{r}_0, \mathbf{r})$ is the free-space dyadic Green's function. The goal is to find a discrete approximation of the eigenvalue problem:

$$(\mathcal{G}\mathcal{G}^\dagger u_n)(\mathbf{r}_0) = \sigma_n^2 \mathbf{u}_n(\mathbf{r}_0) \quad (3.2.4)$$

with \mathcal{G}^\dagger being the adjoint and σ_n^2 the n -th eigenvalue of \mathcal{G} , while \mathbf{u}_n are eigenfunctions of \mathcal{G} that span the observation space. The first step consists in analyzing the kernel function of the composite operator $\mathcal{G}\mathcal{G}^\dagger$, which governs the eigenvalue problem central to determining the degrees of freedom of the radiated field. This kernel, denoted $\underline{K}(\mathbf{r}_0, \mathbf{r}'_0)$, is a 2×2 matrix-valued function obtained through the inner product of Green's functions over the source domain:

$$\underline{K}(\mathbf{r}_0, \mathbf{r}'_0) = \int_{SD} \underline{G}(\mathbf{r}_0, \mathbf{r}) \cdot \underline{G}^H(\mathbf{r}'_0, \mathbf{r}) d\mathbf{r} \quad (3.2.5)$$

where the superscript H denotes conjugate transposition, and only the tangential field components are retained in accordance with near-field measurement conventions. Exploiting the structure of the free-space dyadic Green's function, each entry $K_{n,m}(\mathbf{r}_0, \mathbf{r}'_0)$ of the

kernel matrix can be expressed as:

$$K_{n,m}(\mathbf{r}_0, \mathbf{r}'_0) = \int_{SD} H_{n,m}(\mathbf{r}_0, \mathbf{r}'_0, \mathbf{r}) e^{j[\Phi(\mathbf{r}_0, \mathbf{r}) - \Phi(\mathbf{r}'_0, \mathbf{r})]} d\mathbf{r} \quad (3.2.6)$$

where $\Phi(\mathbf{r}_0, \mathbf{r}) = k\|\mathbf{r}_0 - \mathbf{r}\|$ represents the phase term with $k = 2\pi/\lambda$ being the free-space wavenumber, and $H_{n,m}(\cdot)$ encompasses the amplitude variations. The critical observation underpinning the warping methodology is that the phase difference $\Phi(\mathbf{r}_0, \mathbf{r}) - \Phi(\mathbf{r}'_0, \mathbf{r})$ can be recast through a path integral representation. Specifically, by introducing a polygonal integration path $\mathbf{p}(\nu)$ connecting $\mathbf{r}'_0 = (x'_0, y'_0, z_0)$ to $\mathbf{r}_0 = (x_0, y_0, z_0)$ via the intermediate point (x_0, y'_0, z_0) , we obtain:

$$\Phi(\mathbf{r}_0, \mathbf{r}) - \Phi(\mathbf{r}'_0, \mathbf{r}) = \int_0^1 \nabla_{\mathbf{p}} \Phi(\mathbf{p}(\nu), \mathbf{r}) \cdot \frac{d\mathbf{p}}{d\nu} d\nu = \mathbf{w}(\mathbf{r}_0, \mathbf{r}'_0, \mathbf{r}) \cdot (\mathbf{r}_0 - \mathbf{r}'_0) \quad (3.2.7)$$

where the vector field $\mathbf{w} = (w_x, w_y)$ is defined component-wise as:

$$w_x(x_0, x'_0, \mathbf{r}) = \int_0^1 \frac{\partial \Phi(p_x, y'_0, \mathbf{r})}{\partial p_x} \Bigg|_{p_x=x'_0+\nu(x_0-x'_0)} d\nu, \quad (3.2.8)$$

$$w_y(y_0, y'_0, \mathbf{r}) = \int_0^1 \frac{\partial \Phi(x_0, p_y, \mathbf{r})}{\partial p_y} \Bigg|_{p_y=y'_0+\nu(y_0-y'_0)} d\nu \quad (3.2.9)$$

3.2.2 Parametrization

This reformulation reveals that the phase term resembles a Fourier kernel with spatially varying frequency content determined by \mathbf{w} . Crucially, for fixed observation points \mathbf{r}_0 and \mathbf{r}'_0 , the mapping $\mathbf{r} \mapsto \mathbf{w}(\mathbf{r}_0, \mathbf{r}'_0, \mathbf{r})$ is injective with a full-rank Jacobian matrix over the bounded source domain SD , enabling a valid change of integration variables. Substituting Equation (3.2.7) into Equation (3.2.6) and applying the transformation theorem yields:

$$K_{n,m}(\mathbf{r}_0, \mathbf{r}'_0) = \int_{\Omega(\mathbf{r}_0, \mathbf{r}'_0)} \tilde{H}_{n,m}(\mathbf{r}_0, \mathbf{r}'_0, \mathbf{w}) e^{j\mathbf{w} \cdot (\mathbf{r}_0 - \mathbf{r}'_0)} d\mathbf{w} \quad (3.2.10)$$

where $\Omega(\mathbf{r}_0, \mathbf{r}'_0) = \{\mathbf{w}(\mathbf{r}_0, \mathbf{r}'_0, \mathbf{r}) : \mathbf{r} \in SD\}$ denotes the image of the source domain under the \mathbf{w} -transformation, and $\tilde{H}_{n,m}$ incorporates both the original amplitude term and the Jacobian determinant of the transformation. Equation (3.2.10) demonstrates that the kernel function behaves as a spatially varying band-limited function, with instantaneous bandwidth determined by the geometry-dependent domain $\Omega(\mathbf{r}_0, \mathbf{r}'_0)$.

To render the bandwidth spatially invariant, a rectangular bounding domain $\Omega_R(\mathbf{r}_0, \mathbf{r}'_0)$ is introduced that minimally encloses $\Omega(\mathbf{r}_0, \mathbf{r}'_0)$. Denoting the center of mass of Ω_R as $\mathbf{w}_m(\mathbf{r}_0, \mathbf{r}'_0)$ and its half-extents along coordinate axes as $\Delta w_x(\mathbf{r}_0, \mathbf{r}'_0)$ and $\Delta w_y(\mathbf{r}_0, \mathbf{r}'_0)$, we

decompose $\mathbf{w} = \mathbf{w}_m + \bar{\mathbf{w}}$ and rewrite Equation (3.2.10) as:

$$K_{n,m}(\mathbf{r}_0, \mathbf{r}'_0) \approx e^{j\mathbf{w}_m \cdot (\mathbf{r}_0 - \mathbf{r}'_0)} \int_{-\Delta w_x}^{\Delta w_x} \int_{-\Delta w_y}^{\Delta w_y} \tilde{H}_{n,m}(\mathbf{r}_0, \mathbf{r}'_0, \bar{\mathbf{w}}) e^{j\bar{\mathbf{w}} \cdot (\mathbf{r}_0 - \mathbf{r}'_0)} d\bar{\mathbf{w}} \quad (3.2.11)$$

The approximation becomes exact when $\Omega(\mathbf{r}_0, \mathbf{r}'_0)$ itself is rectangular, which occurs under the geometric constraint $OD \subseteq SD$ (i.e., when the measurement aperture does not exceed the source extent). Under this condition, a profound simplification emerges: the bandwidth extents Δw_x and Δw_y become separable functions depending solely on the corresponding Cartesian observation coordinates:

$$\Delta w_x(x_0, x'_0) = \frac{k}{2(x_0 - x'_0)} \left[\sqrt{(x_0 + X_s)^2 + z_0^2} - \sqrt{(x_0 - X_s)^2 + z_0^2} - \sqrt{(x'_0 + X_s)^2 + z_0^2} + \sqrt{(x'_0 - X_s)^2 + z_0^2} \right] \quad (3.2.12)$$

$$\Delta w_y(y_0, y'_0) = \frac{k}{2(y_0 - y'_0)} \left[\sqrt{(y_0 + Y_s)^2 + z_0^2} - \sqrt{(y_0 - Y_s)^2 + z_0^2} - \sqrt{(y'_0 + Y_s)^2 + z_0^2} + \sqrt{(y'_0 - Y_s)^2 + z_0^2} \right] \quad (3.2.13)$$

This separability motivates the introduction of the warping transformations $\boldsymbol{\xi} : OD \rightarrow \mathbb{R}^2$ and $\boldsymbol{\gamma} : OD \rightarrow \mathbb{R}^2$, defined component-wise as:

$$\xi_x(x_0) = \frac{k}{2} \left[\sqrt{(x_0 + X_s)^2 + z_0^2} - \sqrt{(x_0 - X_s)^2 + z_0^2} \right] \quad (3.2.14)$$

$$\xi_y(y_0) = \frac{k}{2} \left[\sqrt{(y_0 + Y_s)^2 + z_0^2} - \sqrt{(y_0 - Y_s)^2 + z_0^2} \right] \quad (3.2.15)$$

$$\gamma_x(x_0) = \frac{k}{2} \left[\sqrt{(x_0 + X_s)^2 + z_0^2} + \sqrt{(x_0 - X_s)^2 + z_0^2} \right] \quad (3.2.16)$$

$$\gamma_y(y_0) = \frac{k}{2} \left[\sqrt{(y_0 + Y_s)^2 + z_0^2} + \sqrt{(y_0 - Y_s)^2 + z_0^2} \right] \quad (3.2.17)$$

After introducing the warping transformations $\boldsymbol{\xi}$ and $\boldsymbol{\gamma}$, the methodology proceeds to establish a sampling framework in the warped coordinate system where the kernel function exhibits approximately uniform bandwidth. Critically, the bandwidth extents simplify to differences of the ξ -coordinates:

$$\Delta w_x(x_0, x'_0) = \xi_x(x_0) - \xi_x(x'_0) \quad (3.2.18)$$

$$\Delta w_y(y_0, y'_0) = \xi_y(y_0) - \xi_y(y'_0) \quad (3.2.19)$$

which follows directly from the definitions in Equations (3.2.14) and (3.2.15) without additional scaling factors. This property confirms that the kernel in Equation (3.2.11) becomes a band-limited function with constant bandwidth $[-1, 1] \times [-1, 1]$ in the normalized warped coordinates $\hat{\xi}_x = \xi_x/\pi$, $\hat{\xi}_y = \xi_y/\pi$.

3.2.3 Interpolation

Consequently, the Shannon sampling theorem applies directly in the warped domain, yielding the interpolation formula for the tangential field components:

$$E_n(x_0, y_0) = e^{j[\gamma_x(x_0) + \gamma_y(y_0)]} \sum_{m=-M}^M \sum_{l=-L}^L E_n(x_{0,m}, y_{0,l}) e^{-j[\gamma_x(x_{0,m}) + \gamma_y(y_{0,l})]} \cdot \text{sinc}\left(\frac{\xi_x(x_0) - \xi_x(x_{0,m})}{\pi}\right) \text{sinc}\left(\frac{\xi_y(y_0) - \xi_y(y_{0,l})}{\pi}\right) \quad (3.2.20)$$

where the sampling points $\{(x_{0,m}, y_{0,l})\}$ are determined by inverting the warping transformation at uniformly spaced nodes in the ξ -domain:

$$\xi_x(x_{0,m}) = m\pi, \quad \xi_y(y_{0,l}) = l\pi, \quad m = -M, \dots, M, \quad l = -L, \dots, L \quad (3.2.21)$$

The integers M and L are selected such that the sampling grid spans the entire observation domain $OD = [-X_0, X_0] \times [-Y_0, Y_0]$, i.e., $M = \lceil \xi_x(X_0)/\pi \rceil$ and $L = \lceil \xi_y(Y_0)/\pi \rceil$. The phase compensation terms involving γ_x and γ_y in Equation (3.2.20) are essential to account for the non-stationary spectral content of the kernel; they effectively demodulate the rapidly varying carrier before interpolation and remodulate the reconstructed field, ensuring accurate representation of both amplitude and phase characteristics.

3.2.4 Spatial Varying Oversampling

This interpolation scheme achieves exact reconstruction for band-limited fields when $OD \subseteq SD$ (measurement aperture contained within the source projection). However, in practical near-field measurement scenarios, the observation domain typically exceeds the source extent ($OD \supset SD$) to mitigate truncation errors in subsequent far field transformations. Under this condition, the rectangular approximation of $\Omega(\mathbf{r}_0, \mathbf{r}'_0)$ becomes increasingly inaccurate toward the aperture edges. The factorized warping transformations Equations (3.2.14) and (3.2.15) consequently underestimate the required sampling density in peripheral regions.

To address this limitation [18] introduces a spatially varying oversampling factor $\alpha(\mathbf{r}_0) = \alpha_x(x_0)\alpha_y(y_0)$ that adaptively increases sampling density where needed. The modified warping transformation becomes:

$$\alpha_x(x_0) = 1 - (\nu - 1) \sin^p\left(\frac{\pi|x_0|}{2X_0}\right) \quad \alpha_y(y_0) = 1 - (\nu - 1) \sin^p\left(\frac{\pi|y_0|}{2Y_0}\right) \quad (3.2.22)$$

$$\tilde{\xi}_x = a_x(x_0)\xi_x \quad \tilde{\xi}_y = a_y(y_0)\xi_y \quad (3.2.23)$$

with parameters $\nu > 1$ controlling the maximum oversampling ratio (typically $\nu = 1.2$ – 1.5) and $p \geq 2$ governing the transition sharpness (commonly $p = 4$ for smooth behavior).

The interpolation formula adapts to this modified grid by replacing ξ_x, ξ_y with $\tilde{\xi}_x, \tilde{\xi}_y$ in Equation (3.2.20), while retaining the same phase compensation terms γ_x, γ_y which depend solely on geometry rather than sampling strategy.

3.2.5 Results

When applying this Warping algorithm to the same setup as used before and described in Section 3.1.6, with $X_S = 4\lambda$, $Y_S = 3.5\lambda$, $z_0 = 2.898\lambda$ and using a reasonable spatial oversampling factor of $\nu = 1.3$ and $p = 4$, the resulting sampling grid consists of 25 points and is depicted in Figure 3.11.

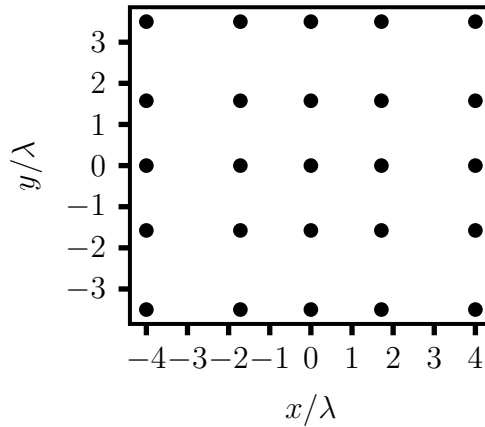


Figure 3.11: Warped sampling grid consisting of 25 points.

Those 25 samples enable a precise reconstruction of the near field on a domain that is slightly larger than the measurement area (approximately $x, y \in [-5.5\lambda, 5.5\lambda]$) using the Equation (3.2.20). The far field constructed from this data is precise up to an elevation angle of $\theta \approx 50^\circ$ in this scenario, as illustrated in Figure 3.12. Conversely, if the near field were sampled using conventional methods to achieve precise far field reconstruction over a comparable elevation range at the same measurement distance z , approximately 529 samples would be required.

3.2.6 Alternative Oversampling of the Warped Grid

[18] introduces spatially varying oversampling, as defined in Equation (3.2.22), to compensate for sparse sampling in regions of the observation domain $\not\subseteq SD$, since the derived warping parametrization is only accurate when $OD \subseteq SD$. However, this oversampling approach does not alter the sampling density at the center of the observation domain ($x = y = 0$). For large values of p , the sampling density remains unchanged within the

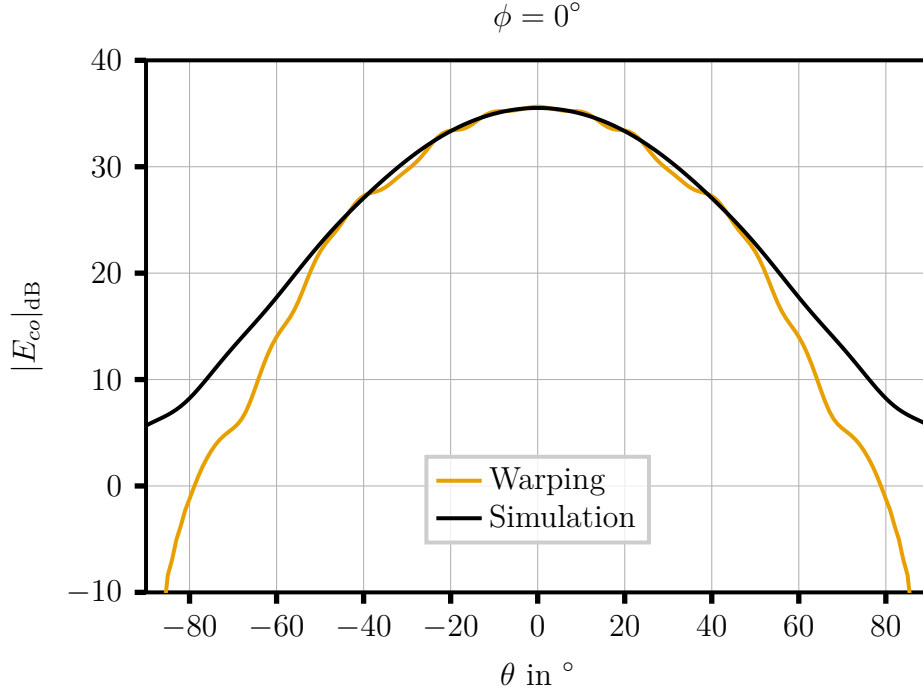


Figure 3.12: Co-polarized far field pattern (cut in the plane $\phi = 0^\circ$) at 30 GHz of a 10-dBi standard-gain horn reconstructed from a warped sampling grid consisting of 25 points at a distance of $z = 2.89\lambda$, compared to the simulated far field.

region $|x| < X_O/2$, $|y| < Y_O/2$ and then transitions rapidly to an oversampling factor of ν relative to the initial warped grid.

To enable oversampling across the entire observation domain, the oversampling formula in Equation (3.2.22) was modified to:

$$\alpha_x(x_0) = \nu_1 - (\nu_2 - \nu_1) \sin^p\left(\frac{\pi|x_0|}{2X_0}\right) \quad \alpha_y(y_0) = \nu_1 - (\nu_2 - \nu_1) \sin^p\left(\frac{\pi|y_0|}{2Y_0}\right) \quad (3.2.24)$$

This formulation ensures that the oversampling factor transitions from ν_1 to ν_2 with increasing distance from the origin $x = y = 0$, rather than transitioning from 1 to ν . This modification facilitates the evaluation of reconstruction fidelity across a broad range of overall sampling densities, thereby enabling a rigorous comparison with alternative approaches.

3.3 Sparse Nonuniform Planar Sampling Based on Angular Projection

Given the theoretical complexity of the two preceding methods, a simpler alternative was evaluated: the sparse planar sampling scheme proposed in [22].

3.3.1 Methodology

This method projects a spherical sampling grid onto a planar surface. The spherical grid satisfies Nyquist criteria with angular spacing

$$\Delta\theta \leq \frac{2\pi}{2N+1} \quad (3.3.1a)$$

$$\Delta\phi = \frac{\Delta\theta}{\sin\theta} \quad (3.3.1b)$$

where $N = \lfloor kr_0 \rfloor + 10$, k is the wavenumber, and r_0 is the radius of the smallest sphere enclosing the antenna. In practice the elevation angle step was defined via an oversampling factor $\nu \geq 1$

$$\Delta\theta = \frac{2\pi}{\nu(2N+1)} \quad (3.3.2)$$

The planar observation domain $OD = [-X_S, X_S] \times [-Y_S, Y_S]$ at $z = z_0$ is aligned such that its x' -axis coincides with the spherical $\phi = 0$ direction, and its y' -axis corresponds to the spherical polar axis. Thus, the planar origin $(x', y') = (0, 0)$ maps to $(\theta, \phi) = (\pi/2, \pi/2)$. The domain extents correspond to angular limits $(\pm\alpha_\phi, \pm\alpha_\theta)$, and sampled angles are restricted to

$$\phi \in [-\alpha_\phi, \alpha_\phi] \quad (3.3.3a)$$

$$\theta \in \left[\frac{\pi}{2} - \alpha_\theta, \frac{\pi}{2} + \alpha_\theta \right] \quad (3.3.3b)$$

$$\alpha_\phi = \tan^{-1}(X_S/z_0) \quad (3.3.3c)$$

$$\alpha_\theta = \tan^{-1}(Y_S/z_0) \quad (3.3.3d)$$

Sample positions on the plane are then computed as

$$x' = z_0 \tan(\pi/2 - \phi) \quad (3.3.4a)$$

$$y' = z_0 \tan(\pi/2 - \theta) \quad (3.3.4b)$$

The described projection is visualized in Figure 3.13

Unlike previous methods, interpolation is performed via bilinear interpolation on a phase-

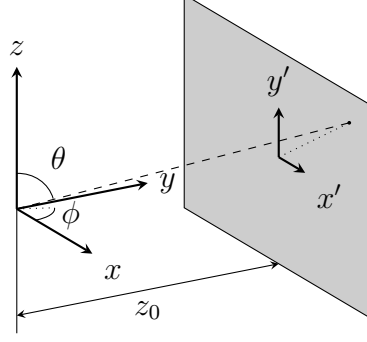


Figure 3.13: Projection of spherical coordinates onto the measurement plane.

reduced field $\mathbf{F}(\mathbf{r}) = \mathbf{E}(\mathbf{r})e^{jk|\mathbf{r}|}$:

$$\mathbf{F}(x, y) = \sum_{s=m}^{m+1} \sum_{t=n}^{n+1} w_{s,t}(x, y) \mathbf{F}(x_s, y_t) \quad (3.3.5a)$$

$$w_{m,n}(x, y) = \frac{(x_{m+1} - x)(y_{n+1} - y)}{(x_{m+1} - x_m)(y_{n+1} - y_n)} \quad (3.3.5b)$$

$$w_{m+1,n}(x, y) = \frac{(x - x_m)(y_{n+1} - y)}{(x_{m+1} - x_m)(y_{n+1} - y_n)} \quad (3.3.5c)$$

$$w_{m,n+1}(x, y) = \frac{(x_{m+1} - x)(y - y_n)}{(x_{m+1} - x_m)(y_{n+1} - y_n)} \quad (3.3.5d)$$

$$w_{m+1,n+1}(x, y) = \frac{(x - x_m)(y - y_n)}{(x_{m+1} - x_m)(y_{n+1} - y_n)} \quad (3.3.5e)$$

where m and n are defined by

$$m = \max\{i \mid x_i \leq x\}, \quad n = \max\{j \mid y_j \leq y\}. \quad (3.3.6)$$

3.3.2 Results

The simulation setup is identical to the previous case and is summarized as follows:

- 30 GHz standard-gain horn antenna with 10 dBi gain,
- $X_S = 4\lambda$, $Y_S = 3.5\lambda$
- $z_0 = 2.898\lambda$

The oversampling factor was set to $\nu = 1$, resulting in a sampling grid consisting of 76 points, as shown in Figure 3.14.

The far field reconstructed from these 76 sampling points by interpolation onto a $\lambda/4$ grid using Equation (3.3.5) is shown in Figure 3.15. In both the main lobe region ($\theta \approx 0$) and at angles close to the limit of validity, the far field obtained using the Igloo approach exhibits inferior agreement with the reference solution compared to both the

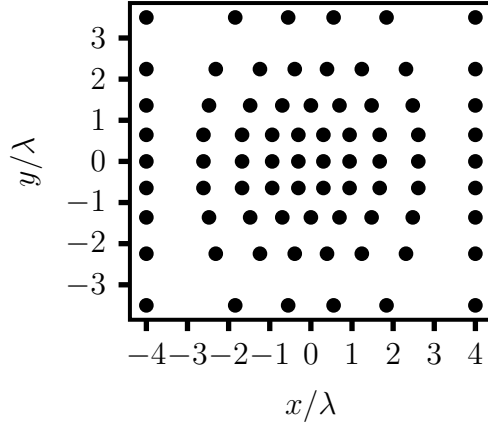


Figure 3.14: Igloo sampling grid consisting of 76 points.

non-redundant sampling approach and the warping approach. This degradation occurs despite the significantly larger number of sampling points employed.

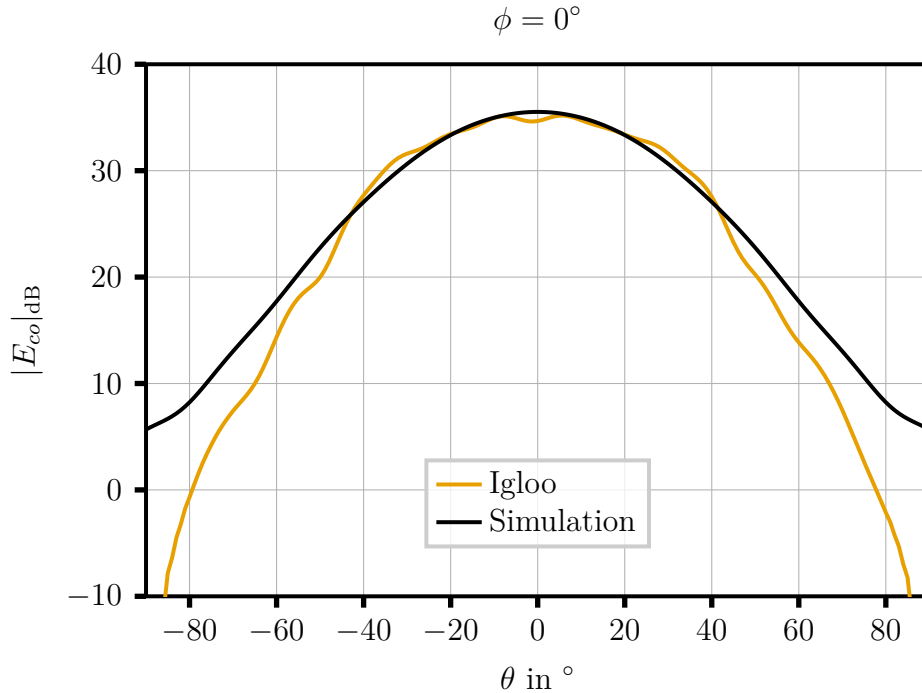


Figure 3.15: Co-polarized far-field pattern (cut in the plane $\phi = 0^\circ$) at 30 GHz of a 10-dBi standard-gain horn reconstructed from an Igloo sampling grid consisting of 76 points at a distance of $z_0 = 2.898\lambda$, compared with the simulated far field.

3.4 Interpolation of Near Fields without Prior Source Knowledge

All previously discussed methods rely on knowledge of the source geometry to determine sampling locations and interpolation strategies. To assess the performance of a method

requiring no prior information beyond frequency, the approach in [25] was examined.

3.4.1 Methodology

This method selects $p < mn$ sampling points randomly from a fixed uniform lattice Σ of size $m \times n$. The measured field values $\mathbf{e} \in \mathbb{C}^p$ are then interpolated onto all lattice points. The unknown full field matrix is denoted $\mathbf{X} \in \mathbb{C}^{m \times n}$.

Interpolation combines two criteria: minimization of the rank of \mathbf{X} (interpreted as seeking the field of the lowest complexity) and minimization of the ℓ_2 -norm between \mathbf{X} and a thin plate spline (TPS) interpolation estimate.

Rank Minimization

Finding the simplest field consistent with measurements \mathbf{e} is formulated as:

$$\min_{\mathbf{X} \in \mathbb{C}^{m \times n}} \text{rank}(\mathbf{X}) \quad \text{s.t.} \quad \|\mathcal{A}(\mathbf{X}) - \mathbf{e}\|_2 \leq \epsilon, \quad (3.4.1)$$

where $\mathcal{A} : \mathbb{C}^{m \times n} \rightarrow \mathbb{C}^p$ extracts the measured entries, and ϵ accounts for measurement noise. This matrix completion problem is non-convex; thus, the nuclear norm is minimized instead:

$$\min_{\mathbf{X} \in \mathbb{C}^{m \times n}} \|\mathbf{X}\|_* \quad \text{s.t.} \quad \|\mathcal{A}(\mathbf{X}) - \mathbf{e}\|_2 \leq \epsilon, \quad (3.4.2)$$

with nuclear norm

$$\|\mathbf{X}\|_* = \sum_{k=1}^r \sigma_k(\mathbf{X}), \quad (3.4.3)$$

where $\sigma_k(\mathbf{X})$ are the singular values of \mathbf{X} . Nuclear norm minimization serves as a convex surrogate for rank minimization [28]. Problem Equation (3.4.2) is recast as:

$$\begin{aligned} & \min_{\mathbf{X}, \mathbf{Y}, \mathbf{Z}} \text{Tr}(\mathbf{Y}) + \text{Tr}(\mathbf{Z}) \\ & \text{s.t.} \quad \begin{cases} \|\mathcal{A}(\mathbf{X}) - \mathbf{e}\|_2 \leq \epsilon \\ \begin{bmatrix} \mathbf{Y} & \mathbf{X} \\ \mathbf{X}^* & \mathbf{Z} \end{bmatrix} \succeq 0 \end{cases} \\ & \mathbf{Y} = \mathbf{Y}^H \in \mathbb{C}^{m \times m}, \quad \mathbf{Z} = \mathbf{Z}^H \in \mathbb{C}^{n \times n}. \end{aligned} \quad (3.4.4)$$

Thin Plate Spline Interpolation

The TPS interpolation estimates unmeasured field values $\tilde{\mathbf{e}}$ by promoting smoothness, expressed as a superposition of radial basis functions:

$$\begin{aligned}\tilde{\mathbf{e}}(\mathbf{r}) &= \sum_{i=1}^p c_i \Phi(|\mathbf{r} - \mathbf{r}_i|), \\ \Phi(r) &= -r^2 \log(r^2).\end{aligned}\tag{3.4.5}$$

Coefficients c_i are obtained by solving

$$e_k = \sum_{i=1}^p c_i \Phi(|\mathbf{r}_k - \mathbf{r}_i|), \quad k = 1, \dots, p,\tag{3.4.6}$$

where e_k are the measured field values at positions \mathbf{r}_k .

Combined Interpolation Scheme

The two approaches are combined by augmenting the nuclear norm minimization with a fidelity term to the TPS estimate:

$$\min_{\mathbf{X} \in \mathbb{C}^{m \times n}} \|\mathbf{X}\|_* + \alpha \|\mathbf{W}(\mathcal{A}^c(\mathbf{X}) - \tilde{\mathbf{e}})\|_2 \quad \text{s.t.} \quad \|\mathcal{A}(\mathbf{X}) - \mathbf{e}\|_2 \leq \epsilon,\tag{3.4.7}$$

where $\mathcal{A}^c : \mathbb{C}^{m \times n} \rightarrow \mathbb{C}^{mn-p}$ selects unmeasured entries. Following [25], the weights that balance the two terms in Equation (3.4.7) are defined as $W_{i,i} = |\tilde{e}_i|^{-1}$, based on the assumption that TPS estimates with larger amplitudes are more reliable.

The problem was implemented in CVXPY using MOSEK, with each electric field component treated independently. CVXPY is a high-level modeling language for formulating convex optimization problems, whereas MOSEK is a numerical optimization solver that integrates with CVXPY to efficiently solve the resulting problem instances.

3.4.2 Pseudo Random Sampling Point Selection

The method proposed by [25], which reconstructs the near field via rank minimization and thin plate spline interpolation, selects sampling points from a prescribed uniform lattice as detailed in Section 3.4. This strategy is generally effective when at least approximately 33% of the lattice points are selected. However, when significantly fewer points are chosen at random, the resulting distribution often exhibits clustering and large unsampled regions. Near-field reconstruction accuracy degrades notably in these sparsely sampled areas. To mitigate this issue, the purely random selection process was replaced with a simple pseudo-random algorithm.

Initially, a random permutation of lattice points is generated. Points are then sequentially added to the sampling set only if they are not adjacent, neither orthogonally nor diagonally, to any point already included. If the target number of samples cannot be achieved under this constraint, the procedure is repeated with a relaxed criterion that permits diagonal adjacency. Should the required sample count still not be attainable, the remaining points are selected uniformly at random. This straightforward algorithm promotes a more uniform spatial distribution of sampling points, thereby improving near-field reconstruction performance under substantial undersampling conditions relative to the original lattice.

3.4.3 Results

The simulation setup is identical to the previous case and is summarized as follows:

- 30 GHz standard-gain horn antenna with 10 dBi gain,
- $X_S = 4\lambda$, $Y_S = 3.5\lambda$
- $z_0 = 2.898\lambda$

To obtain a far-field reconstruction quality matching the previous approaches, half of the $\lambda/2$ grid points, which was chosen as the uniform lattice Σ , were chosen as sampling points. The grid can be seen in Figure 3.16.

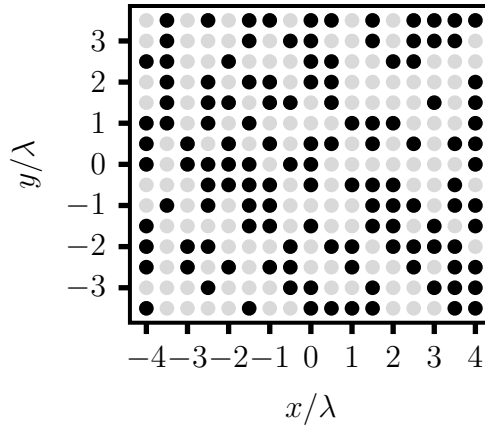


Figure 3.16: 127 random selected points from a $\lambda/2$ grid.

The far-field reconstructed from these 127 sampling points interpolated by the presented hybrid scheme, using $\alpha = 50$, is shown in Figure 3.17.

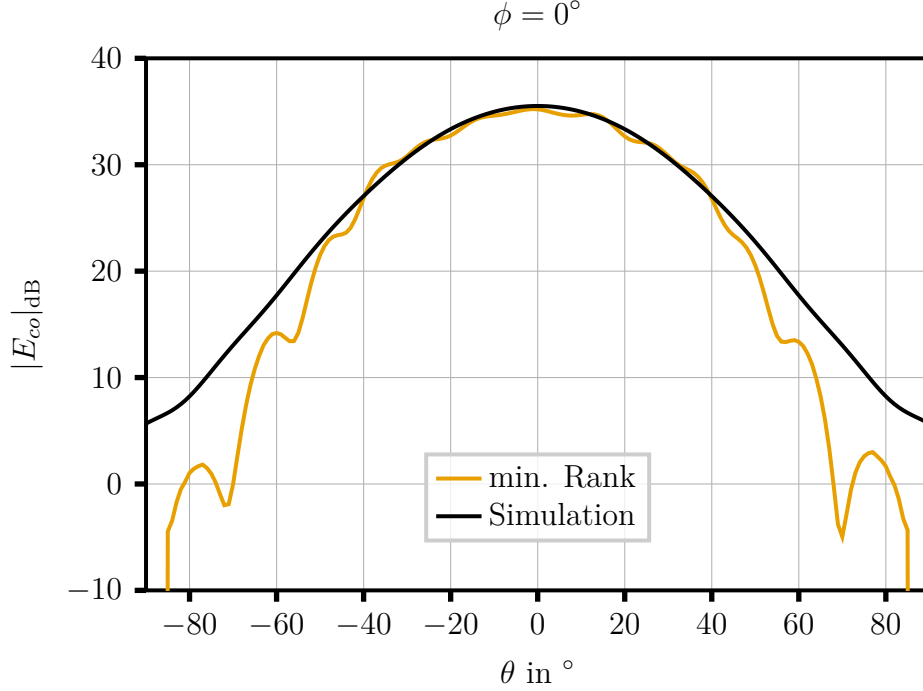


Figure 3.17: Co-polarized far-field pattern (cut in the plane $\phi = 0^\circ$) at 30 GHz of a 10-dBi standard-gain horn reconstructed from a random grid consisting of 127 points at a distance of $z_0 = 2.898\lambda$, compared with the simulated far field.

3.5 Greedy Sampling Point Selection for Planar Near-Field Measurements

The final method, introduced in [19], adopts a distinct strategy: it first selects an optimal subset of measurement points from a given grid, then reconstructs the harmonics of equivalent source currents from the acquired data. The same geometry as in Figure 3.10 is assumed, with vanishing fields outside the source domain SD at $z = 0$.

3.5.1 Radiation Operator Derivation

Optimal point selection requires relating candidate observation points to source current harmonics. The continuous radiation operator maps equivalent magnetic source currents to the electric field:

$$\mathcal{G} : \mathbf{J}_{ms} \in L^2[SD] \rightarrow \mathbf{E}(\mathbf{r}_o) = \int_{SD} \mathbf{G}(\mathbf{r}_o, \mathbf{r}) \cdot \mathbf{J}_{ms}(\mathbf{r}) d\mathbf{r} \in L^2[OD], \quad (3.5.1)$$

with dyadic Green function

$$\mathbf{G}(\mathbf{r}_o, \mathbf{r}) = \begin{bmatrix} 0 & -\frac{\partial g}{\partial z_o}(\mathbf{r}_o, \mathbf{r}) \\ \frac{\partial g}{\partial z_o}(\mathbf{r}_o, \mathbf{r}) & 0 \end{bmatrix}, \quad g(\mathbf{r}_o, \mathbf{r}) = -\frac{e^{-jk|\mathbf{r}_o - \mathbf{r}|}}{4\pi|\mathbf{r}_o - \mathbf{r}|}. \quad (3.5.2)$$

Rather than expanding \mathbf{J}_{ms} directly in Fourier harmonics as in [19], we express it via the electric field \mathbf{E}_s on the source plane:

$$\mathbf{J}_{ms}(x, y) = 2\mathbf{E}_s(x, y) \times \hat{z} = 2 \sum_{m,n} \tilde{\mathbf{E}}(m, n) \times \hat{z} \cdot e^{-jk\pi\left(\frac{mx}{N_x} + \frac{ny}{N_y}\right)}, \quad (3.5.3)$$

where harmonic indices satisfy $m \in [-N_x, N_x]$, $n \in [-N_y, N_y]$, with

$$N_x = \left\lceil \frac{2X_S}{\lambda} \right\rceil, \quad N_y = \left\lceil \frac{2Y_S}{\lambda} \right\rceil. \quad (3.5.4)$$

Substituting into Equation (3.5.1) and assuming negligible z -component of \mathbf{E}_s yields

$$\mathbf{E}(\mathbf{r}_o) = 2 \sum_{m,n} \tilde{\mathbf{E}}_{m,n} \underbrace{\int_{SD} \frac{\partial g}{\partial z_o}(\mathbf{r}_o, \mathbf{r}) e^{-jk\pi\left(\frac{mx}{N_x} + \frac{ny}{N_y}\right)} d\mathbf{r}}_{G_{m,n}(\mathbf{r}_o)}. \quad (3.5.5)$$

The kernel $G_{m,n}(\mathbf{r}_o)$ is evaluated by discretizing SD with $\lambda/2$ spacing:

$$x_p = p\lambda/2, \quad p \in [-N_x, N_x], \quad y_q = q\lambda/2, \quad q \in [-N_y, N_y]. \quad (3.5.6)$$

The derivative of the Green function is

$$\frac{\partial g}{\partial z_o}(\mathbf{r}_o, \mathbf{r}) = \frac{z_0}{4\pi} \left(\frac{jk}{|\mathbf{r}_o - \mathbf{r}|^2} + \frac{1}{|\mathbf{r}_o - \mathbf{r}|^3} \right) e^{-jk|\mathbf{r}_o - \mathbf{r}|}, \quad (3.5.7)$$

leading to the discrete approximation

$$G_{m,n}(\mathbf{r}_o) = \sum_{p,q} \frac{z_0}{4\pi} \left(\frac{jk}{|\mathbf{r}_o - \mathbf{r}_{p,q}|^2} + \frac{1}{|\mathbf{r}_o - \mathbf{r}_{p,q}|^3} \right) e^{-jk|\mathbf{r}_o - \mathbf{r}_{p,q}|} e^{-jk\pi\left(\frac{mx_p}{N_x} + \frac{ny_q}{N_y}\right)} \left(\frac{\lambda}{2}\right)^2. \quad (3.5.8)$$

3.5.2 Optimal Sampling Point Selection

To select H_S points from H candidates, the system is cast as

$$\mathbf{E}_i = \mathbf{G}_t \cdot \tilde{\mathbf{E}}_i, \quad (3.5.9)$$

where $i \in \{x, y\}$ denotes field components (treated independently). $\mathbf{E}_i \in \mathbb{C}^H$ contains near-field values at H candidate points ($z = z_0$), and $\tilde{\mathbf{E}}_i \in \mathbb{C}^L$ holds Fourier harmonics of the field on SD satisfying

$$k_{xm}^2 + k_{yn}^2 = \left(\frac{m\pi}{X_S}\right)^2 + \left(\frac{n\pi}{Y_S}\right)^2 \leq k^2. \quad (3.5.10)$$

The task reduces to selecting H_S rows of $\mathbf{G}_t \in \mathbb{C}^{H \times L}$. Following [19], a greedy algorithm is used that minimizes the noise factor (NF):

$$NF = \sum_{l=1}^L \frac{1}{\lambda_l(\mathbf{A})}, \quad \mathbf{A} = \mathbf{G}_t^{H_S \dagger} \mathbf{G}_t^{H_S}. \quad (3.5.11)$$

Selection occurs in two phases. First, L linearly independent rows are chosen: at iteration i , the row \mathbf{g}_t^i maximizing projection onto the nullspace of \mathbf{A}_{i-1} is selected:

$$\mathbf{R}_{i-1} = \text{orth} \left\{ \mathbf{G}_t^{i-1T} \right\}, \quad (3.5.12a)$$

$$\mathbf{P}_{i-1} = \mathbf{I} - \mathbf{R}_{i-1} \mathbf{R}_{i-1}^\dagger, \quad (3.5.12b)$$

$$\mathbf{g}_t^i = \arg \max_{h \in H \setminus \mathcal{S}} \frac{\|\mathbf{P}_{i-1} \mathbf{g}_t^h\|_2^2}{\|\mathbf{g}_t^h\|_2^2}. \quad (3.5.12c)$$

After L steps, the second phase adds points minimizing NF:

$$\mathbf{g}_t^i = \arg \min_{h \in H \setminus \mathcal{S}} \sum_{l=1}^L \frac{1}{\lambda_l(\mathbf{A}_i^h)}, \quad (3.5.13a)$$

$$\mathbf{A}_i^h = \mathbf{A}_{i-1} + \mathbf{g}_t^{h\dagger} \mathbf{g}_t^h. \quad (3.5.13b)$$

This continues until H_S points are selected.

3.5.3 Alternative Selection of Optimal Sampling Points

The greedy approach for optimal sampling point selection, as described in Section 3.5.2 and [19], is computationally efficient; however, greedy algorithms generally do not yield globally optimal solutions. The sampling points obtained by this greedy algorithm for the scenario with $X_S = 1.36\lambda$, $Y_S = 1\lambda$, $X_O = Y_O = 11.5\lambda$, and $z_0 = 7\lambda$ are illustrated in Figure 3.18. Since the optimization problem addressed by this greedy algorithm resembles the well-known sensor selection problem, alternative solution strategies with potentially superior performance were investigated. Two approaches were adopted from [29]. Both assume the following linear relationship between the harmonics of the electric field in the source domain $\tilde{\mathbf{E}}_i$ and the electric near field in the observation domain \mathbf{E}_i , corrupted by additive white Gaussian noise \mathbf{v}_i :

$$\mathbf{E}_i = \mathbf{G}^T \cdot \tilde{\mathbf{E}}_i + \mathbf{v}_i \quad (3.5.14)$$

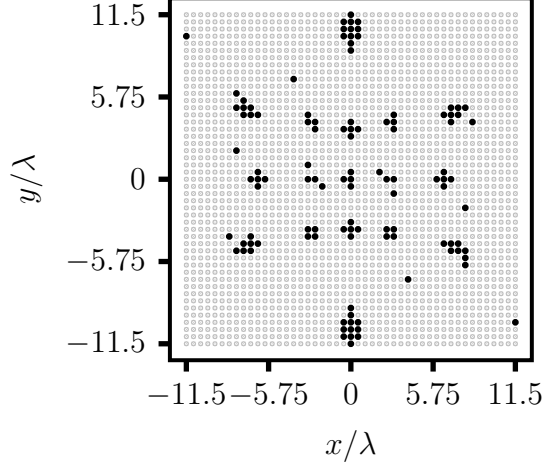


Figure 3.18: Sampling locations selected by the greedy noise factor minimization method ($X_S = 1.36\lambda$, $Y_S = 1\lambda$, $X_O = Y_O = 11.5\lambda$, $z_0 = 7\lambda$).

The maximum likelihood estimator (MLE) of this setup is defined as:

$$\hat{\mathbf{E}}_i = \sigma^{-2} \Sigma \mathbf{G}_t^{H_S \dagger} \mathbf{E}_i, \quad (3.5.15a)$$

$$\Sigma = \sigma^2 \left(\mathbf{G}_t^{H_S \dagger} \mathbf{G}_t^{H_S} \right)^{-1}. \quad (3.5.15b)$$

Confidence Ellipsoid Minimization

The first approach aims to minimize the volume of the η -confidence ellipsoid $\mathcal{E}_\alpha = \{\mathbf{z} \mid \mathbf{z}^\dagger \Sigma^{-1} \mathbf{z} \leq \alpha\}$, with $\alpha = F_{\chi_n^2}^{-1}(\eta)$, $F_{\chi_n^2}$ being the cumulative distribution function of a χ -squared random variable with n degrees of freedom, leads to:

$$\max_{\mathcal{S}} \log \det \left(\mathbf{G}_t^{H_S \dagger} \mathbf{G}_t^{H_S} \right) \quad \text{s.t.} \quad |\mathcal{S}| = H_S. \quad (3.5.16)$$

Relaxing the non-convex constraint yields a tractable optimization problem that is feasible but not equivalent to the original:

$$\max_{z_i} \log \det \left(\mathbf{G}_t^\dagger \mathbf{Z} \mathbf{G}_t \right) \quad \text{s.t.} \quad \sum_i z_i = H_S, z_i \in [0, 1], \mathbf{Z} = \text{diag}(z_i), i = 1, \dots, H. \quad (3.5.17)$$

The H_S largest z_i identify the selected points. The results of selecting $H_S = 110$ points from a $\lambda/2$ -spaced grid ($H = 2209$) are shown in Figure 3.19.

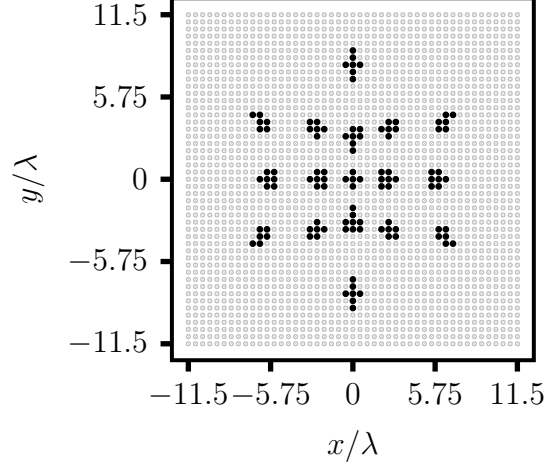


Figure 3.19: Sampling locations selected by confidence ellipsoid minimization ($X_S = 1.36\lambda$, $Y_S = 1\lambda$, $X_O = Y_O = 11.5\lambda$, $z_0 = 7\lambda$).

Mean Square Error Minimization

The second approach, which is minimizing the MSE $\mathbb{E}[\|\hat{\mathbf{E}} - \tilde{\mathbf{E}}\|^2] = \text{Tr}(\Sigma)$ gives the design:

$$\min_{z_i} \text{Tr} \left((\mathbf{G}_t^\dagger \mathbf{Z} \mathbf{G}_t)^{-1} \right) \quad \text{s.t.} \quad \sum_i z_i = H_S, z_i \in [0, 1], \mathbf{Z} = \text{diag}(z_i), i = 1, \dots, H. \quad (3.5.18)$$

Again, the H_S largest z_i are chosen. Results appear in Figure 3.20.

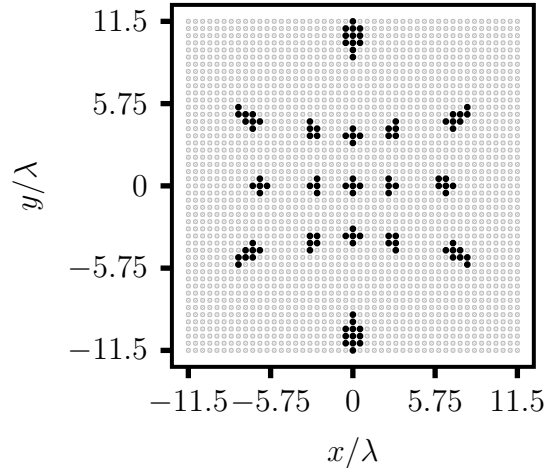


Figure 3.20: Sampling locations selected by MSE minimization ($X_S = 1.36\lambda$, $Y_S = 1\lambda$, $X_O = Y_O = 11.5\lambda$, $z_0 = 7\lambda$).

Both approaches produce sampling patterns that are qualitatively similar yet more spatially regular than those obtained via the greedy method; however, they entail substantially higher computational cost.

3.5.4 Source Domain Field Reconstruction

After measurement at the selected points, the source field is reconstructed. First, Fourier harmonics are estimated via the pseudoinverse of \mathbf{G}_t^{HS} :

$$\hat{\mathbf{E}}_i = \sum_{n=1}^L \mathbf{v}_n \frac{\mathbf{u}_n \cdot \mathbf{E}_i}{\sigma_n}, \quad (3.5.19)$$

where \mathbf{u}_n , \mathbf{v}_n , and σ_n are the left/right singular vectors and singular values of \mathbf{G}_t^{HS} . The spatial field is then synthesized by applying the inverse transform as the one shown in Equation (3.5.3) as

$$\hat{\mathbf{E}}_{i,SD}(x, y) = \sum_{m,n} \hat{\mathbf{E}}_i(m, n) \cdot e^{jk\pi\left(\frac{mx}{N_x} + \frac{ny}{N_y}\right)}. \quad (3.5.20)$$

$\hat{\mathbf{E}}_{i,SD}(x, y)$ can be used to calculate the far field via plane wave expansion.

3.5.5 Results

The simulation setup is identical to that of the previous case and is summarized as follows:

- 30 GHz standard-gain horn antenna with 10 dBi gain,
- $X_S = 4\lambda$, $Y_S = 3.5\lambda$,
- $z_0 = 2.898\lambda$.

The horn aperture ($a_{ap} = 14.06$, mm = 1.41λ , $b_{ap} = 10.5$, mm = 1.05λ) supports five distinct spatial frequency components. Since no noise is present in the simulations, only five sampling points were selected. The sampling locations were determined using a convex optimization approach that minimizes the mean squared error (MSE). The selected points are shown in Figure 3.21. Despite using less than a quarter of the sampling

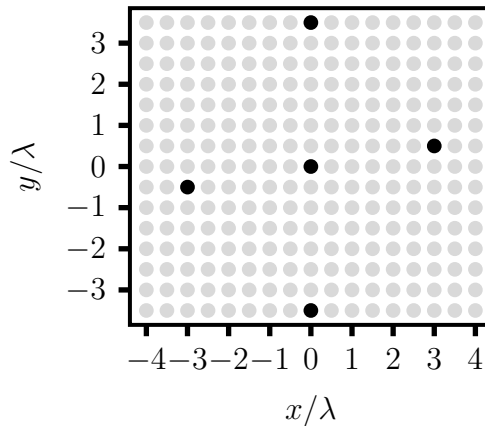


Figure 3.21: Five sampling points selected by MSE minimization from a $\lambda/2$ grid.

points compared to all other considered approaches, the reconstructed far field exhibits

superior fidelity. This improvement is observed both in the main beam region and in the angular range close to the limit of validity, which is approximately 50° in this case. The reconstructed far field is shown in Figure 3.22.

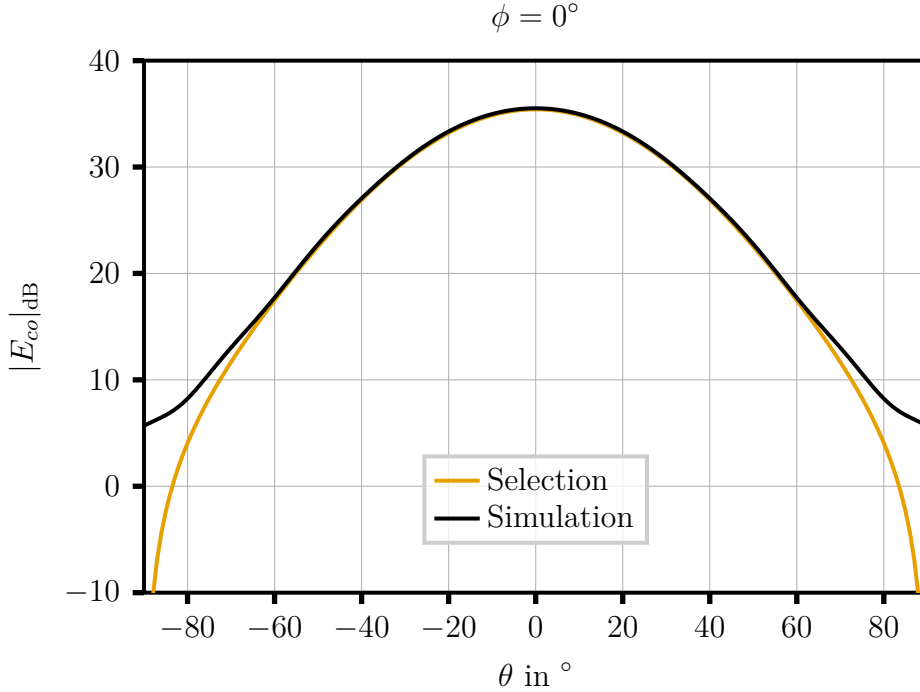


Figure 3.22: Co-polarized far-field pattern (cut in the plane $\phi = 0^\circ$) at 30 GHz of a 10-dBi standard-gain horn reconstructed from five optimally selected sampling points at a distance of $z_0 = 2.898\lambda$, compared with the simulated far field.

3.6 Gerchberg-Papoulis Algorithm

In addition to the five schemes previously described for minimizing the required near field samples, an additional strategy was investigated to reduce errors introduced by truncation. This approach is based on the Gerchberg-Papoulis algorithm (GPA) and is described in [12], [26]. The algorithm exploits a priori knowledge of the antenna geometry to mitigate far-field reconstruction errors resulting from truncated near-field measurements.

3.6.1 Methodology

The configuration, illustrated in Figure 3.23, features an antenna aperture A lying in the $z = 0$ plane, with near-field data acquired over a truncated measurement plane Σ . The GPA relies on two fundamental assumptions:

1. On the antenna under test (AUT) plane (here, $z = 0$), the electromagnetic field vanishes outside a known region A .

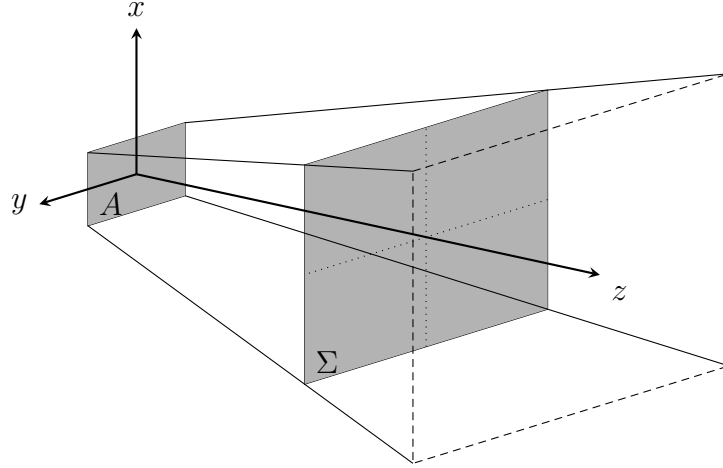


Figure 3.23: Geometric configuration of the Gerchberg-Papoulis based algorithm for reducing truncation error.

2. Certain portions of the spectrum, and consequently of the far field, computed from the near-field measurements over the scan area Σ are considered accurate. This portion of the spectrum is referred to as the reliable region and is described in Section 2.9.3.

This approach is particularly suitable when the AUT exhibits a clearly defined and physically bounded aperture field, such that the field distribution outside this region is negligible, as is the case for aperture or horn antennas.

The corresponding spectral region for which the plane-wave spectrum is considered reliable is defined by the set of (k_x, k_y) values satisfying Equation (2.9.3).

The Gerchberg-Papoulis algorithm (GPA) initiates with the near-field data measured over the scan area Σ . From these measurements, the field spectrum is computed and back-propagated to the AUT plane. Within this spectrum, only the portion belonging to the reliable region is retained. An inverse Fourier transform then yields the corresponding field distribution on the AUT plane. The electromagnetic field outside the known aperture A is subsequently set to zero. The spectrum of this modified field distribution is obtained by applying a forward Fourier transform. Within this new spectrum, the reliable region is replaced by the reliable region extracted from the initial spectrum derived from the measured near field. The procedure then repeats; each iteration consists of alternating enforcement of spatial and spectral domain constraints, respectively. After convergence, the far field is computed from the final spectrum, which retains the original, measurement-based reliable region. A simplified illustration of the iterative process is provided in Figure 3.23.

3.6.2 Gradient Descent for Convergence Control

A well-known limitation of the GPA is its sensitivity to measurement errors: according to [26], convergence is guaranteed only in the absence of noise. While convergence was observed with purely synthetic data generated by numerical evaluation of the near field from an ideal aperture on an infinite ground plane, divergence occurred even with noise-free simulated data. Specifically, outside the reliable angular region, the reconstructed far-field amplitude begins to increase after a certain number of iterations, eventually approaching levels comparable to the main beam. Consequently, early termination of the iterative process is essential.

This diverging behavior renders an appropriate stopping criterion crucial. [12] proposes partitioning the same measurement domain Σ into two subsets, denoted S_1 and S_2 . These subsets are generated from the initial plane-wave spectrum with two different values of C , the parameter that controls the size of the reliable region, as defined in Equation (3.6.2). The algorithm seeks the pair of iteration counts, one for each subset, that minimizes the discrepancy μ , defined as

$$\mu = \sum_{\theta, \phi} |\mathbf{E}_{S_1}(\theta, \phi) - \mathbf{E}_{S_2}(\theta, \phi)|^2. \quad (3.6.1)$$

Rather than exhaustively comparing all intermediate reconstructions, [26] introduces a gradient descent algorithm (GDA) to streamline this process. The procedure alternates GPA iterations between S_1 and S_2 : if updating with a given subset reduces μ , the same subset is used again; if μ increases, the algorithm switches to the other subset. Termination occurs when an update with either subset causes μ to rise.

3.6.3 Selection of the Reliability Scaling Factor C

The GDA does not address the selection of the parameter C , which scales the theoretical boundary of the reliable angular region. In practice, spectral components near the edge of this region are often degraded by truncation effects. Thus, only the spectrum within a reduced boundary

$$\tilde{\theta}'(\phi) = C\theta'(\phi) \quad (3.6.2)$$

is retained as reliable.

According to [26], values of C between 0.35 and 0.8 typically yield low reconstruction errors. However, this range is broad, and empirical results confirm that the choice of C significantly influences performance. For conventional $\lambda/2$ -spaced planar scans of a 10-dBi standard-gain horn antenna, optimal results were achieved with values of C approaching unity.

In contrast, when near-field data are acquired using a plane-polar non-redundant sampling scheme, the measurement surface is theoretically bounded by the maximum radial sampling distance. Crucially, the near field is extrapolated beyond this boundary with high fidelity. Under these conditions, it is reasonable to consider $C > 1$, where the baseline reliable region is defined by the outermost radius of the non-redundant grid. Empirical evaluation indicates that $C = 1.1$ yields the best reconstruction.

3.6.4 Results

The algorithm was first tested with data generated from a canonical aperture as described in Section 2.6. Initial results indicated favorable performance. When applying the same method to simulation data of a 10-dBi standard-gain horn operating at 30 GHz, the improvements in the far-field pattern obtained by applying the GPA were less convincing. For the results presented here, the near field was sampled on a regular $\lambda/2$ grid 2.89λ above the horn aperture on a domain with the size $13\lambda \times 13\lambda$, which results in an angle of validity in the principal planes of $\theta'_x = 63.5^\circ$ and $\theta'_y = 64.2^\circ$. The gradient descent algorithm was used and the parameter C was set to 1. The improvement offered by the application of the GPA depends strongly on the considered ϕ cut of the far field. In some cases, the improvements are significant, such as in the $\phi = 20^\circ$ cut depicted in Figure 3.24, while in others, e.g., $\phi = 70^\circ$ depicted in Figure 3.25, the far field outside the reliable region appears to diverge.

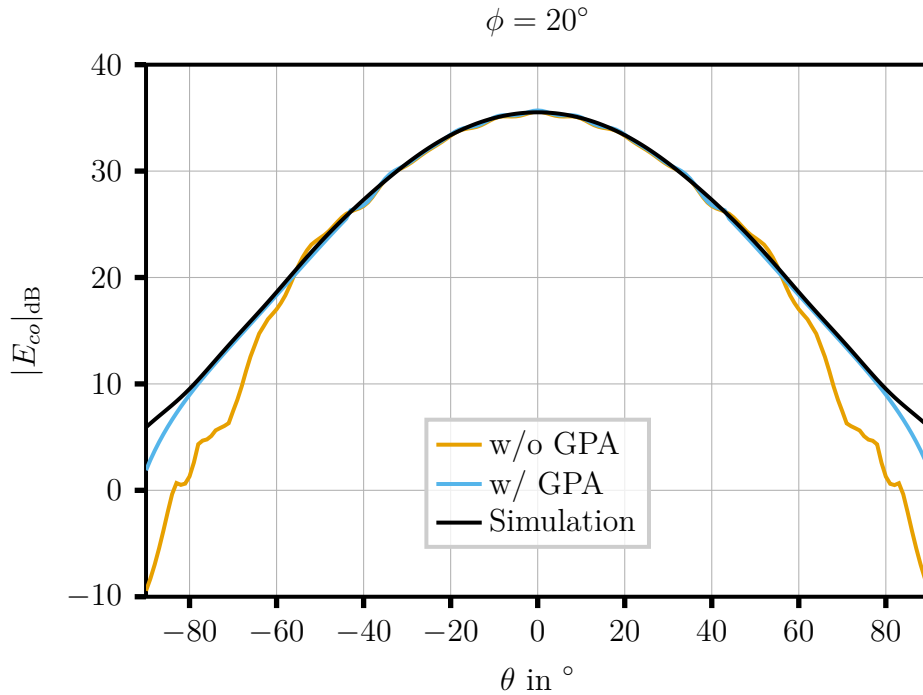


Figure 3.24: Co-polarized far-field pattern (cut in the plane $\phi = 20^\circ$) at 30 GHz of a 10-dBi standard-gain horn reconstructed from uniform $\lambda/2$ sampling with and without the application of the GPA in comparison to the simulated far field.

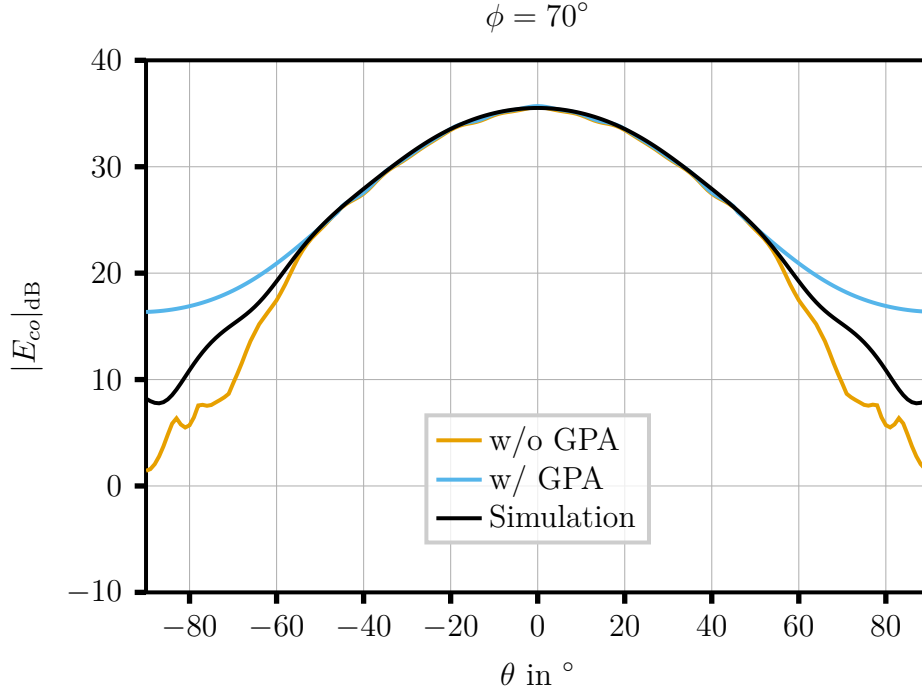


Figure 3.25: Co-polarized far-field pattern (cut in the plane $\phi = 70^\circ$) at 30 GHz of a 10-dBi standard-gain horn reconstructed from uniform $\lambda/2$ sampling with and without the application of the GPA in comparison to the simulated far field.

More importantly, the performance of the GPA in conjunction with the GDA exhibits limited predictability, and slight changes in C cause significantly different results. The correct choice of C varies depending on the size of the measurement domain, the antenna, and the measurement distance z . Collectively, these factors make the algorithm difficult to apply effectively. Consequently, given the project timelines and the observed sensitivities, further investigation of this method was discontinued.

3.7 Conclusion

This section has evaluated five distinct strategies for reconstructing antenna far-field patterns from undersampled near-field measurements. Each method reflects a different trade-off among theoretical foundation, reliance on prior knowledge of the radiating source, computational complexity, and sampling efficiency.

The Non-redundant sampling and Warping-based approaches, though derived from different geometric assumptions, share a common conceptual structure: both introduce a parametrization of the observation domain that equalizes the spatially varying bandwidth of the measured field, followed by sinc based interpolation of equispaced samples in the transformed domain. The key practical distinction lies in their source modeling: Non-redundant sampling encloses the antenna within a rotational ellipsoid and derives the

parametrization rigorously from electromagnetic theory, whereas the warping approach assumes a rectangular source support and tailors the parametrization to the common case where the measurement aperture is at least as large as the source projection.

In contrast, the remaining three methods adopt fundamentally different philosophies. The ‘‘Igloo’’ scheme replaces conventional planar Nyquist sampling ($\lambda/2$ spacing) with a projection of a spherical Nyquist grid onto the measurement plane, thereby enforcing angular sampling constraints rather than Cartesian ones. The minimum-rank (min. Rank) approach requires no prior geometric information about the source and does not try to find optimal sampling points; instead, it selects sampling points randomly from a fixed lattice and relies on a hybrid interpolation strategy combining nuclear norm minimization (to promote low-complexity field representations) with thin-plate spline smoothing (to enforce spatial correlation).

Finally, the greedy sampling point selection method bypasses near-field reconstruction altogether: it directly estimates the equivalent source currents on a known source domain by selecting an optimal subset of measurement points from a candidate grid. A notable distinction is that the first four methods aim to reconstruct the near field over the entire measurement plane, while the selection-based approach targets the underlying source distribution, enabling far-field computation via forward propagation.

Name	Source Modeling	Approach	Samp. efficiency	
Non-red.	Rotational Ellipsoid	Parametrized OD	High	(22/255)
Warping	Rectangle	Parametrized OD	High	(25/255)
Igloo	Sphere	Sphere-to-plane proj.	Low	(76/255)
min. Rank	No apriori inf.	Rank minimization	Poor	(127/255)
Selection	Rectangle	Source current recon.	Very High	(5/255)

Table 3.2: Qualitative comparison of the five considered sampling and interpolation schemes.

As summarized in Table 3.2, methods that incorporate accurate prior knowledge of the antenna geometry, namely non-redundant sampling, warping, and greedy selection, achieve significantly higher sampling efficiency than those that do not. In our test case (a WR34 10-dBi standard-gain horn), these informed methods required only 5-25 samples to achieve high-fidelity far-field reconstruction up to $\theta \approx 50^\circ$, whereas Igloo needed 76 samples and min. Rank required 127, even then yielding lower accuracy. Thus, while simpler or agnostic methods reduce modeling effort or eliminate geometric assumptions, they do so at the cost of either increased sample count (Igloo) or higher computational burden (min. Rank).

Complementing these sampling strategies, the Gerchberg-Papoulis Algorithm (GPA) was

investigated as a post-processing technique to mitigate truncation errors inherent in limited measurement domains. While initial tests indicated that the GPA can effectively suppress artifacts and improve reconstruction fidelity under specific conditions, its performance proved highly sensitive to parameter selection and measurement geometry. The algorithm exhibited unpredictable convergence behavior, where slight variations in the reliability scaling factor led to significant discrepancies in the far-field pattern, including divergence outside the reliable angular region. Due to this lack of robustness and the substantial computational effort required for stabilization via gradient descent, a comprehensive optimization was not pursued within the scope of this work. Nevertheless, given its theoretical potential to recover information from truncated data without increasing the physical sample count, the GPA remains a promising avenue for future research once more adaptive stopping criteria are established.

Chapter 4

Minimizing Samples in a Limited Acquisition Area: Proposed Method and Comparative Analysis

To enable a meaningful evaluation of the five sampling schemes introduced in Chapter 3, a realistic measurement scenario is considered. The objective is to characterize the far-field pattern of an antenna from planar near-field measurements, where the acquisition area is limited to a rectangular domain of dimensions $2X_O \times 2Y_O$. The comparison aims to determine which of the five sampling schemes achieves the most accurate far-field reconstruction while requiring the smallest possible number of near-field samples.

Except the non-redundant sampling approach, all schemes inherently permit restriction of the acquisition area. Consequently, an adaptation of the non-redundant sampling method was developed to ensure consistency with the comparison framework and to allow a fair and unbiased performance assessment.

The subsequent sections detail the modifications introduced to the non-redundant scheme, followed by a comprehensive description of the evaluation framework, including the measurement setup, performance metrics, and the results obtained from the two conducted comparative studies involving all five sampling strategies.

4.1 Adapting the Non-Redundant Sampling Grid

As discussed in Section 3.1, the non-redundant sampling scheme generates sampling points along radial lines, which, in principle, can extend indefinitely. In practice, however, the measurement area is constrained by the finite observation domain. Consequently, a procedure is required to adjust the sampling grid to ensure that all points remain within

the available measurement region.

Conversely, there are cases in which the nominal grid may occupy only a portion of the observation domain, leaving additional space unused. In such situations, the sampling grid can be extended to increase the area over which the reconstructed field is reliable.

To address these scenarios, three specific strategies were implemented. All strategies start by generating the nominal sampling grid, determined by the radial positions and the number of angular samples per radius, based solely on the antenna geometry and the measurement distance z_0 .

4.1.1 Replacing Sampling Radii

Limiting the Spatial Extent of the Sampling Grid

In the first proposed variant, any radial line containing one or more sampling points lying outside the observation domain is discarded. A single radial line is then located at the largest radius that remains fully contained within the OD. However, this replacement radius does not correspond to an equispaced node in the transformed ξ -domain, which is a prerequisite for the validity of the interpolation formula (3.1.19).

To restore consistency with the original interpolation scheme, the field value at a fictitious sampling radius, located at the correct equispaced ξ -position, is reconstructed via a linear inversion. Specifically, let r_1, \dots, r_M (with associated parameters ξ_1, \dots, ξ_M) denote the original radii whose sampling points lie entirely within the OD, and let r_{M+1}, \dots, r_N (with ξ_{M+1}, \dots, ξ_N) be the excluded radii. These are replaced by a single physical radius r' at the boundary of the OD, corresponding to parameter ξ' .

For a given azimuth angle ϕ_0 , the axial (inner) interpolation step, corresponding to the inner sum in Equation (3.1.19), is first performed using the available real samples, yielding the reduced field values $\mathbf{F}(\xi_n, \phi_0)$ for $n = 1, \dots, M$ and the additional value at ξ' . The contribution of each sampling radius to the reduced field at (ξ', ϕ_0) is then computed as

$$\mathbf{F}_n(\xi', \phi_0) = \Omega_N(\xi' - \xi_n) D_{N''}(\xi' - \xi_n) \mathbf{F}(\xi_n, \phi_0), \quad n = 1, \dots, M, M + 1, \quad (4.1.1)$$

where the index $M + 1$ refers to the fictitious missing equispaced sampling radius.

The interpolation condition requires that the total field at (ξ', ϕ_0) equals the sum of all individual contributions:

$$\mathbf{F}(\xi', \phi_0) = \sum_{n=1}^{M+1} \mathbf{F}_n(\xi', \phi_0). \quad (4.1.2)$$

This equation is solved for the unknown reduced field value at the missing equispaced

location ξ_{M+1} :

$$\mathbf{F}(\xi_{M+1}, \phi_0) = \frac{\mathbf{F}(\xi', \phi_0) - \sum_{n=1}^M \mathbf{F}_n(\xi', \phi_0)}{\Omega_N(\xi' - \xi_{M+1}) D_{N''}(\xi' - \xi_{M+1})}. \quad (4.1.3)$$

With this reconstructed value, the outer sum of the original interpolation formula Equation (3.1.19) can be evaluated using the set of radii ξ_1, \dots, ξ_{M+1} , thereby enabling accurate field reconstruction at any (ξ, ϕ_0) .

Increasing the Spatial Extent of the Sampling Grid

The procedure for the case in which the outermost radial sampling line does not fully exploit the available observation domain follows the same principles as in the limiting case. In contrast to the previous scenario, however, no existing sampling radii are removed. Instead, an additional radial line is introduced at the maximum admissible radius within the observation domain.

To maintain compatibility with the interpolation framework, the newly introduced physical radius does not, in general, coincide with an equispaced node in the transformed ξ -domain. Therefore, the same reconstruction strategy as described above is applied. In particular, the field value at the required equispaced fictitious ξ -position is determined via the linear inversion procedure outlined in Equation (4.1.3). Once this reconstructed value is obtained, the interpolation formula Equation (3.1.19) can be evaluated using the augmented set of sampling radii.

4.1.2 Squeezing Sampling radii

Limiting the Spatial Extent of the Sampling Grid

An alternative strategy to accommodate the constraint that the measurement radii must be equispaced in the transformed ξ -domain is not only to replace the external radii, those whose sampling points fall outside the observation domain, with a single radius $r' = r(\xi')$ located at the OD boundary, but also to rearrange (or “squeeze”) the remaining internal radii. This rearrangement ensures that all retained radii, including the new boundary radius, are equispaced in the ξ -domain while preserving their original count.

Because this modification reduces the physical extent of the internal radii, the angular sampling density on each radius must be updated accordingly using Equations (3.1.16) and (3.1.17). As a consequence, the number of angular samples per radius either remains unchanged or decreases.

However, this squeezing operation violates a second fundamental assumption underlying the original interpolation formula (3.1.19): namely, the 2π -periodicity of the radial sampling grid, which is guaranteed by the definition of $\Delta\xi$ in Equation (3.1.15a). Without

this periodicity, the Dirichlet kernel-based interpolation (Equation (3.1.18a)) fails, as the radial samples no longer coincide with the zeros of the convolution of other samples with the Dirichlet kernel. To restore interpolation fidelity, the Dirichlet kernel was replaced by a sinc-like kernel:

$$D'_L(x) = \frac{\sin\left(\frac{2L+2}{2}x\right)}{(2L+1)\frac{x}{2}}. \quad (4.1.4)$$

Aside from this substitution, the remainder of the interpolation procedure remains unchanged.

In practice, the “squeezing” approach consistently yielded more accurate reconstructions than the simpler strategy of merely replacing external radii. Moreover, the latter method involves computing a fictitious field value at (ξ_{M+1}, ϕ_0) via Equation (4.1.3), which can become numerically unstable in the presence of noise, particularly when the denominator approaches zero due to unfavorable geometry. The squeezing method avoids this instability and additionally reduces the total number of required sampling points. For these reasons, it was adopted for all subsequent applications.

Increasing the Spatial Extent of the Sampling Grid

Analogous to the reduction case, the extension of the sampling grid under the squeezing strategy is performed by introducing a new radial sampling line at the largest radius fully contained within the observation domain. In this case, no existing radii are discarded. Instead, all radii, including the newly added outermost one, are redistributed such that they remain equispaced in the transformed ξ -domain.

This redistribution requires a corresponding adjustment of the angular sampling density on each radius, ensuring consistency with the updated radial positions. The number of angular samples per radius is recalculated accordingly. The interpolation is then carried out using the modified radial grid and the sinc-like kernel previously introduced, while all remaining steps of the procedure remain unchanged.

4.1.3 Qualitative Comparison

To qualitatively compare the two approaches used to limit the spatial extent of the acquisition grid starting from the non-redundant samples, a rectangular source domain of size $2.5\lambda \times 2.5\lambda$ is considered. The corresponding observation domain is located at a distance of $z = 8.24\lambda$. Using oversampling and excess bandwidth factors of $\chi = \chi' = 1$, the resulting non-redundant grid consists of 65 sampling points distributed over five concentric radii, with the outermost radius equal to 13.0λ . This original sampling grid is depicted by black crosses in Figure 4.1.

The sampling area is now constrained to a maximum radius of 9λ , which renders the

outermost sampling ring of the original grid inadmissible. Two different strategies are employed to enforce this constraint.

In the first approach, described in Section 4.1.1, the outermost measurement radius is removed and replaced by a new radius at 9λ , while all remaining radii are left unchanged. This modification results in a sampling grid consisting of 63 sampling points distributed over five radii. In the second approach, referred to as the squeezing method and described in Section 4.1.2, all sampling radii are uniformly reduced such that the equidistant spacing in the ξ -domain is preserved. This approach yields a sampling grid with 61 sampling points on five radii.

The resulting modified sampling grids obtained with both approaches are shown in comparison with the original grid in Figure 4.1.

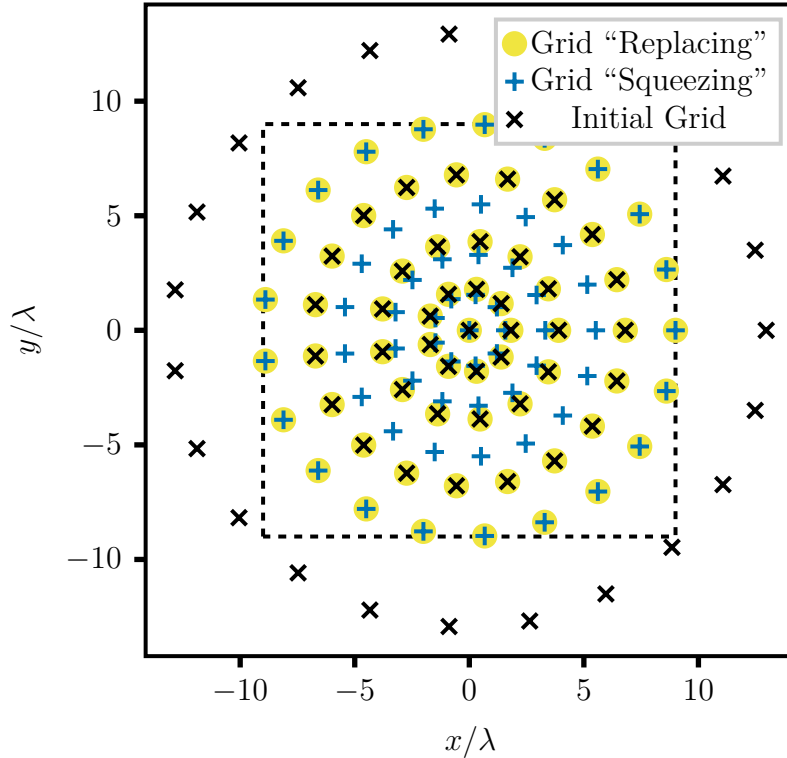


Figure 4.1: Visualization of the replacement and squeezing methods used to adapt the original sampling grid to a restricted $18\lambda \times 18\lambda$ region, marked by the dashed line.

For the subsequent comparisons of the different sampling schemes, the “squeezing” methodology was adopted to ensure that the sampling grid fully exploits the available constrained observation domain. In the following, this approach is referred to as “squeezing” or modified non-redundant sampling.

4.2 Quantitative Comparison on a 10-dBi Standard-Gain Horn

The five sampling and interpolation schemes summarized in Table 3.2 were evaluated in a realistic scenario using full-wave simulation data of a WR34 10-dBi standard-gain horn operating at 30 GHz. The near field is sampled at twice the Fresnel distance, $d = 0.62\sqrt{D^3/\lambda}$, from the antenna aperture. Here, D denotes the effective diameter of the radiator, defined as the diagonal of the rectangular aperture: $D = \sqrt{a_{\text{ap}}^2 + b_{\text{ap}}^2}$, with aperture dimensions $a_{\text{ap}} = 14.06$ mm and $b_{\text{ap}} = 10.5$ mm. This yields a measurement distance of $z = 2d = 28.8$ mm $= 2.898\lambda$.

The observation domain is rectangular, with half-extents $X_O = 39.97$ mm $= 4\lambda$ and $Y_O = 34.98$ mm $= 3.5\lambda$, resulting in angular validity limits of $\theta_x = 48.8^\circ$ and $\theta_y = 45.9^\circ$ in the principal planes as shown in Section 2.9.3. Uniform Nyquist sampling ($\lambda/2$ spacing) along both axes over this domain would require a 17×15 grid, corresponding to 255 samples.

While the minimum-rank approach permits interpolation only onto the original uniform lattice, in this case a $\lambda/2$ -spaced grid, the igloo method, based on bilinear interpolation, enable the evaluation of the electric field at arbitrary points within the observation domain. Here, the field was interpolated onto a $\lambda/4$ -spaced grid covering the same domain.

Both the non-redundant sampling and the warping approaches theoretically support interpolation at any point in the observation plane. However, interpolated values far from the central region of the observation domain tend to be inaccurate and degrade overall performance. Consequently, the near field was interpolated onto a $\lambda/4$ grid extended to $1.3 \cdot 2X_O \times 1.3 \cdot 2Y_O$, which yielded consistent and accurate results.

To adapt the non-redundant sampling grid to the fixed observation domain, the “squeezing” modification described in Section 4.1.2, which was developed in the course of this work, was applied. In the warping approach, the oversampling parameters were consistently chosen such that the ratio satisfied $1.3\nu_1 = \nu_2$. Within the minimum-rank method, the pseudo-random sampling point selection outlined in Section 3.4.2 was employed with parameter $\alpha = 50$. Finally, in the selection-based algorithm, the optimal sampling points were determined using the confidence ellipsoid minimization method detailed in Section 3.5.3.

4.2.1 Metrics

To enable a meaningful comparison among the different algorithms, the following quantitative metrics were introduced.

Undersampling Ratio

The undersampling ratio is defined as the ratio between the number of samples employed by a given algorithm and the number of points in a $\lambda/2$ -spaced uniform grid over the same observation domain (255 points in this case). It thus provides a measure of the fraction of samples retained relative to the conventional Nyquist-rate sampling scheme.

Different undersampling ratios were achieved by adjusting the specific parameters of each sampling scheme: χ for the modified non-redundant approach (with $\chi' = 1$ fixed), ν_1 and ν_2 for the warping approach (while maintaining the relation $1.3\nu_1 = \nu_2$), and ν for the igloo approach. For the minimum-rank and selection-based algorithms, the number of samples used can be directly specified.

Baseline

The baseline refers to the performance in terms of NMSE achieved using the full $\lambda/2$ -spaced uniform sampling grid over the observation domain (255 points), against which all undersampled methods are compared.

Normalized Mean Square Error

The primary metric for evaluating far-field reconstruction fidelity is the Normalized Mean Square Error (NMSE), defined as the ratio of the squared error between the magnitude of the reconstructed far field $\hat{\mathbf{E}}_{ff}(\theta, \phi)$ and the reference far field $\mathbf{E}_{ff}(\theta, \phi)$, obtained from full-wave simulation, to the total power of the reference far field:

$$\text{NMSE} = \frac{\sum_{\theta, \phi} \left| |\mathbf{E}_{ff}(\theta, \phi)| - |\hat{\mathbf{E}}_{ff}(\theta, \phi)| \right|^2}{\sum_{\theta, \phi} |\mathbf{E}_{ff}(\theta, \phi)|^2}. \quad (4.2.1)$$

This quantity represents the relative power of the reconstruction error with respect to the total radiated power in the far field. To ensure a fair and meaningful comparison, the NMSE is computed only over the angular region, in both azimuth and elevation, deemed reliable according to the validity limits specified in Equation (2.9.3), as reconstructions outside this region are inherently inaccurate due to the limited spatial support of the observation domain.

Computation Time

The computation time is defined as the total CPU time required to execute two key stages of each method: (i) the generation or selection of the sampling points (or measurement grid), and (ii) the subsequent interpolation. This timing excludes any data loading or post-processing steps and focuses solely on the core algorithmic operations. The measurement is

performed using a processor time counter, representing an assessment of the computational burden associated with each approach.

4.2.2 Results using Noiseless Data

In the first series of simulations, no additional noise is introduced on the near-field samples; the uncorrupted full-wave simulation data is used directly as input to the various algorithms.

Normalized Mean Square Error

The resulting NMSE values across varying undersampling ratios are presented in Figure 4.2.

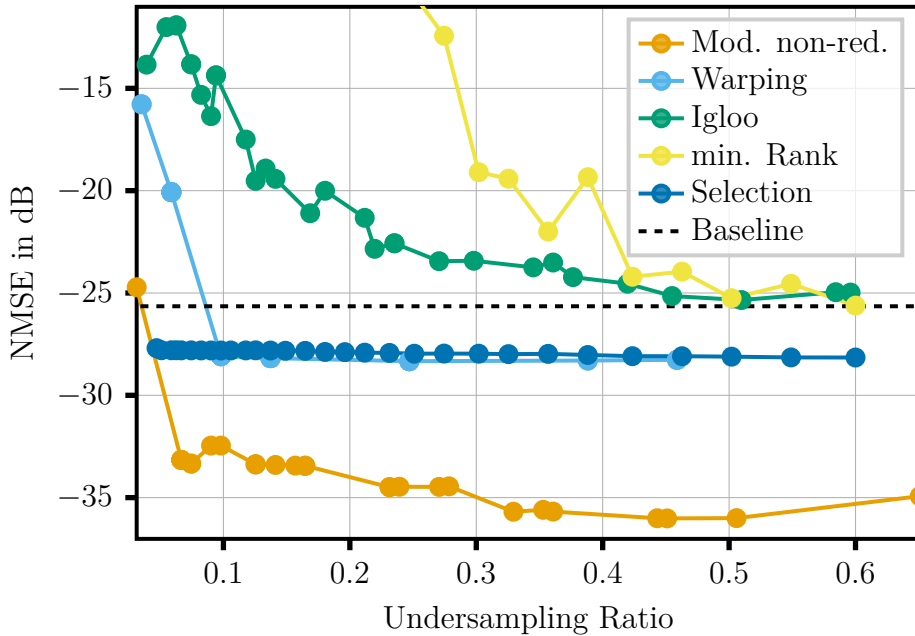


Figure 4.2: NMSE as a function of the undersampling ratio. The results are obtained from simulated near-field data of a 10-dBi standard-gain horn over a confined acquisition area of $4\lambda \times 3.5\lambda$, in the absence of measurement noise.

The modified non-redundant, warping, and selection methods achieve superior far-field reconstruction accuracy compared to the baseline, even when using less than 10% of the samples required by the Nyquist scheme. This performance advantage stems from two distinct mechanisms: (i) for the modified non-redundant and warping approaches, the near field is interpolated onto a grid that is both larger in spatial extent and finer in resolution ($\lambda/4$ spacing over $1.3 \cdot 2X_O \times 1.3 \cdot 2Y_O$) than the baseline grid, thereby capturing more spectral content; (ii) for the selection method, the optimally chosen sample points enable an accurate representation of the aperture field, which translates into high-fidelity far-field reconstruction despite extreme undersampling.

In contrast, both the igloo and minimum-rank approaches interpolate the near field onto a grid identical in size and resolution to that of the baseline ($\lambda/2$ spacing over $X_O \times Y_O$). Consequently, their reconstruction fidelity cannot exceed that of the baseline; at best, they asymptotically approach it as the number of samples increases. As shown in Figure 4.2, these two methods are consistently outperformed by the other three across all undersampling levels.

An alternative perspective focuses on the number of samples required to match the baseline reconstruction quality within a prescribed tolerance. Figure 4.3 shows the undersampling ratio needed for each method to achieve an NMSE within 1 dB, 3 dB, and 5 dB of the baseline NMSE. The modified non-redundant, warping, and selection methods require the same small number of samples to satisfy all three tolerances, reflecting the rapid decay of their NMSE in the low-sampling regime. In comparison, igloo and minimum-rank demand significantly more samples to reach the 1 dB margin. When larger deviations are permitted (3 dB and 5 dB), igloo clearly outperforms the minimum-rank approach, although both remain substantially less efficient than the top-performing methods.

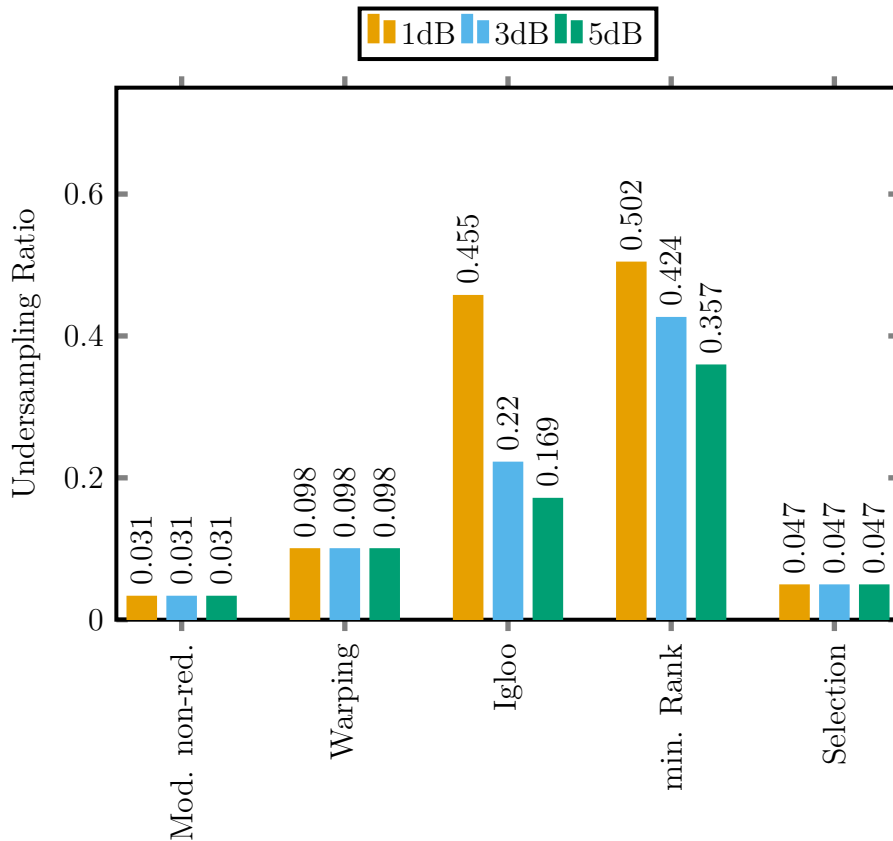


Figure 4.3: Undersampling ratio required to achieve NMSE within 1 dB, 3 dB, and 5 dB of the baseline NMSE. Noiseless simulation near-field data have been considered.

To illustrate the differences between the sampling strategies, Figure 4.4 compares the reconstructed far-field patterns obtained with the modified non-redundant, igloo, and

selection-based sampling schemes to the simulated far-field reference. The three approaches employ 113, 110, and 102 near-field samples, respectively, corresponding to an under-sampling ratio of approximately 0.1. To achieve this sampling density, the oversampling parameter of the modified non-redundant method was set to $\chi = 2.75$, while for the igloo method $\nu = 1.21$ was chosen.

As already indicated by the NMSE results in Figure 4.2, the igloo method exhibits inferior performance both within and outside the reliable angular region. In contrast, the far field reconstructed from the modified non-redundant near-field samples closely follows the simulated reference within the reliable region and does not exhibit noticeable ripples or significant deviations. However, outside this region, the reconstruction accuracy deteriorates and becomes comparable to that of the igloo approach. In the vicinity of the validity limit, the modified non-redundant method still provides improved agreement, which can be attributed to its ability to interpolate over a domain larger than the original measurement region.

The selection-based approach demonstrates superior performance outside the reliable region compared to the other two methods. This behavior results from the spectral reconstruction of the equivalent source current distribution, rendering the far-field accuracy less dependent on the angular validity limit. Within the reliable region, the reconstructed far-field pattern is smooth and in good agreement with the simulated data. Nevertheless, the magnitude is slightly underestimated, leading to a higher NMSE than that of the modified non-redundant scheme. The improved reconstruction outside the reliable region is not reflected in the NMSE values, as this angular range is excluded from the error computation, as described in Section 4.2.1.

Computational Complexity and Runtime

The computational effort required by the different reconstruction methods varies significantly. For comparison, the total computation time was measured as the sum of the time required to generate the sampling grid and the time required to interpolate the measured samples onto the grid used for far-field computation. The resulting computation times are shown in Figure 4.5.

The modified non-redundant sampling, warping, and igloo approaches employ relatively simple procedures for sampling grid generation. Furthermore, their interpolation steps are based on either sinc convolution or bilinear interpolation, which are computationally efficient operations. As a result, these methods exhibit low computation times.

In contrast, the minimum-rank approach requires the solution of a convex optimization problem that seeks a matrix of minimum rank defined on the corresponding $\lambda/2$ lattice over the observation domain. This optimization problem is computationally demanding and

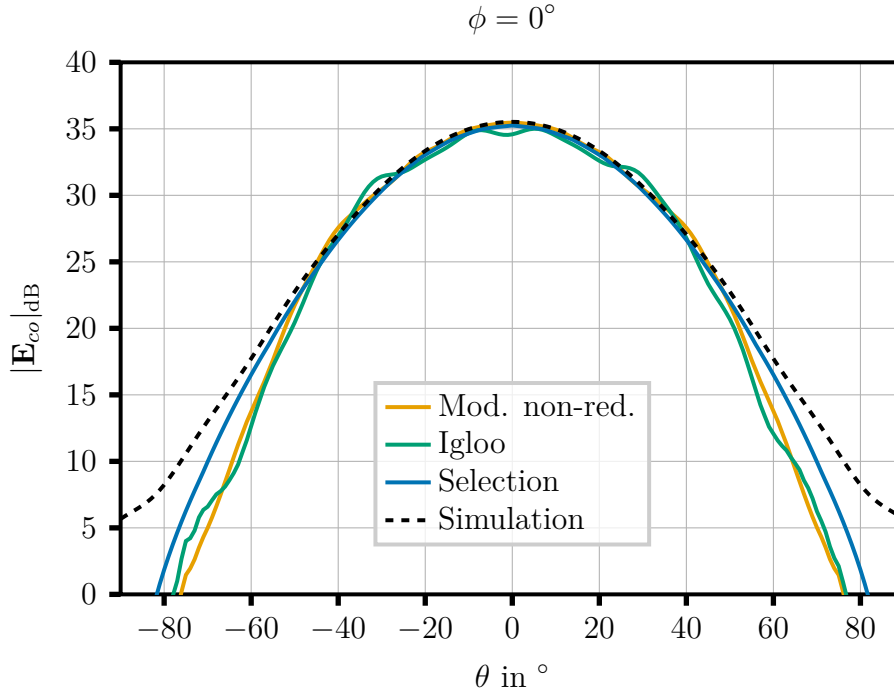


Figure 4.4: Co-polarized far-field pattern (cut in the plane $\phi = 0^\circ$) at 30 GHz of a 10-dBi standard-gain horn reconstructed from ~ 110 near-field samples (corresponding to an undersampling ratio of ~ 0.1) at a distance of $z = 2.89\lambda$ using three different sampling schemes, compared to the simulated far-field data.

exhibits a substantially higher computational complexity than the approaches employed by the other methods. For larger observation domains, the required computational resources increase rapidly, as the problem complexity scales on the order of $\mathcal{O}(N^2)$, where N is the total number of near-field samples.

The selection method exhibits a higher computational cost than the former sampling-based approaches, primarily due to the convex optimization used to select sampling points that minimize the volume of the confidence ellipsoid, as defined in Equation (3.5.16). When the sampling points are instead selected to minimize the mean square error, as formulated in Equation (3.5.18), the computational burden increases further.

The greedy selection strategy originally proposed in [19], however, offers a significantly more efficient alternative. It provides a practical fallback solution in scenarios with numerous candidate sampling points, where convex optimization-based methods become computationally infeasible.

4.2.3 Consideration on the Impact of Noise

In contrast to the previous simulations, additive white Gaussian noise (AWGN) is introduced in the following study to evaluate the robustness of the investigated reconstruction algorithms with respect to measurement noise. Apart from the addition of noise, the

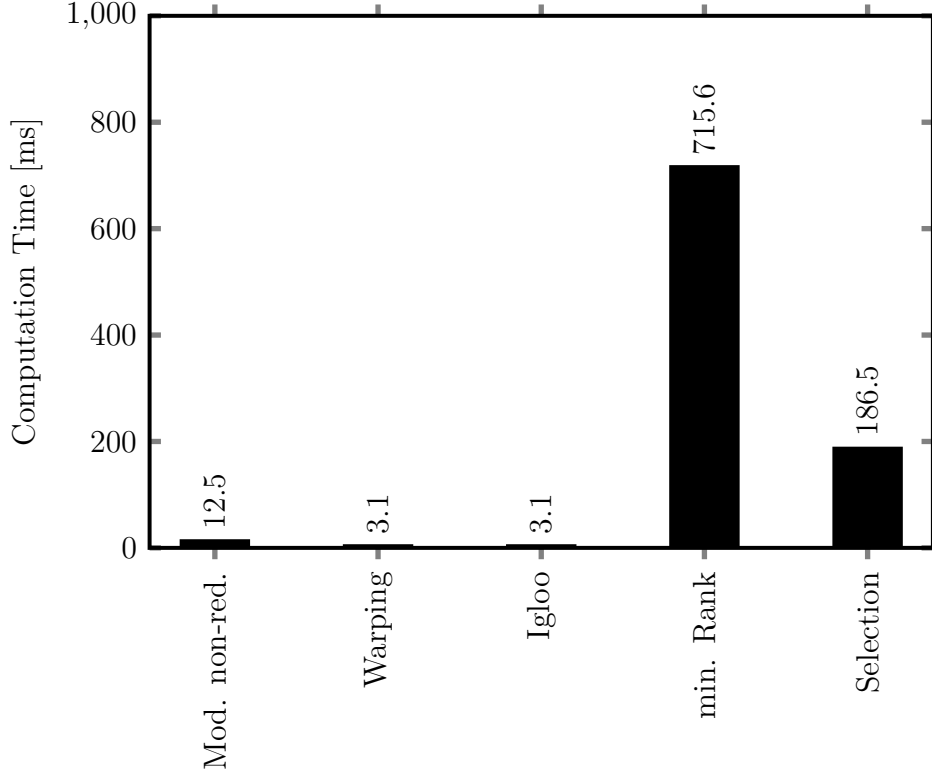


Figure 4.5: Average computation time for sampling grid generation and interpolation for the different reconstruction methods.

simulation setup remains unchanged. To reduce statistical fluctuations caused by the random noise realization, each simulation run is repeated five times and the results are averaged.

The noise power is defined via the signal-to-noise ratio (SNR) as

$$P_{N,x,y} = \frac{P_{S,x,y}}{\text{SNR}}, \quad (4.2.2)$$

where $P_{S,x,y}$ denotes the signal power of the respective near-field component. The signal power is computed as the spatial average of the $\lambda/2$ -sampled baseline near-field data. The x - and y -components are treated independently and are given by

$$P_{S,x} = \frac{1}{N_x N_y} \sum_{k,l} |E_x(x_k, y_l)|^2, \quad P_{S,y} = \frac{1}{N_x N_y} \sum_{k,l} |E_y(x_k, y_l)|^2, \quad (4.2.3)$$

where N_x and N_y are the number of near-field samples in x - and y -direction respectively. For each near-field sample, the noise is generated as a complex-valued random variable whose real and imaginary parts are drawn independently from a zero-mean normal distribution. Both components have a variance of

$$\sigma_{x,y}^2 = \frac{P_{N,x,y}}{2}, \quad (4.2.4)$$

ensuring that the total noise power corresponds to the specified SNR. In the following, noise levels corresponding to SNR values of 20 dB and 10 dB are considered.

The resulting normalized mean square error (NMSE) as a function of the undersampling ratio is shown in Figure 4.6 for an SNR of 20 dB. The results are based on simulated near-field data of a 10-dBi standard-gain horn, considered in Section 4.2.2, at 30 GHz.

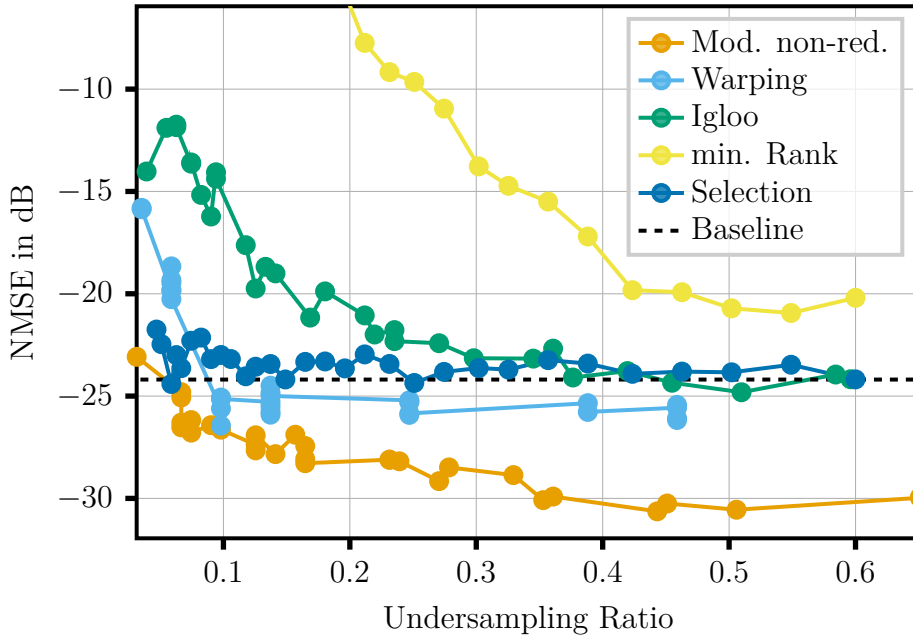


Figure 4.6: NMSE as a function of the undersampling ratio. The results are obtained from simulated near-field data of a 10-dBi standard-gain horn over a confined acquisition area of $4\lambda \times 3.5\lambda$, with additive white Gaussian noise at an SNR of 20 dB applied to the data.

The overall trend remains consistent with the noise-free case shown in Figure 4.2. However, notable differences can be observed. In particular, the minimum-rank approach fails to reach the baseline performance even using moderate undersampling ratios (0.6). In contrast, the igloo approach exhibits the opposite behavior: baseline performance is approximately achieved with a lower number of samples. As a result, the performance gap between the minimum-rank and igloo approaches increases significantly in the presence of noise.

The remaining three methods continue to outperform the baseline even for undersampling ratios as low as 0.1, similar to the noise-free scenario. Notably, the selection method is able to match the precision of the modified non-redundant sampling approach.

These observations are further supported by the results summarized in Figure 4.7. The 1 dB bar for the minimum-rank method is absent, indicating that none of the tested undersampling ratios achieves a reconstruction accuracy within 1 dB of the baseline NMSE for this approach.

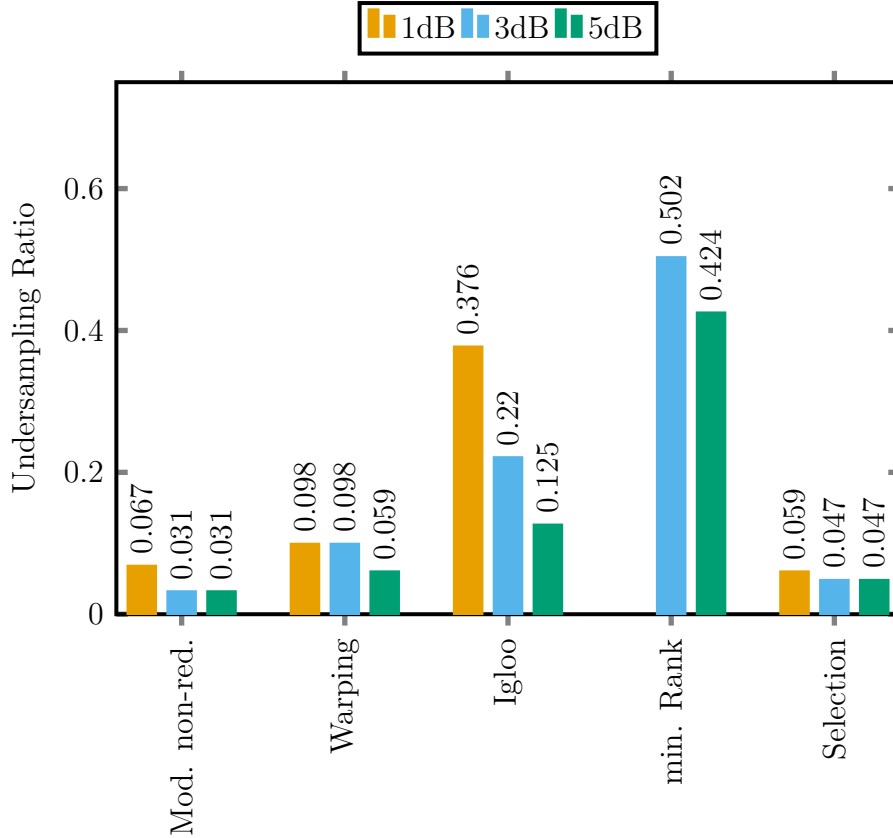


Figure 4.7: Undersampling ratio required to achieve an NMSE within 1 dB, 3 dB, and 5 dB of the baseline NMSE for an SNR of 20 dB.

When the noise level is increased to a corresponding SNR of 10 dB, the previously observed trends persist, as illustrated in Figure 4.8. The minimum-rank approach again performs worst among all evaluated methods. The performance of the igloo approach converges toward that of the modified non-redundant sampling and warping approaches, particularly at higher undersampling ratios. In contrast, the selection method begins to outperform all other approaches and appears to exhibit increased robustness against noise. This behavior is corroborated by the results shown in Figure 4.9.

4.2.4 Concluding Remarks on the Comparative Analysis

The quantitative comparison of the analyzed methods in terms of number of samples and quality of the near field to far field reconstruction clearly demonstrates that the incorporation of prior knowledge and a more refined treatment of the source geometry have a decisive impact when undersampled near-field measurements are considered. Methods that explicitly exploit such information significantly outperform approaches that rely on more generic assumptions.

In particular, the minimum-rank approach, which does not incorporate prior knowledge about the source geometry or radiation characteristics, exhibits limited undersampling

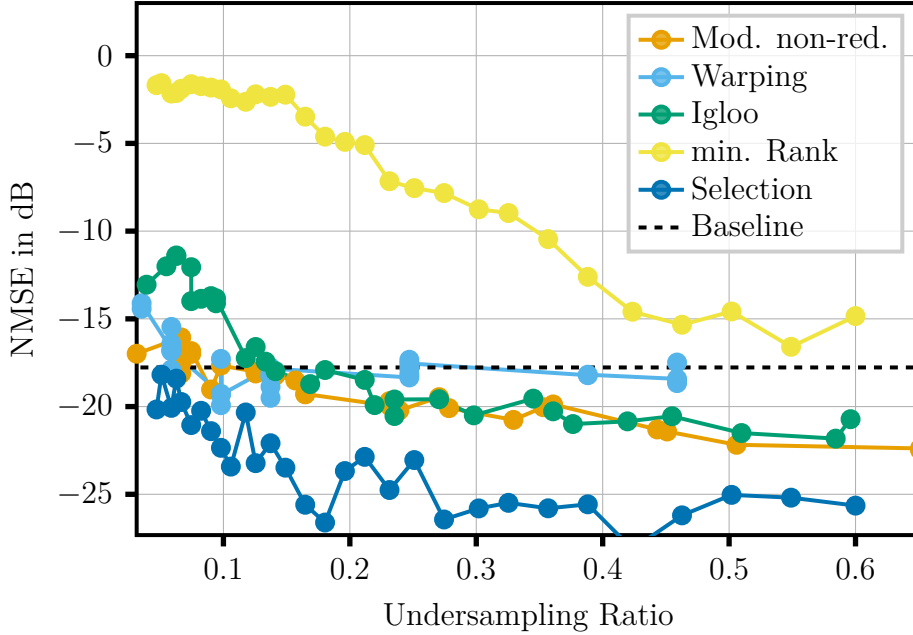


Figure 4.8: NMSE as a function of the undersampling ratio. Results are based on simulated data from a 10-dBi standard-gain horn with a confined acquisition area and 10 dB additive white Gaussian noise.

capability. In the investigated scenarios, it achieves a reduction in sampling density by approximately a factor of two relative to conventional $\lambda/2$ sampling, while incurring substantial computational cost. Consequently, its performance remains unsatisfactory both in terms of reconstruction accuracy and efficiency when some information about the antenna under test is available.

In contrast, the proposed sampling scheme based on the non-redundant approach, warping, and selection-based methods reduce the number of required samples by factors in the order of 20. Moreover, the quality of the far-field reconstruction which these approaches achieve with a finer sampling, still coarser than Nyquist, is better than that obtained with uniform $\lambda/2$ sampling. This improvement is enabled by a more informed use of the underlying physics, either through spectral-domain considerations or through explicit modeling of the source representation.

The igloo method, which employs a simple bilinear interpolation strategy and does not explicitly account for the source geometry, exhibits inferior performance compared to the best-performing methods in the noise-free case. However, its robustness in the presence of measurement noise is noteworthy, yielding results that are comparable to more sophisticated approaches under moderate noise levels. This highlights the potential of simple, computationally efficient techniques in practical measurement scenarios.

Among all investigated methods, the selection-based approach consistently demonstrates the highest robustness to measurement noise. Its fundamentally different strategy-based on

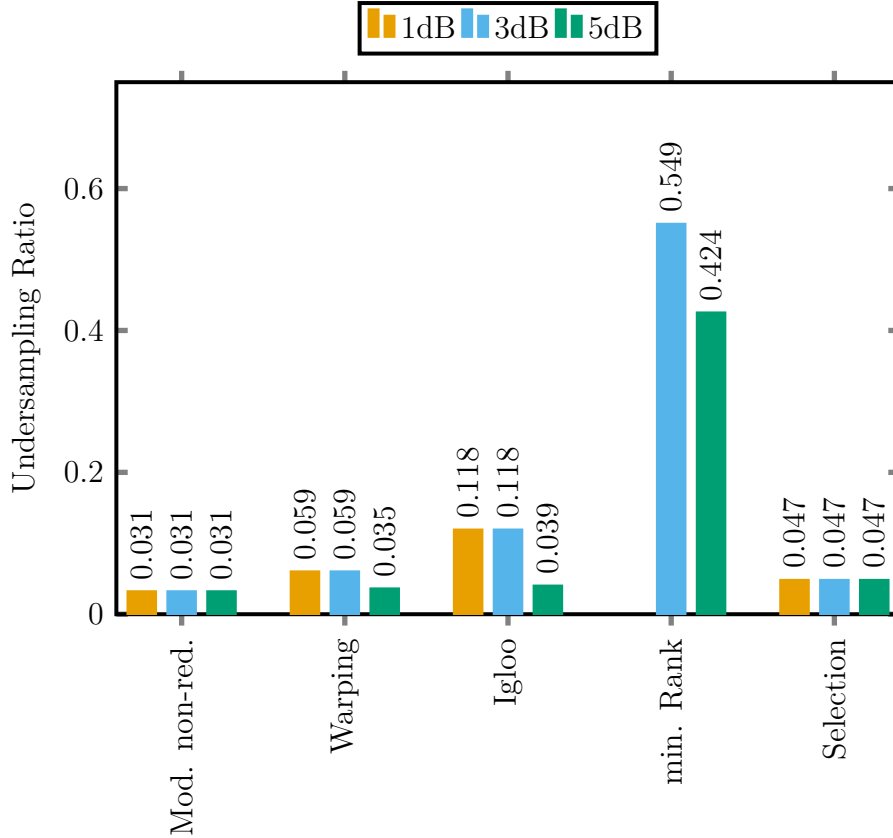


Figure 4.9: Undersampling ratio required to achieve an NMSE within 1 dB, 3 dB, and 5 dB of the baseline NMSE for an SNR of 10 dB.

reconstructing source harmonics rather than directly interpolating spatial samples-enables both aggressive undersampling and effective noise suppression, making it a particularly promising candidate for future applications.

The warping approach is methodologically related to modified non-redundant sampling and does not provide a clear performance advantage in the examined scenarios. Moreover, the selection of appropriate oversampling parameters ν_1 and ν_2 proves to be nontrivial and sensitive, which limits its practical appeal. For this reason, the warping approach is not considered further in the subsequent comparisons. Similarly, due to its high computational complexity and limited reconstruction performance, the minimum-rank method is excluded from further analysis.

As a result, the remainder of this work focuses on three representative approaches: modified non-redundant sampling, which offers robust and consistently high performance at the cost of increased algorithmic complexity; igloo, which represents a simple efficient baseline with competitive noise robustness; and the selection-based method, which emerges as the most powerful approach in terms of undersampling capability and noise resilience.

4.3 Quantitative Comparison Based on Measurement Data

A second quantitative study is conducted using planar near-field measurements of a WR51 20-dBi standard-gain horn. In this setup, described in [30], an electro-optic probe is used for field acquisition. The analysis focuses on three representative sampling strategies:

- Modified non-redundant sampling (Section 3.1),
- Igloo sampling (Section 3.3),
- Selection-based sampling (Section 3.5).

Since independent far-field measurements are not available, the reconstructed far fields obtained from the reduced sampling schemes are compared with a reference solution. This reference is computed via plane-wave expansion using the complete set of measured near-field samples.

4.3.1 Dataset and Evaluation Procedure

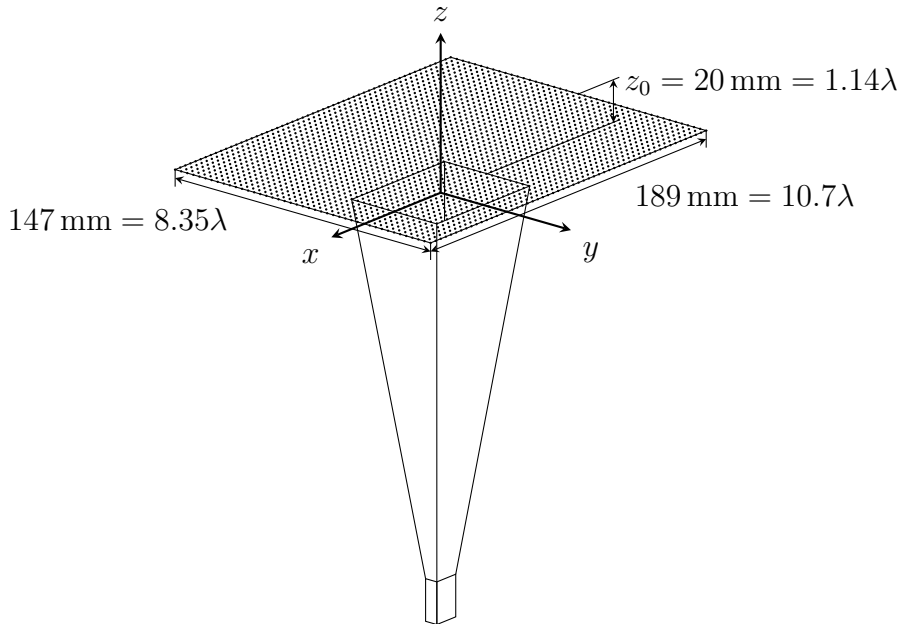


Figure 4.10: Measurement configuration of the 20-dBi standard-gain horn and planar acquisition surface (drawn to scale).

The dataset consists of planar near-field measurements of a WR51 20-dBi standard-gain horn operating at 17.025 GHz. The horn aperture measures 63.75 mm by 49 mm (3.62λ by 2.78λ). The near field is sampled at a distance of $z_0 = 20 \text{ mm} = 1.14\lambda$ over an area of $189 \text{ mm} \times 147 \text{ mm}$ ($10.7\lambda \times 8.3\lambda$), as illustrated in Figure 4.10. The measurement grid is uniform with step sizes $\Delta x = \Delta y = 3.5 \text{ mm} = 0.199\lambda$, resulting in $55 \times 43 = 2365$ samples

acquired with an electro-optic probe. This configuration provides validity angles in the principal planes of $\theta'_x = 72.3^\circ$ and $\theta'_y = 67.8^\circ$.

The magnitude and phase of the y -polarized near field, corresponding to the principal polarization of the antenna under test, are shown in Figure 4.11 and Figure 4.12, respectively. The near-field magnitude at the boundary of the measurement domain is on average 34.5 dB below the maximum field magnitude. This indicates that the field levels outside the measured domain are relatively low and are therefore not expected to contribute significantly to the far-field pattern.

The phase distribution exhibits anomalous behavior in the vicinity of $y = 0$, $|x| > 2.5\lambda$. In particular, the phase difference between adjacent sampling points located immediately to the left and right of this position approaches π . Such a discontinuity strongly suggests the presence of measurement inaccuracies or post-processing errors in the acquired data. Nevertheless, since it affects a limited part of the acquisition area where the field amplitude is quite low, the overall results remain largely coherent. The subsequent comparison of reconstruction methods is therefore considered meaningful within these limitations.

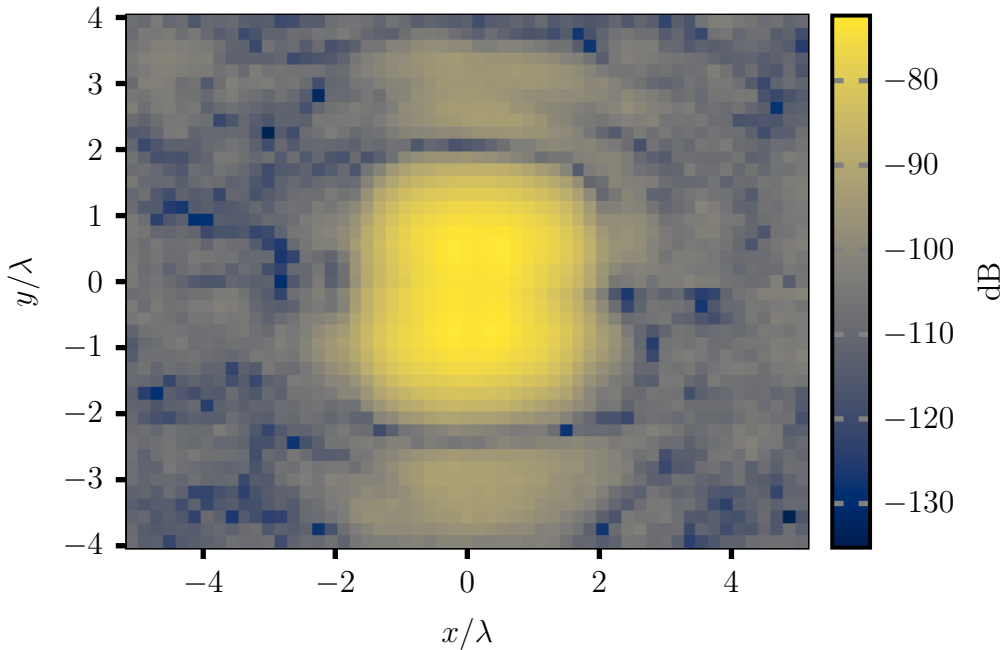


Figure 4.11: Magnitude of the measured y -polarized near field at $z = 20 \text{ mm} = 1.14\lambda$. The average edge taper is approximately 34.5 dB.

For the application of the different sampling schemes, the electric field is first reduced according to

$$\mathbf{F}(\mathbf{r}) = \mathbf{E}(\mathbf{r})e^{jk|\mathbf{r}|}, \quad (4.3.1)$$

interpolated to the desired positions using cubic interpolation, and subsequently expanded by multiplication with $e^{-jk|\mathbf{r}|}$.

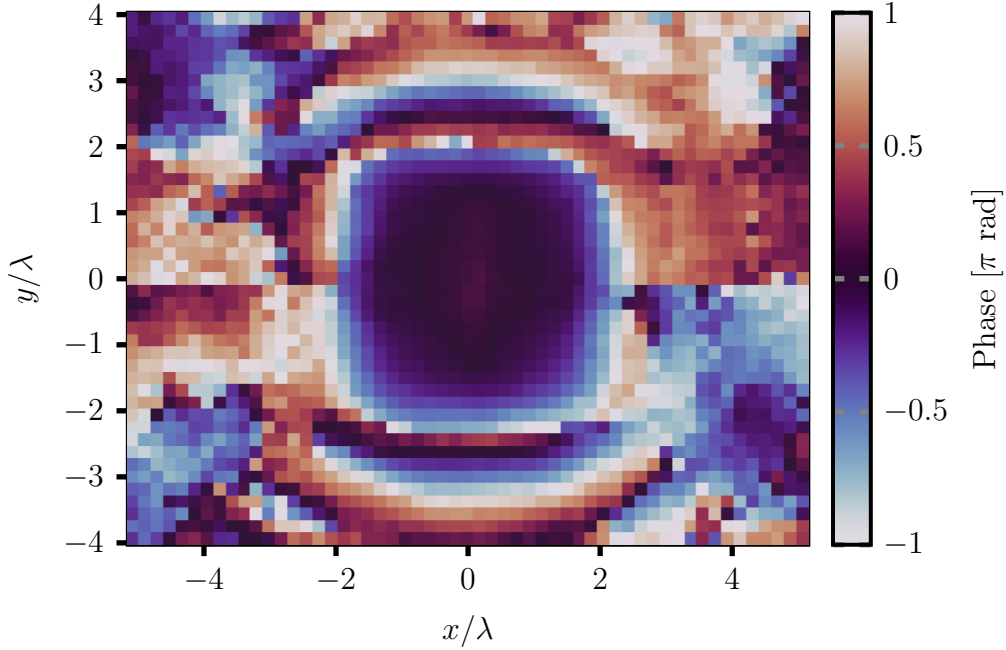


Figure 4.12: Phase of the measured y -polarized near field, normalized to π , at $z = 20 \text{ mm} = 1.14\lambda$.

The employed performance metric corresponds to the NMSE defined in Equation (4.2.1). In the absence of measured far-field data, the reference field \mathbf{E}_{ff} is replaced by the far field obtained via PWE from all 2365 near-field samples.

As in the previous study, the effective observation domain for all sampling schemes is restricted, namely to $123 \text{ mm} \times 106 \text{ mm}$ ($7\lambda \times 6\lambda$), yielding validity angles of $\theta'_x = 56.1^\circ$ and $\theta'_y = 54.8^\circ$.

For the modified non-redundant approach, the sampling density is controlled by the oversampling parameter χ , whereas for the Igloo method the parameter ν is varied. The candidate set for the selection-based algorithm is chosen as a Cartesian $\lambda/2$ grid. The modified non-redundant samples are interpolated onto a $\lambda/4$ grid extended to a rectangle with 1.3 times the side length of the observation domain. In contrast, the Igloo samples are interpolated onto a $\lambda/4$ grid covering the observation domain only.

As a baseline, the far field derived from the $\lambda/2$ -sampled near-field data over the $123 \text{ mm} \times 106 \text{ mm}$ region, consisting of 195 samples is used.

4.3.2 Results

The NMSE obtained for the three sampling strategies as a function of the undersampling ratio is shown in Figure 4.13. In comparison to the simulation-based study, the behavior observed in the measurement-based evaluation differs noticeably. This deviation can be attributed in part to the modified reference: the reconstructed far fields are compared

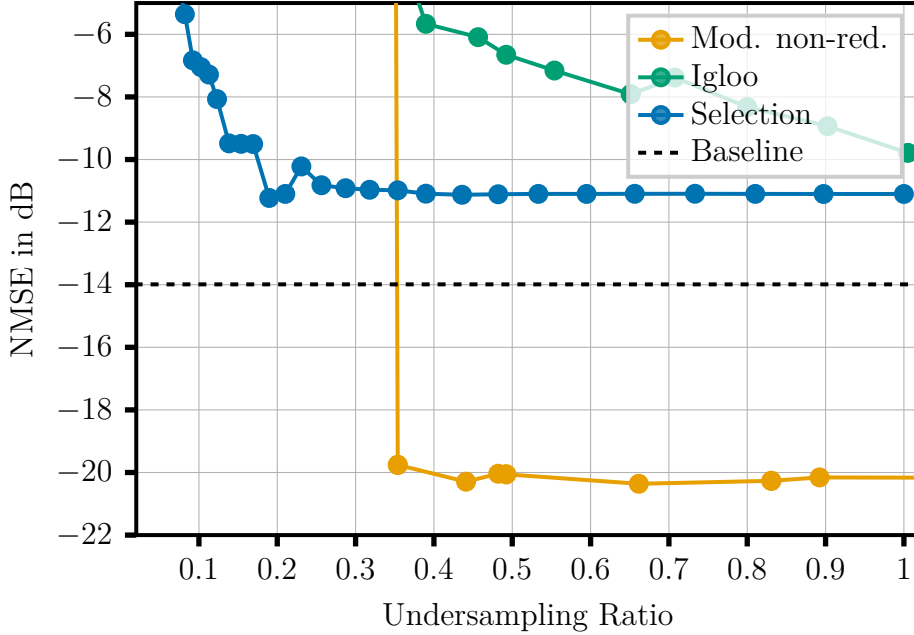


Figure 4.13: NMSE as a function of the undersampling ratio evaluated from near-field measurements of a 20-dBi standard-gain horn over an acquisition area of size $3.5\lambda \times 3\lambda$, at a distance 1.14λ from the horn aperture.

to the PWE solution derived from the measured near field rather than to independent far-field measurements.

The Igloo method does not reach the baseline performance, even when a comparable number of samples is used. In contrast, the modified non-redundant sampling scheme exhibits a pronounced reduction in NMSE starting from an undersampling ratio of approximately 0.35, corresponding to $\chi \approx 0.9$. Since $\chi \geq 1$ is generally recommended, reliable performance can be expected in this regime. As in the simulation-based scenario, the modified non-redundant method is able to outperform the $\lambda/2$ baseline. This is attributed to the fact that the near field can be interpolated beyond the measurement domain.

A representative far-field cut reconstructed from 94 modified non-redundant near-field samples ($\chi = 1$), corresponding to an undersampling ratio of 0.48, is shown in Figure 4.14a and compared to the reference field obtained from all available measurements. Even for angles exceeding the validity limit of $\theta'_x = 56.1^\circ$, good agreement with the reference solution is observed.

The selection-based method achieves low NMSE values already at undersampling ratios around 0.15. In the present configuration, 45 spatial harmonics are supported over the assumed source domain, corresponding to an undersampling ratio of 0.231. This value may therefore serve as a practical lower bound for reliable sampling in comparable scenarios.

However, in contrast to the simulation-based case, the selection-based approach does not

achieve NMSE values lower than that obtained with the $\lambda/2$ baseline, even for higher sample counts. The reason why the reconstructed equivalent source currents fail to accurately represent the true field distribution remains unclear. One possible explanation is an incorrect choice of the source domain, for instance the approximation of the radiating region to the horn aperture only. Another contributing factor may be the defective phase distribution of the measured near field shown in Figure 4.12, which could render the measured field incompatible with any physically realizable current distribution over the assumed source region.

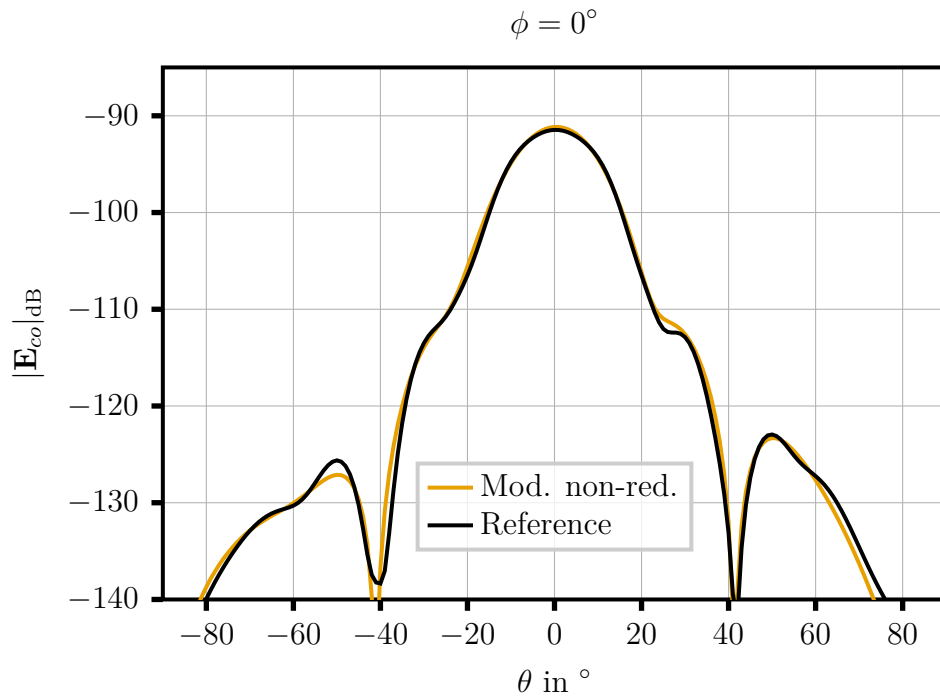
The far-field reconstruction obtained with 39 near-field samples is shown in Figure 4.14b. While the main beam is reconstructed accurately, deviations from the reference pattern become noticeable for $|\theta| \gtrsim 30^\circ$. Beyond approximately 40° , the agreement with the reference solution deteriorates significantly.

4.3.3 Concluding Remarks on the Comparative Analysis

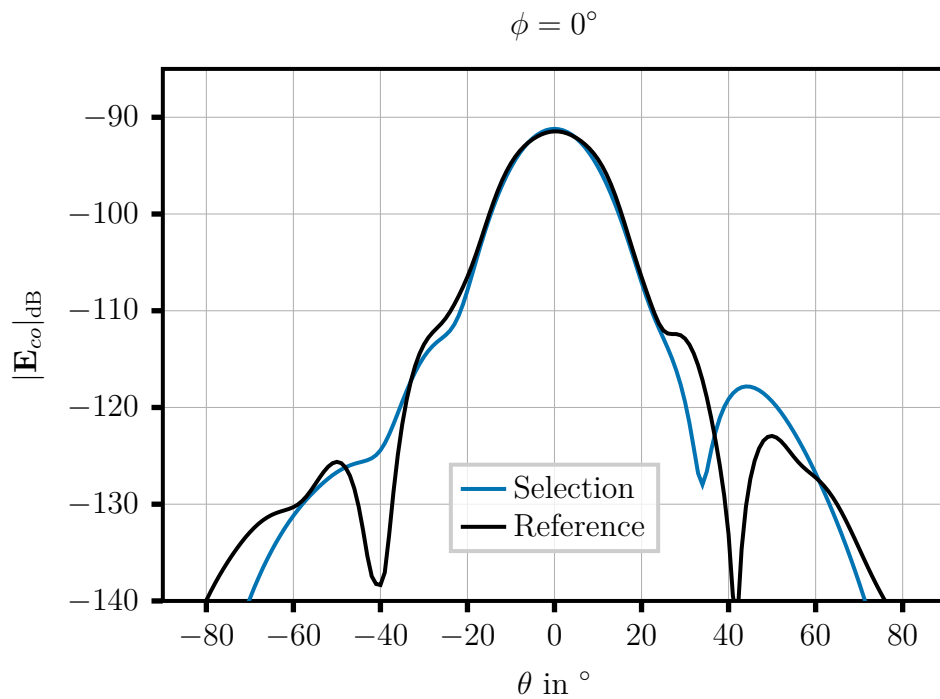
The measurement-based evaluation confirms and further strengthens the trends observed in the simulation study. The Igloo sampling scheme is clearly outperformed by both the modified non-redundant and the selection-based approaches. In contrast to the previous comparison, it is now not even capable of reaching the $\lambda/2$ baseline performance, even for undersampling ratios approaching unity. This behavior indicates that the performance of the Igloo method does not follow a consistent or predictable trend with increasing sampling density, which limits its practical reliability.

The proposed sampling approach based on the non-redundant scheme again proves to be robust and dependable. It achieves an NMSE of less than -20 dB already for strong undersampling (about 0.3) and clearly surpasses the $\lambda/2$ baseline. In particular, the case $\chi = 1$ already yields very good reconstruction accuracy, suggesting that this parameter choice as a practical rule of thumb. The consistent performance across both numerical and experimental studies validates the effectiveness of the proposed definition of the near field acquisition grid and controlled oversampling strategy.

The selection-based method delivers acceptable results but performs noticeably worse than anticipated based on the simulation-based study. In the measurement scenario, it does not reach baseline performance, and the underlying reason remains unclear. Possible causes include modeling inaccuracies of the equivalent source domain or inconsistencies in the measured phase distribution. Further investigation is therefore required to clarify the limitations of this approach under realistic measurement conditions. Overall, the results demonstrate that the increased complexity of the modified non-redundant and selection-based methods can provide substantial benefits, while simpler sampling strategies such as the Igloo scheme lacks robustness in practical measurement scenarios.



(a)



(b)

Figure 4.14: Co-polarized far-field pattern (cut in the plane $\phi = 0^\circ$) at 17.025 GHz of a 20-dBi standard-gain horn reconstructed from planar near-field measurements at $z = 20 \text{ mm} = 1.14\lambda$: (a) non-redundant sampling (94 samples), (b) selection-based method (39 samples). Both results are compared to the reference far field obtained via PWE from all 2365 available near-field samples.

Chapter 5

Conclusion

The primary objective of this work was to investigate, implement, and evaluate efficient sampling strategies for the characterization of the far-field pattern of an antenna starting from downsampled and truncated planar near-field measurements. While analytical formulas exist for far-field reconstruction when the near field is available over a complete plane and sampled at the Nyquist rate, developing robust numerical implementations for spatially confined observation domains remains a significant engineering challenge. This report transitioned from the fundamental theory of wave propagation (Chapter 2) to a rigorous comparative analysis of diverse sampling approaches (Chapters 3 and 4), ultimately proposing novel adaptations to address the minimization of near-field measurement over a finite area while preserving highly accurate FF reconstruction

Review of the Plane Wave Expansion and its Performance

The foundation of the near-field to far-field transformation (NFFFT) employed throughout this work relies heavily on the Plane Wave Expansion (PWE) method, detailed in Chapter 2. Derived from Maxwell's equations and the subsequent Helmholtz wave equations, the PWE framework allows any electromagnetic field in a source-free, linear, homogeneous, and isotropic medium to be expressed as a continuous superposition of elementary plane waves.

By framing the electric field as a two-dimensional inverse Fourier transform of its plane wave spectrum, the NFFFT circumvents the need for highly computationally intensive numerical integration of electromagnetic potentials. Instead, Fast Fourier Transforms (FFTs) can be leveraged to efficiently transition between spatial near-field data and the angular far-field spectrum. The performance of the PWE method proved exceptionally robust; as demonstrated in Section 2.11, the far-field computations obtained via PWE perfectly matched the analytical solutions for canonical aperture test cases.

However, the practical application of the PWE method requires careful numerical handling. Because near-field measurements are bounded by finite spatial domains, passing this data directly through Fourier transforms without sufficient zero-padding introduces severe Gibbs phenomenon artifacts, manifesting as pronounced ripples in the reconstructed near field due to jump discontinuities at the aperture edges. Once properly mitigated through extensive zero-padding, the PWE method formed a highly reliable, exact, and computationally lightweight foundation for all subsequent far-field calculations in this thesis.

Gerchberg-Papoulis Algorithm for Truncation Error Mitigation

A fundamental limitation of planar near-field measurements is the finite extent of the observation domain, which inevitably leads to incomplete coverage of the radiated field and results in truncation errors. These errors corrupt the far-field reconstruction outside a specific angular bound, known as the Angle of Validity (AOV) or the reliable region. To address this without requiring additional measurement samples, the Gerchberg-Papoulis Algorithm (GPA) was investigated in Section 3.6 as a post-processing mitigation technique.

The GPA is an iterative procedure that leverages alternating projections between the spatial and spectral domains. It enforces two a priori assumptions: first, that the electric field in the spatial domain vanishes outside the known physical aperture of the antenna under test; and second, that the plane-wave spectrum computed from the truncated measurement plane remains accurate strictly within the theoretical reliable region.

While initial tests on canonical theoretical apertures indicated that the GPA possesses the theoretical potential to recover lost spectral information, its application to realistic standard-gain horn scenarios yielded inconsistent and highly unstable results. The algorithm exhibited extreme sensitivity to the parameter C , which scales the theoretical boundary of the reliable region. Furthermore, the GPA inherently struggles with convergence in the presence of even negligible noise, often leading to a severe divergence of the far-field pattern outside the reliable region. Although incorporating a Gradient Descent Algorithm (GDA) to establish a dynamic stopping criterion improved stabilization, the method ultimately lacked the necessary predictability and robustness.

Implementation and Review of the Five Sampling Schemes

The core of this work consisted of implementing and benchmarking five distinct near-field sampling schemes, as detailed in Chapter 3 and evaluated in Chapter 4. These methods reflect a diverse spectrum of trade-offs regarding theoretical complexity, sampling efficiency, and reliance on prior geometric knowledge of the radiating source.

Igloo Sampling: The Igloo approach replaces traditional Cartesian Nyquist sampling with a spherical-to-planar projection. Points are selected by mapping a uniform spherical grid onto the measurement plane, followed by a simple bilinear interpolation. While the method is computationally trivial and agnostic to the source exact geometry, this simplicity comes at a severe cost. It demonstrated low sampling efficiency, requiring significantly more points (e.g., 76 points for the 10-dBi horn) than more informed methods while simultaneously yielding lower accuracy both inside and outside the reliable region.

Minimum-Rank Interpolation: Representing an entirely source-agnostic philosophy, this method interpolates a heavily undersampled, randomly selected subset of lattice points by enforcing general electromagnetic properties. It reconstructs the field by combining nuclear norm minimization (a convex surrogate to promote low-complexity field representations) with Thin-Plate Spline (TPS) smoothing. While conceptually elegant, it proved computationally prohibitive due to $O(N^2)$ scaling. Furthermore, it consistently exhibited the poorest far-field reconstruction accuracy among all methods, completely failing to reach the precision achieved using standard NFFFT with near-field data sampled with a $\lambda/2$ step.

Warping-Based Sampling: This highly informed method models the antenna using equivalent currents on a rectangular planar domain. By analyzing the phase of the Green’s function, it introduces a spatially varying coordinate transformation (warping) that equalizes the local bandwidth of the field, enabling aggressive undersampling. While it achieved high sampling efficiency (e.g., 25 samples), the parametrization is strictly analytically valid only when the observation domain is smaller than or equal to the source domain. Applying it to realistic measurement geometries requires a heuristic, spatially varying oversampling factor (ν_1, ν_2) that proved highly sensitive and lacked a firm physical grounding, ultimately rendering the method less reliable than alternative geometry-aware approaches.

Selection-Based (Greedy/Convex) Sampling: This method departs fundamentally from the others by bypassing direct near-field interpolation. Instead, it aims to reconstruct the spatial harmonics of the equivalent source current on the antenna aperture. It utilizes convex optimization (e.g., minimizing the confidence ellipsoid or Mean Square Error) to select the optimal subset of measurement locations from a uniform grid that best suppresses noise propagation. By reconstructing the source directly, this technique inherently circumvents near-field truncation errors. It achieved exceptional theoretical performance, requiring mere single-digit sample counts (e.g., 5 samples) in noiseless conditions, and exhibited unparalleled robustness to noise (at 10 dB and 20 dB SNR).

However, when applied to measured data, the performance proved to be significantly

less convincing and did not reach the accuracy achieved by the non-redundant sampling scheme. Further investigation is therefore required to determine whether the discrepancy arises from impaired phase accuracy in the measurements or from intrinsic limitations of the proposed reconstruction approach.

Non-Redundant Sampling: Grounded in the rigorous derivation of the Number of Degrees of Freedom (NDF) of a radiated field, this method encloses the source antenna within a rotational ellipsoid. By establishing an optimal parametrization (ξ and γ) of the measurement curve, it ensures the spectral wavenumber increment remains constant, thereby allowing the field to be perfectly represented by a dramatically reduced, non-redundant set of equispaced samples in the transformed domain. Interpolation is subsequently performed using specialized Dirichlet or Chebyshev functions. This geometry-driven method achieved extreme efficiency, reducing the required Nyquist samples by a factor of 20, while consistently returning the highest fidelity reconstructions in both simulation and measurement.

Core Contribution: Adaptation to the Constrained Acquisition Domain

A paramount discrepancy between the theoretical non-redundant sampling literature and practical measurement systems lies in limited observation domain available in most setups. Theoretical non-redundant grids dictate sampling points that fall along radial lines extending indefinitely toward infinity. In realistic scenarios, the acquisition domain is physically constrained. Applying the theoretical scheme directly results in critical sampling points falling outside the measurable region, breaking the required regular spacing in the ξ -domain and collapsing the interpolation algorithm.

Addressing this severe limitation forms a key contribution of this work (Detailed in Section 4.1). To enable the deployment of non-redundant sampling in constrained domains, an advanced geometric adaptation, termed the “squeezing” methodology, was developed. Rather than simply discarding unattainable external radii, the “squeezing” algorithm dynamically recalculates and rescales all radial sampling positions inward so that the outermost radius precisely aligns with the edge of the bounded observation domain.

Crucially, this uniform compression preserves the strict requisite that sampling radii remain perfectly equispaced in the transformed ξ -domain. However, this spatial rearrangement breaks the 2π -periodicity inherent in the original theoretical grid derivations. Since the standard Dirichlet interpolation kernel relies explicitly on this periodicity, the original interpolation algorithm would fail. To resolve this, the conventional Dirichlet kernel was substituted with a modified sinc-like convolution kernel. The proposed sampling approach proved highly successful in maintaining peak precision across simulations and physical measurements.

Summary

This work has analyzed, implemented, and tested, using both numerical and experimental data, several state-of-the-art sampling approaches for reducing the number of measurements required for NFFFT. A novel method has been proposed that opportunely modifies the non-redundant sampling grid to fit the acquisition area. A quantitative comparison among these approaches has been presented, considering the accuracy of the far-field reconstruction within the reliable angular region, the achieved downsampling ratio, the robustness to noise, and the computational burden. The results show that the explicit incorporation of prior electromagnetic geometry has a decisive impact on far-field reconstruction. Agnostic approaches, while mathematically elegant and reducing initial modeling effort, incur prohibitive costs in either computation time or poor accuracy.

For the vast majority of realistic planar near-field measurement tasks, the non-redundant sampling method, significantly augmented by the proposed “squeezing” sampling adaptations introduced in this work, remains the best choice for reliability and precision. The method thrives on its rigorous physical grounding, and heuristic evaluations strongly indicate that utilizing an oversampling factor of unity ($\chi = 1$) provides the most robust and dependable balance of massive sample reduction and high-fidelity output.

Conversely, for applications requiring a further reduction in the number of data acquisitions, particularly in severely noise-corrupted environments, the selection-based source reconstruction approach provides a practical alternative.

Bibliography

- [1] F. Ferrara, C. Gennarelli, R. Guerriero, G. Riccio, and C. Savarese, “An efficient near-field to far-field transformation using the planar wide-mesh scanning,” *Journal of Electromagnetic Waves and Applications*, vol. 21, no. 3, pp. 341–357, 2007. DOI: 10.1163/156939307779367404
- [2] S. Gregson, J. McCormick, and C. Parini, *Principles of Planar Near-Field Antenna Measurements*. The Institution of Engineering and Technology, 2007. DOI: 10.1049/PBEW053E
- [3] D. Kerns and U. S. N. B. of Standards, *Plane-wave Scattering-matrix Theory of Antennas and Antenna-antenna Interactions: Formulation and Applications*. U.S. Department of Commerce, National Institute of Standards and Technology, 1976.
- [4] D. Paris, W. Leach, and E. Joy, “Basic theory of probe-compensated near-field measurements,” *IEEE Transactions on Antennas and Propagation*, vol. 26, no. 3, pp. 373–379, 1978. DOI: 10.1109/TAP.1978.1141855
- [5] T. Isernia, G. Leone, and R. Pierri, “Radiation pattern evaluation from near-field intensities on planes,” *IEEE Transactions on Antennas and Propagation*, vol. 44, no. 5, pp. 701–, 1996. DOI: 10.1109/8.496257
- [6] C. A. Balanis, *Antenna theory*, en, 2nd ed. Brisbane, QLD, Australia: John Wiley and Sons (WIE), Jul. 1996.
- [7] W. C. Chew, *Waves and fields in inhomogenous media*. Wiley-IEEE Press, 1995.
- [8] M. H. Francis and R. C. Wittmann, “Near-field scanning measurements: Theory and practice,” in *Modern Antenna Handbook*. John Wiley and Sons, Ltd, 2008, ch. 19, pp. 929–976, ISBN: 9780470294154. DOI: <https://doi.org/10.1002/9780470294154.ch19>
- [9] A. Ludwig, “The definition of cross polarization,” *IEEE Trans. Antennas Propag.*, vol. 21, no. 1, pp. 116–119, 1973. DOI: 10.1109/TAP.1973.1140406
- [10] J. Wang, “An examination of the theory and practices of planar near-field measurement,” *IEEE Trans. Antennas Propag.*, vol. 36, no. 6, pp. 746–753, 1988. DOI: 10.1109/8.1176
- [11] A. Yaghjian, “An overview of near-field antenna measurements,” *IEEE Trans. Antennas Propag.*, vol. 34, no. 1, pp. 30–45, 1986. DOI: 10.1109/TAP.1986.1143727

- [12] E. Martini, O. Breinbjerg, and S. Maci, “Reduction of truncation errors in planar near-field aperture antenna measurements using the gerchberg-papoulis algorithm,” *IEEE Trans. Antennas Propag.*, vol. 56, no. 11, pp. 3485–3493, 2008. DOI: 10.1109/TAP.2008.2005442
- [13] O. Bucci and G. Franceschetti, “On the spatial bandwidth of scattered field,” *IEEE Trans. Antennas Propag.*, vol. 35, pp. 1445–1455, Jan. 1988. DOI: 10.1109/TAP.1987.1144024
- [14] O. M. Bucci and G. Franceschetti, “On the degrees of freedom of scattered fields,” *IEEE Trans. Antennas Propag.*, vol. 37, pp. 918–926, Aug. 1989. DOI: 10.1109/8.29386
- [15] O. M. Bucci, C. Gennarelli, and C. Savarese, “Representation of electromagnetic fields over arbitrary surfaces by a finite and nonredundant number of samples,” *IEEE Trans. Antennas Propag.*, vol. 46, pp. 351–359, Apr. 1998. DOI: 10.1109/8.662654
- [16] O. M. Bucci, F. D’Agostino, G. Riccio, and C. Savarese, “Nf-ff transformation with plane-polar scanning: Ellipsoidal modelling of the antenna,” *AUTOMATIKA*, vol. 41, pp. 159–164, 2000, ISSN: 0005-1144.
- [17] M. A. Maisto, R. Pierri, and R. Solimene, “Near-field warping sampling scheme for broad-side antenna characterization,” *Electronics*, vol. 9, no. 6, 2020, ISSN: 2079-9292. DOI: 10.3390/electronics9061047
- [18] M. A. Maisto, G. Leone, A. Brancaccio, and R. Solimene, “Efficient planar near-field measurements for radiation pattern evaluation by a warping strategy,” *IEEE Access*, vol. 9, pp. 62 255–62 265, 2021. DOI: 10.1109/ACCESS.2021.3074786
- [19] M. A. Maisto, A. Ciociola, A. Cuccaro, and R. Solimene, “Warping-driven greedy method for data reduction in planar near-field antenna measurements,” *IEEE Trans. Antennas Propag.*, vol. 72, no. 10, pp. 7546–7559, 2024. DOI: 10.1109/TAP.2024.3441826
- [20] M. A. Qureshi, C. H. Schmidt, and T. F. Eibert, “Adaptive sampling in spherical and cylindrical near-field antenna measurements,” *IEEE Antennas and Propagation Magazine*, vol. 55, no. 1, pp. 243–249, 2013. DOI: 10.1109/MAP.2013.6474537
- [21] J. Zheng, X. Chen, and Y. Huang, “An effective antenna pattern reconstruction method for planar near-field measurement system,” *IEEE Transactions on Instrumentation and Measurement*, vol. 71, pp. 1–12, 2022. DOI: 10.1109/TIM.2022.3193194
- [22] Y. Chen, X. Liu, J. Zheng, and X. Chen, “A simple and effective planar near-field measurement method with sparse nonuniform sampling,” *IEEE Antennas and Wireless Propagation Letters*, vol. 23, no. 11, pp. 3947–3951, 2024. DOI: 10.1109/LAWP.2024.3437431
- [23] N. Mézières, B. Fuchs, L. L. Coq, J.-M. Lerat, R. Contreres, and G. L. Fur, “On the application of sparse spherical harmonic expansion for fast antenna far-field

- measurements,” *IEEE Antennas and Wireless Propagation Letters*, vol. 19, no. 5, pp. 746–750, 2020. DOI: 10.1109/LAWP.2020.2978170
- [24] M. D. Migliore, “Near field antenna measurement sampling strategies: From linear to nonlinear interpolation,” *Electronics*, vol. 7, no. 10, 2018, ISSN: 2079-9292. DOI: 10.3390/electronics7100257
- [25] B. Fuchs, L. Le Coq, and M. D. Migliore, “On the interpolation of electromagnetic near-field without prior knowledge of the radiating source,” *IEEE Trans. Antennas Propag.*, vol. 65, no. 7, pp. 3568–3574, 2017. DOI: 10.1109/TAP.2017.2705163
- [26] F. Cano-Fácil, S. Pivnenko, and M. Sierra-Castaner, “Reduction of truncation errors in planar, cylindrical, and partial spherical near-field antenna measurements,” *International Journal of Antennas and Propagation*, vol. 2012, Feb. 2012. DOI: 10.1155/2012/438727
- [27] F. D’Agostino, F. Ferrara, C. Gennarelli, R. Guerriero, and M. Migliozzi, “Laboratory testing on a nonredundant nf-ff transformation with plane-polar scanning optimized for quasi-planar antennas,” *2014 IEEE Conference on Antenna Measurements and Applications, CAMA 2014*, Jan. 2015. DOI: 10.1109/CAMA.2014.7003367
- [28] M. Fazel, H. Hindi, and S. Boyd, “Rank minimization and applications in system theory,” in *Proceedings of the 2004 American Control Conference*, vol. 4, 2004, 3273–3278 vol.4. DOI: 10.23919/ACC.2004.1384521
- [29] S. Joshi and S. P. Boyd, “Sensor selection via convex optimization,” *IEEE Transactions on Signal Processing*, vol. 57, pp. 451–462, 2009.
- [30] G. Gaborit, P. Artillan, C. Bermond, G. Revillod, G. Chevrier-Gros, and L. Duvillelet, “20 ghz antenna radiation pattern obtained from near-field mapping with electrooptic probe on a single plane,” *IEEE Antennas Wireless Propag. Lett.*, vol. 19, no. 7, pp. 1177–1181, 2020. DOI: 10.1109/LAWP.2020.2994263